ABSTRACT

Title: INVESTIGATION OF ACTIVE MATERIALS AS DRIVING ELEMENTS IN A HYDRAULIC-HYBRID ACTUATOR

Joshua Ellison, Master of Science, 2004

Directed By: Professor/Advisor, Dr. Inderjit Chopra,
Rotorcraft

In recent years, there have been growing applications of smart materials, such as piezoelectrics and magnetostrictives, as actuators in the aerospace and automotive fields. Although these materials have high force and large bandwidth capabilities, their use has been limited due to their small stroke. The use of hydraulic amplification in conjunction with motion rectification is an effective way to overcome this problem and to develop a high force, large stroke actuator. In the hybrid-hydraulic concept, a solid-state actuator is driven at a high frequency to pressurize fluid in a pumping chamber. This paper presents a comparison of a piezostack, Terfenol-D, and Galfenol element as the driving material in a hybrid-hydraulic actuator. The performance of the actuator with the various driving elements is measured through systematic testing and compared based on input power.

INVESTIGATION OF ACTIVE MATERIALS AS DRIVING ELEMENTS IN A HYDRAULIC-HYBRID ACTUATOR

By

Joshua Ellison

Thesis submitted to the Faculty of the Graduate School of the
University of Maryland, College Park, in partial fulfillment
of the requirements for the degree of
Master of Science
2004

Advisory Committee:
Professor Inderjit Chopra, Chair / Advisor
Professor Norman Wereley
Assistant Professor Christopher Cadou
Assistant Research Scientist Jayant Sirohi

Acknowledgements

I would like to thank my advisor, Dr. Inderjit Chopra, for his guidance and assistance throughout my career at the University of Maryland, as an undergraduate as well as a graduate student. His advice and encouragement was of great motivation to me, and I am extremely appreciative. I would also like to thank the members of my examining committee, Dr. Norman Wereley, Dr. Christopher Cadou, and Dr. Jayant Sirohi, for their time and input towards my thesis work.

A special thanks is due to my colleagues at the University of Maryland who have all taught me a great deal through discussions and our work together. I am greatly in debt to Jayant, who has been like a mentor in his assistance with my work. Others who have contributed a great deal to my learning experience are Shaju John, Jinsong Bau, Dr. Yoo, Dr. Nagaraj, Alex Zajac, Ron Couch, Jaye Falls, Felipe Bohorquez, Paul Samuel, and many others.

Table of Contents

Chapter 1: Introduction

1.1 Background and Problem Statement

In recent years, there have been growing applications of smart materials, such as piezoelectrics and magnetostrictives, as actuators in the aerospace and automotive fields. Smart materials undergo an induced strain due to the application of an electric, magnetic, or thermal field. Piezoelectrics and magnetostrictives, specifically, are attractive as actuators due to their high energy density, large blocked force, and wide actuation bandwidth. In addition, these actuators have no moving parts and are therefore, mechanically less complex than conventional actuators such as hydraulic systems.

Smart materials are particularly attractive as actuators for helicopter rotors [1]. Due to the inherently unsteady environment of a helicopter rotor, the rotor blades undergo large vibratory loads which are transmitted to the rotor hub and the rest of the vehicle. These vibrations limit helicopter performance and reduce the fatigue life of rotor components [2]. In order to actively reduce the vibratory loads, two methods of control are implemented. These methods are higher harmonic control (HHC) and individual blade control (IBC). Currently, rotorcraft utilize bulky and mechanically complex swashplate systems for primary control and higher harmonic control of the main rotor. For HHC, the swashplate is excited in the fixed frame at N_b/rev (N_b = number of blades) frequency. This results in higher harmonic excitations of blade pitch at N_b/rev and $N_b \pm 1$/rev frequencies. The effects of this method of vibration control have been investigated analytically and experimentally [3-11]. Although successful in reducing vibrations, these systems have a high weight penalty and consist of many moving parts. In addition, HHC is limited to controlling vibrations of N_b/rev.

Individual Blade Control (IBC) is a method of vibration reduction where actuators are incorporated in the rotating frame of the rotor. Besides hydraulic actuators, a variety of smart material actuators have been investigated for IBC vibration reduction. This method has the flexibility of exciting the blade at any desired frequency. However, the hydraulic actuators not only incur a significant weight penalty, but also require a mechanically complex hydraulic slipring. On the other hand, smart material actuators are compact and may provide the flexibility of distributed actuation. In addition to active vibration controls, passive control methods such as composite tailored rotor blades that incorporate bending/torsion coupling have shown benefits in reducing rotor blade vibration in Mach scaled rotors [12]. On-blade actuators such as trailing edge flap actuators and active twist rotors have been investigated for use on a smart rotor [13-22]. Several problems exist in implementing this type of actuators. In addition to size constraints of the blade volume, the actuators must be designed to work efficiently under the high centrifugal loads present on the rotor blades.

One possible solution to these problems could involve the use of an active pitch link on a swashplateless rotor. By incorporating the smart actuator on the pitch links of a rotor, the problems associated with on-blade actuators could be avoided. Such a system utilizing smart materials would weigh substantially less than a swashplate system, and would offer higher frequency control of the rotor. The large operating bandwidth of piezoelectrics and magnetostrictives would allow high frequency inputs for vibration reduction as well as low frequency primary control inputs. In addition, control of the actuator would be achieved through electrical inputs as opposed to the hydraulic input to a swashplate system. This significantly lowers the mechanical complexity of the whole system.

1.2 Hydraulic Hybrid Actuators

A problem with implementing actuators using these smart materials is that, although they have high energy densities and large bandwidth capabilities, their use is usually limited due to their small stroke [1]. Without a means of stroke amplification, these actuators can only reach strain levels on the order of 1000 ppm. To overcome this limitation, many types of mechanical amplification have been investigated, where linkages are used to amplify the stroke of the material. These methods trade output force for a larger stroke. In addition, finite stiffness of linkages results in energy loss and limits the amplification to less than 15. In fact, studies have shown that mechanical amplification methods lead to reductions in actuator energy density of up to 80% [23].

Another method often used to overcome the limited stroke of these materials is frequency rectification. The concept of frequency rectification involves conversion of the bi-directional strain of a smart element into a continuous uni-directional output, providing larger stroke at a lower bandwidth. Examples of frequency rectification in actuators are inchworm motors, rotary piezostack motors, and ultrasonic motors, although these actuators are not ideal for a smart rotor application [24-26]. These actuators experience rapid wearing due to their use of friction to generate motion.

The use of a hydraulic fluid and valve system for frequency rectification is an effective way to overcome the problem of small stroke and develop a moderately high force, large stroke actuator ideal for this application. This combination of smart material driving a hydraulic fluid system is called a hydraulic-hybrid actuator. In the hydraulic-hybrid concept, an active smart material, most commonly piezoelectric, is driven at a high frequency to pressurize fluid in a pumping chamber. The flow of the pressurized fluid is then rectified by a set of one-way valves, creating pulsing flow in a specified direction. The one directional flow is then utilized to transfer power from the active material to a hydraulic output cylinder. Through this stepwise actuation process, the high frequency, small stroke of the active material is converted into a larger, lower frequency displacement of the output cylinder. Throughout this report, the term 'actuator' will be used to refer to the entire hydraulic-hybrid actuator and the "driving element" will refer to the active material driving the piston.

1.3 State of the Art

Several hydraulic-hybrid pumps have been constructed to investigate behavior and proof of concept. Because various sized driving elements were used, performance results differed in each case. Mauck and Lynch developed a PZT pump that achieved a performance of 7.25 cm/sec unloaded velocity and 271 N (61 lbs.) of blocked force.

The system used a large piezostack of length 10.2 cm and cross-sectional area 3.6 cm^2. The piezostack was actuated at its optimum operating condition of 800 V input at an actuation frequency of 60 Hz. The actuation frequency was limited due to self-heating and high levels of required input current. In addition to experimentally determining performance characteristics and the effects of fluid viscosity, a lumped parameter model of the system was also developed [27-31].

Nasser developed a compact piezohydraulic actuation system that utilized active solenoid valves to rectify the piezoelectric actuation and produce unidirectional motion in the output cylinder. The system used a piezoelectric stack actuator with a free displacement of 100 μm and a blocked force of 3000 N with a peak-to-peak input of 150 V. The actuator produced an unloaded velocity of 0.0180 cm/sec and a blocked force of 100 N. The low bandwidth of the solenoid valves ultimately limited the actuation frequency of the piezoelectric actuator to 7 Hz. It was found that the time delay of the valves was the primary limiting factor in achieving higher speeds and greater power from the actuator. In addition, a lumped parameter system model was developed to predict the steady state motion of the output cylinder with respect to the piezoelectric actuator. By incorporating a time delay associated with the mechanical response time of the valves, the model was able to predict uni-directional motion of the actuator [32-35].

Konishi developed a piezoelectric hydraulic hybrid actuator driven by a piezostack with high blocked force. The piezostack had a length of 55.5mm and a diameter of

22mm. Its blocked force was 10.8kN and its free displacement was $60\,\mu m$ at an operating voltage of 600 V peak-to-peak. The actuator was excited at frequencies up to 300 Hz, and delivered an output power of 34 W. In addition, mathematical models were developed to investigate the use of fluid resonance on the maximum output power achievable [36-39].

In addition, Gerver has developed a magnetostrictive water pump using Terfenol-D that utilizes a two-stage actuation system and a hydraulic stroke amplifier to effectively increase the induced strain of the actuator. The designed flow rate of the pump is 30 ml/sec at a pressure of 5 psi for a power consumption of 25 W [40].

Other interesting studies include a review of magnetostrictive actuators and their applications performed by Claeyssen [41], as well as the ongoing developments of a piezo-hydraulic actuator made by CSA engineering [42].

At the University of Maryland, Sirohi and Chopra designed and constructed a piezo-hydraulic actuator for potential use in smart rotor applications. The device used two piezostacks of total length 3.61 cm and cross-sectional dimensions of 1 cm x 1 cm. The piezostack was actuated in a high frequency pump to pressurize hydraulic fluid (MIL-H-5606F), and two passive mechanical check valves to rectify the flow direction. In order to focus on the dynamics of the system, the actuator was designed only to move the output cylinder in a unidirectional fashion. The pump was coupled to a manifold containing a return valve that was used to reset the position of the output cylinder after actuation. The pump and manifold were then coupled to a commercially available hydraulic cylinder. A schematic of the complete actuator will be described in detail (see Chapter 2). In testing the performance of the system, the piezo-stacks were driven at frequencies from 50 to 700 Hz at 0-100 Volts while velocity was measured from the output cylinder. Experiments were repeated with varying parameters such as reed valve thickness, biased pressure, and piston diaphragm thickness in order to determine optimum settings for the actuator. The actuator was found to have an unloaded velocity of about 17.78 cm/sec and a blocked force of 80 N. Although the piezo-hydraulic pump showed good performance in low pumping frequency tests, it exhibited self-heating problems at high pumping frequencies. This ultimately limited the actuator's achievable flow rate [43-46].

In addition to experimental work carried out on the piezo-hydraulic actuator, a quasi-static model was developed for improving the performance of the actuator fluid system. The model showed good correlation with experimental results at low frequencies (<150 Hz), and found that the inertia of the piezostack load dominates the behavior of the device at high frequencies [47].

1.4 Present Work

Although proof of concepts have been established, several issues were encountered in previous works developing these actuators. One problem with using piezoceramic stacks in this type of actuator is their temperature sensitivity. At high actuation frequencies (~1kHz), the piezostacks generate significant heat that can deteriorate their performance. Brittleness of the material can also be a problem. After many cycles of operation, small cracks are observed to develop in the layers of a piezoceramic stack. The damage can significantly affect performance and is not easily detected. In addition, although piezostacks have a high energy density and perform well in these actuators, a driving element with a larger stroke could dramatically improve actuator performance. Due to these problems, it was necessary to examine other active materials as the driving elements in this hydraulic actuator.

Magnetostrictives are an attractive option because they do not generate as much heat as piezostacks and their performance is less sensitive to temperature. These materials achieve high levels of strain under an applied magnetic field. A field generating coil wound around the driving element is used to actuate the material. Strain levels can be as high as 2000 ppm with their blocked forces and bandwidth on the order of piezostacks.

Terfenol-D is a good option for this application due to its high magnetostriction (~2000 ppm) and large blocked force [48]. However, there are several drawbacks in using Terfenol-D. The material is extremely brittle and can develop cracking after prolonged periods of actuation. In addition, the magnetic field required to induce the strain in Terfenol-D is large, and would likely require high levels of input power, as well as a bulky and heavy electromagnetic field generator. Terfenol-D is also very expensive. An alternate magnetostrictive material that can be used is Galfenol. Unlike Terfenol-D, Galfenol requires very small magnetic fields and is robust and machinable. Galfenol is much less expensive than Terfenol-D as well. The only drawback of Galfenol is that its magnetostriction (~300 ppm) is much smaller than that of Terfenol-D. With several options available, there is a need to compare the performance of various materials as the driving elements in hydraulic hybrid actuator [49-51].

The present work involved the performance comparison of three smart materials as the driving element in the existing actuator. The performance of the actuator was studied using two magnetostrictive materials, Galfenol and Terfenol-D, and one type of piezostack as the driving elements. An energy based comparison of typical magnetostrictives and piezoelectrics shows energy densities of the materials are on the same order [52]. Comparisons were made based on input power required by the material, and keeping the same active length of the driving element. Other system components, such as reed valves, piston, piston diaphragm, etc., were all held constant. The only parts changed throughout the tests were those required to drive the active material, such as the electromagnetic field generator for the magnetostrictive materials. Testing was conducted to determine unloaded velocity, blocked force, output power, and strain of the active material. By comparing the input power required by each driving material, an overall efficiency was obtained for each actuator. Although these actuators do not meet performance requirements for full-scale applications, a comparison of driving materials will be useful in selecting the configuration for a full sized actuator.

In addition, the hydraulic-hybrid pump was converted for bi-directional actuation in order to evaluate the feasibility of such a system as well as to determine the frequency response characteristics of a bi-directional actuator. For this experiment, a new manifold was designed and built to house a set of bi-directional valves. Coupled to the existing pump, the valve system allowed bi-directional actuation of the output cylinder. Tests were carried out to show the effect of the added manifold, and the performance characteristics of the bi-directional system were quantified.

1.5 Thesis Outline

The thesis is organized in the following chapters:

Chapter 1: Introduction: This chapter gives a description of the background and problem statement, state of the art, and scope of the present work.

Chapter 2: Hydraulic-Hybrid Actuator: This chapter explains the hybrid actuator operating mechanism and gives a description of the parts and subassemblies. The experimental setup is also described.

Chapter 3: Piezoelectric Material: This chapter gives a brief overview of the basic principles of piezoelectric actuation.

Chapter 4: Magnetostrictive Material: This chapter gives a brief overview of the basic principles of magnetostrictive actuation.

Chapter 5: Magnetostrictive Actuator Design and Testing: This chapter presents the design and experimental tests and results of a first generation magnetostrictive actuator using Terfenol-D and Galfenol.

Chapter 6: Magnetostrictive Actuator Coil Design: This chapter describes an algorithm for calculating various coil properties as a function of wire diameter for generating a magnetic field.

Chapter 7: Magnetostrictive Actuator Characterization: This chapter presents the design and quasi-static performance of a second generation, lower inductance magnetostrictive actuator based on the coil design analysis.

Chapter 8: Piezostack Actuator Characterization: This chapter presents the design and quasi-static performance of a piezostack actuator for comparison with magnetostrictive actuators.

Chapter 9: Comparison of Results: Experimental results and analysis are presented in this chapter for testing of the piezostack and magnetostrictive hybrid actuators.

Chapter 10: Bi-Directional Operation: Experimental results and analysis are presented in this chapter for testing of a bi-directional valve system coupled to the Terfenol-D driven actuator.

Chapter 11: Summary and Conclusions: This chapter summarizes the results of the present study and presents the conclusions.

Chapter 2: Hydraulic-Hybrid Actuator

2.1 Basic Operating Mechanism

The basic operation of the hydraulic-hybrid actuator involves three stages. A schematic of the system (Figure 2.1) highlights these steps. The first stage involves the actuation of an active material to pressurize fluid in the pumping chamber. By applying an alternating field, the material is made to expand and contract, driving a piston in and out of the pumping chamber. The movement of the piston pressurizes the fluid in the pumping chamber. The next step is to create a single direction of fluid flow from the pumping material. A set of reed valves is used to allow flow only in a specified direction. In this case, frequency rectification is used to convert bi-directional actuation of the driving material into a single direction of fluid flow. The final stage of the hydraulic-hybrid concept is the transfer of power from the driving material to the output cylinder through the hydraulic circuit. The hydraulic circuit

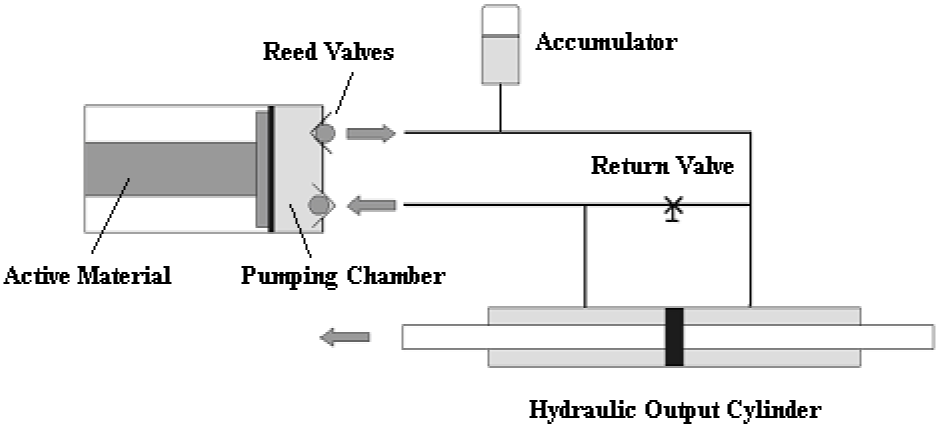

Figure 2.1 - Schematic of Hydraulic-Hybrid Actuator

consists of a network of tubes used to direct the fluid to either side of the output cylinder and usually includes an accumulator from which a bias pressure can be applied on the fluid. The subassemblies of the entire actuator are explained in more detail below.

2.2 Subassemblies

Pump Body

The driving material used to pressurize the fluid in this actuator is held in a steel cylinder called the pump body. The pump body is 2” long, has a 1.4” outer diameter and a 1” bore diameter. The driving material is enclosed in the pump body at one end by the piston-diaphragm assembly, and at the other end by a preload base. A diagram of the pump body assembly is shown in Figure 2.2. The preload base can be tightened against the active material to provide a compressive preload. The pump body is made thick enough to be much stiffer than the active material, so the strain of the active material is not lost in deforming the body. Slots are cut in the preload base to allow room for power and sensor wires. When preload is applied, the driving

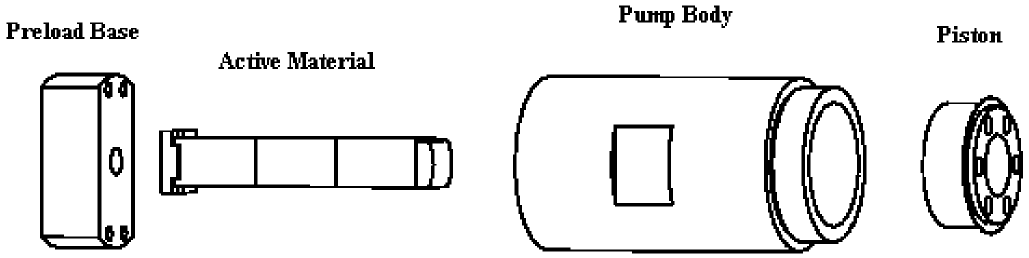

Figure 2.2 - Pump Body Assembly

material is pressed against the piston-diaphragm assembly. The piston is made of steel and has a tight running fit with the bore of the pump body. The side of the piston not in contact with the active material makes up the top part of the pumping chamber. A 0.002” thick C-1095 spring steel diaphragm is bonded to both the piston head and the pump body, sealing the pump body from the fluid in the pumping chamber. When the driving material is actuated, it displaces the piston by bending the piston diaphragm. The movement of the piston then changes the volume of the pumping chamber and pressurizes the fluid. The initial volume of the pumping chamber is 0.04 in^3 (0.656 cm^3).

Valve Assembly

The flow rectifying valves used for the present actuator are passive reed valves. The assembly consists of two aluminum valve plates and a reed valve with two flaps that is made of 0.002” (0.0508 mm) thick C-1095 spring steel. The reed valve is bonded between the valve plates, and allows fluid to flow in only one direction. The diagram in Figure 2.3 shows the two valve plates and reed valve that make up the valve assembly. When assembled, the reed flaps are only free to open in one direction. When the driving material expands, and the pressure of the fluid in the pumping chamber increases, fluid is allowed to flow out through one port only. Conversely, when the pressure decreases, fluid is allowed to flow in through the other port. The result is a steady flow of fluid out of the pumping chamber through one port, and into the pumping chamber through the other. For high frequency applications, a system with fewer moving parts is desirable because it will inherently be more reliable, provided the valves function properly. An example of active valves that do not include moving parts is magnetorheological (MR) valves. MR valves utilize a magnetic field produced from a coil to change the viscosity of the working fluid, which in this case must be MR fluid. This concept is in its early stage of development [53].

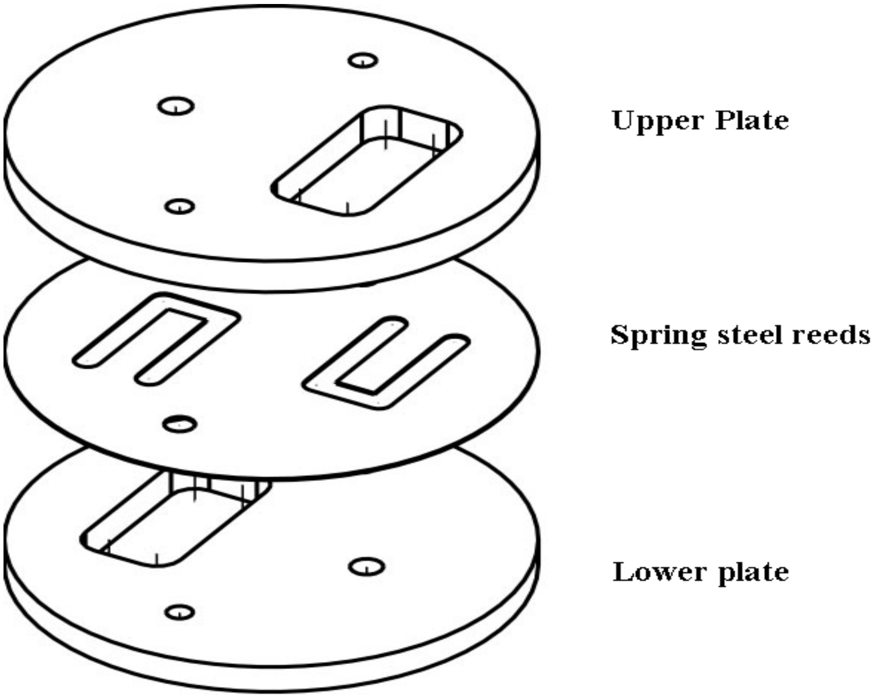

Figure 2.3 - Valve Assembly

Hydraulic Circuit

The hydraulic circuit for this actuator consists of a manifold, an output cylinder, and an accumulator. The manifold is constructed out of aluminum and was designed and manufactured in-house. It contains the tubing required to direct the fluid to and from the pumping chamber and the output cylinder. A picture of the manifold and output cylinder coupled to the pump body assembly is shown in Figure 2.4. In this configuration, the manifold only directs the fluid to one side of the output cylinder, so

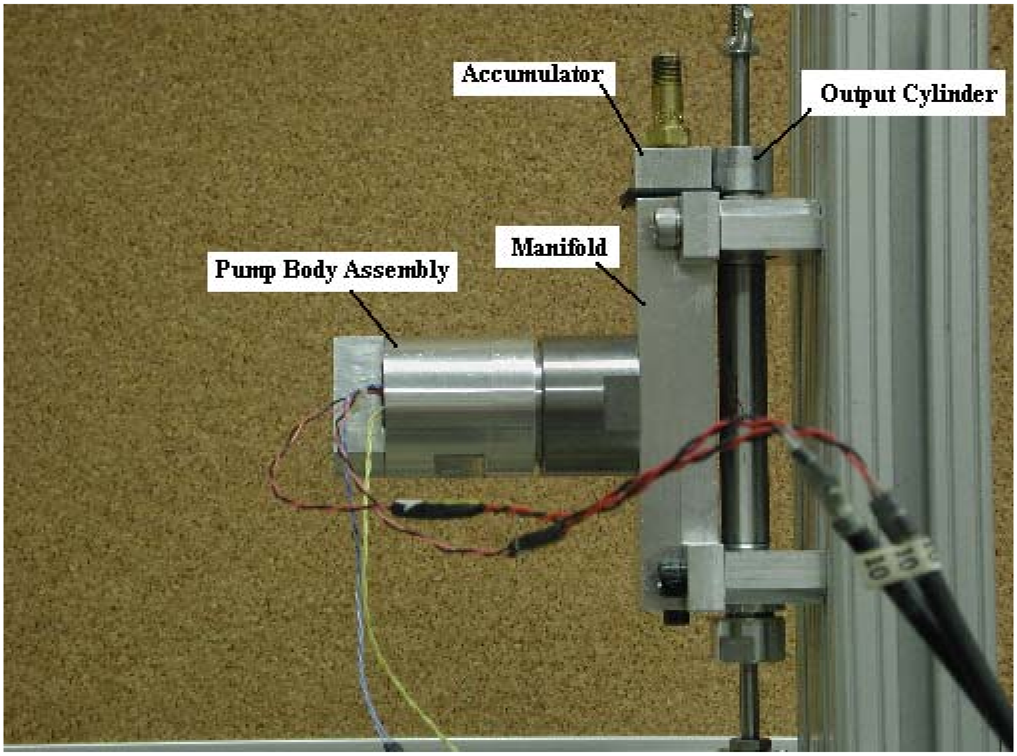

Figure 2.4 – Hydraulic-Hybrid Actuator

that the actuator can only be operated in one direction. A return valve mechanism is utilized to allow the output cylinder to reset to its original position. This is a problem in the development of the actuator since any envisioned application would require bi-directional capability. Attached to the manifold is an accumulator with a gas volume of about 0.1 cubic inches. The accumulator has a 0.06” rubber diaphragm, and is used to apply a bias pressure to the fluid in the actuator. This helps to prevent cavitation in the fluid and also serves to add some preload to the active material. A bias pressure of 200 psi was applied to the fluid for all tests. The output cylinder is a commercially available double acting hydraulic cylinder from Bimba Manufacturing Company with a 7/16” bore diameter, a rod diameter of 3/16”, and a 2” stroke [54]. Relevant dimensions of the actuator assemblies are listed in Table 2.1.

Actuator Dimensions	
Pump Body Assembly	
Pump Body Diameter	1.4" od, 1" id
Pump Body Length	2"
Active Material Length	2"
Piston Diaphragm Thickness	0.002"
Pumping Chamber Diameter	1"
Pumping Chamber Height	0.05"
Valve Assembly	
Valve Plate Thickness	0.2"
Reed Valve Thickness	0.002"
Hydraulic Circuit	
Accumulator Gas Volume	0.1 cubic in.
Output Cylinder Bore	7/16"
Output Shaft Diameter	3/16"
Output Cylinder Stroke	2"

Table 2.1 - Actuator Dimensions

2.3 Experimental Setup and Procedure

Before driving the actuator, the system must be completely filled with fluid. In order to fill the actuator without any air in the fluid, the system must first be vacuumed. Using an adapter in place of the accumulator, a vacuum pump is attached to the manifold. The vacuum pulls the air out of the system through a fluid reservoir. After vacuuming for several minutes, the pressure in the reservoir is released, and the fluid drains into the vacuumed actuator. The fluid in the actuator is then pressurized to about 50 psi to identify any leaks. If no leaks are identified, the vacuum adapter is replaced by the accumulator, and a bias pressure is applied to the fluid. For all tests in this paper, the bias pressure applied was 200 psi. At a pressure of 200 psi, the fluid applies a stress of 3.2 ksi to the Terfenol-D and Galfenol rods, and a stress of 1 ksi to the piezostack, which has a larger cross-sectional area than the magnetostrictive rods.

Tests were performed on the actuator in three categories. No-load tests were performed to determine the fluid flow rate of the actuator using each driving material. The velocities obtained during these tests correspond to the power required to overcome losses in the actuator. Loaded tests were performed to investigate the actuator performance in an externally loaded condition. For these tests, weights were hung from the shaft of the output cylinder, applying a constant load to the fluid and the active material. The no-load tests as well as the loaded tests were performed using uni-directional actuation. A return valve is opened after each test to allow the output cylinder to return to its initial position. The third test performed was a bi-directional actuation of the system. For these tests, commercially available valves were attached to the actuator via a new manifold that was designed and fabricated in-house. The return valve remained closed at all times during these tests. No-load was applied during bi-directional actuation.

The active material was actuated using two different power amplifiers. The piezostacks were actuated using an AE Techron, LV 3620 Linear Amplifier [55]. The coil used to actuate the magnetostrictive material was driven using a QSC Audio, RMX 2450 Professional Power Amplifier [56]. In both cases, a Stanford Research

Systems, 3.1 MHz Synthesized Function Generator was used to supply the input signal to the amplifiers [57].

During each test, data was acquired using a National Instruments PCI-6031E 16-bit DAQ card in conjunction with a MatLab program [58-59]. The program recorded voltage and current levels applied to the active material from sense resistors in parallel and series, as shown in Figure 2.5. Voltage dividers were used to obtain a signal within the limits of the DAQ system, and all data corrections were performed using the MatLab program. The strain of the active material and the output cylinder velocity were also acquired using the DAQ system. The strain of the active material was measured using four 120 ohm strain gauges (from Micro-Measurements) in a full-bridge configuration [60]. The gauges were bonded to the active material and

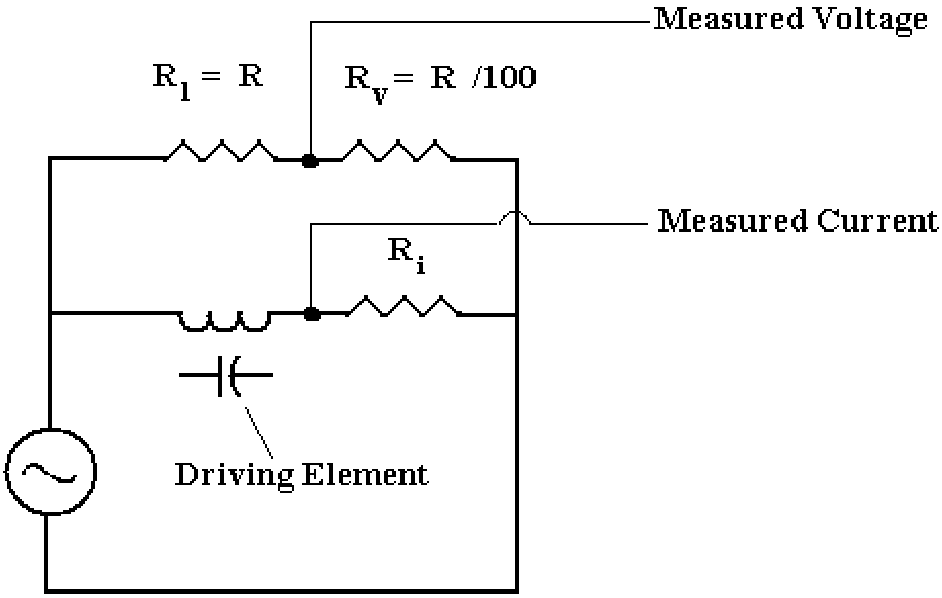

Figure 2.5 - Circuit Used for Voltage and Current Measurements

covered with a polyurethane coating for protection and insulation. The velocity of the output cylinder was measured using a linear potentiometer that was attached to the shaft of the output cylinder and had a 2.25” stroke.

Before analyzing the experimental results of these tests, a brief review of the basic principles of magnetostrictives and piezoelectrics is presented.

Chapter 3: Piezoelectric Material

3.1 Basic Material Principles

Piezoelectricity refers to the generation of electricity under a mechanical pressure. This phenomenon is observed in many naturally occurring crystals. This phenomenon was first predicted and measured by Pierre and Jacques Curie in 1880, and is known as the direct piezoelectric effect. A converse piezoelectric effect also exists and is the generation of a mechanical strain under an applied electric field. The subject of piezoelectricity remained purely academic until around the World War era, when a growing interest in locating underwater objects led to the development of piezoelectric devices for emitting and receiving ultrasonic waves underwater. Several developments would be made in the following decades leading to piezoelectric resonators, oscillators, and transformers that are used today in a wide range of applications. Later, the development of manufactured piezoelectric elements called piezoceramics led to a wide range of applications. Piezoceramics exhibit a much larger piezoelectric affect than natural piezoelectrics such as quartz and tourmaline, and can easily be manufactured to a desired size and shape. The most common form of piezoceramics is based on lead zirconate titanate (PZT) compounds. Piezoceramics are available commercially in various shapes and even as assembled actuators such as stacks, benders, and torque tubes.

The piezoelectric effect can be traced to the unit cell of the crystal. The cell has a certain degree of asymmetry, leading to a separation of positive and negative charges that results in a polarization of the material. In piezoceramics, the material is manufactured with a similar asymmetry. For example, a PZT unit cell is manufactured so that the titanium atom is slightly off center, resulting in an inherent asymmetry that produces a permanent dipole. A typical PZT unit cell is shown in Figure 3.1. The cell is tetragonal with the dipole aligned along the long axis or c-axis

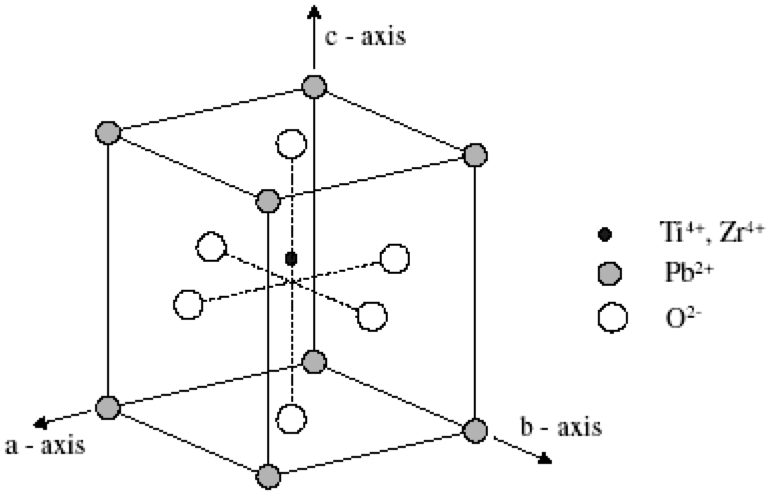

Figure 3.1 - Typical PZT Unit Cell

as shown in the figure. A volume of these unit cells with the dipoles aligned in the same direction is called a domain. A bulk sample of PZT material will contain several randomly oriented domains. A process called poling, where a large electric field is applied to the material, aligns most of the domains such that their dipoles are parallel to the applied field as shown in Figure 3.2. This process creates a permanent net polarization of the material. Once polarized, an applied voltage with the same polarity of the poling voltage causing a temporary expansion in the poling direction and an unequal contraction in the plane parallel to the poling direction. The result is a small net change in volume with applied voltage. The material will return to its original dimensions upon removal of the voltage.

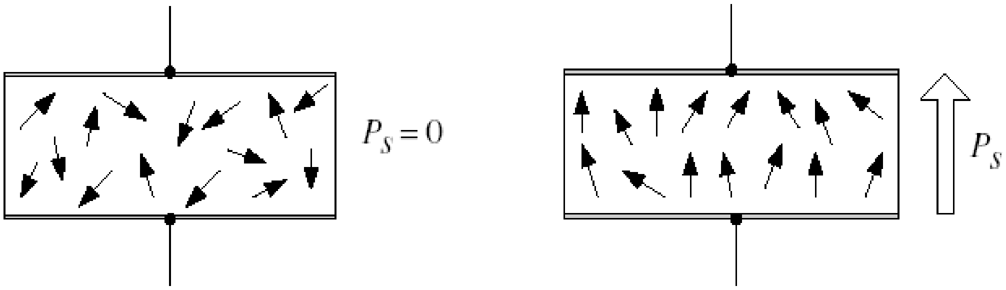

Figure 3.2 - Effect of Poling Aligning Material Domains

3.2 Piezostack Actuator

Consider a piezoceramic sheet with two electrodes as shown in Figure 3.3. When the sheet is used as an actuator, an electrical field is input, producing a mechanical strain output. In a piezostack actuator, many of these sheets are bonded on top of each other

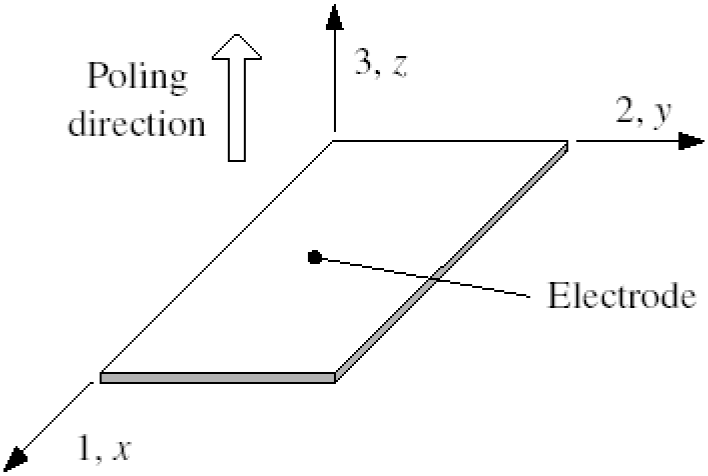

Figure 3.3 - Piezoceramic Sheet Poled With Two Electrodes

with common electrodes. The strain of the entire stack is the added strain of each plate in the stacked direction.

The constitutive relation for a piezoceramic sheet can be written as:

$$\varepsilon = s^{\mathrm{E}}\sigma + d^{c}\mathrm{E} + \alpha\Delta T \qquad \text{Eq. 3.1}$$

The effects of thermal expansion can be left out for the purpose of this discussion, leaving:

$$\varepsilon = s^{\mathrm{E}}\sigma + d^{c}\mathrm{E} \qquad \text{Eq. 3.2}$$

where s^{E} (N/m$^{2)}$ defines the mechanical compliance of the material under a constant electric field. The compliance term s_{km}^{E} is defined as the elastic strain in direction-k due to a unit stress in direction-m. For a piezoceramic, the compliance matrix is defined as:

$$\begin{aligned}
s^{\mathbb{E}} &= \begin{bmatrix} s_{11}^{\mathbb{E}} & s_{12}^{\mathrm{E}} & s_{13}^{\mathrm{E}} & 0 & 0 & 0 \\ s_{12}^{\mathbb{E}} & s_{11}^{\mathrm{E}} & s_{13}^{\mathrm{E}} & 0 & 0 & 0 \\ s_{13}^{\mathbb{E}} & s_{13}^{\mathrm{E}} & s_{33}^{\mathrm{E}} & 0 & 0 & 0 \\ 0 & 0 & 0 & s_{44}^{\mathbb{E}} & 0 & 0 \\ 0 & 0 & 0 & 0 & s_{44}^{\mathrm{E}} & 0 \\ 0 & 0 & 0 & 0 & 0 & s_{66}^{\mathrm{E}} \end{bmatrix} \\
&= \begin{bmatrix} \frac{1}{E_1} & -\frac{\nu_{12}}{E_1} & -\frac{\nu_{31}}{E_3} & 0 & 0 & 0 \\ -\frac{\nu_{12}}{E_1} & \frac{1}{E_1} & -\frac{\nu_{31}}{E_3} & 0 & 0 & 0 \\ -\frac{\nu_{31}}{E_3} & -\frac{\nu_{31}}{E_3} & \frac{1}{E_3} & 0 & 0 & 0 \\ 0 & 0 & 0 & \frac{2(1+\nu_{31})}{E_3} & 0 & 0 \\ 0 & 0 & 0 & 0 & \frac{2(1+\nu_{31})}{E_3} & 0 \\ 0 & 0 & 0 & 0 & 0 & \frac{2(1+\nu_{12})}{E_1} \end{bmatrix}
\end{aligned} \qquad \text{Eq. 3.3}$$

Note that the variable E_1 in the above matrix represents the Young's Modulus in the 1-axis direction and should not be confused with the variable E_1, which represents the electric field applied in the 1-axis direction. The piezoelectric coefficient matrix, d^c (m/Volt) is defined as the amount of strain per unit of electric field at constant mechanical stress. The matrix is given by:

$$\mathbf{d}^c = \begin{bmatrix} 0 & 0 & d_{31} \\ 0 & 0 & d_{32} \\ 0 & 0 & d_{33} \\ 0 & d_{24} & 0 \\ d_{15} & 0 & 0 \\ 0 & 0 & 0 \end{bmatrix}$$

Eq. 3.4

The coefficient d_{31} represents the strain in the 1-axis due to an electric field E_3 in the 3-axis. Expanding the constitutive equations,

$$\begin{Bmatrix} \epsilon_1 \\ \epsilon_2 \\ \epsilon_3 \\ \epsilon_4 \\ \epsilon_5 \\ \epsilon_6 \end{Bmatrix} = \begin{bmatrix} s_{11}^{\mathbb{E}} & s_{12}^{\mathbb{E}} & s_{13}^{\mathbb{E}} & 0 & 0 & 0 \\ s_{12}^{\mathbb{E}} & s_{11}^{\mathbb{E}} & s_{13}^{\mathbb{E}} & 0 & 0 & 0 \\ s_{13}^{\mathbb{E}} & s_{13}^{\mathbb{E}} & s_{33}^{\mathbb{E}} & 0 & 0 & 0 \\ 0 & 0 & 0 & s_{44}^{\mathbb{E}} & 0 & 0 \\ 0 & 0 & 0 & 0 & s_{44}^{\mathbb{E}} & 0 \\ 0 & 0 & 0 & 0 & 0 & s_{66}^{\mathbb{E}} \end{bmatrix} \begin{Bmatrix} \sigma_1 \\ \sigma_2 \\ \sigma_3 \\ \sigma_4 \\ \sigma_5 \\ \sigma_6 \end{Bmatrix} + \begin{bmatrix} 0 & 0 & d_{31} \\ 0 & 0 & d_{31} \\ 0 & 0 & d_{33} \\ 0 & d_{15} & 0 \\ d_{15} & 0 & 0 \\ 0 & 0 & 0 \end{bmatrix} \begin{Bmatrix} \mathbb{E}_1 \\ \mathbb{E}_2 \\ \mathbb{E}_3 \end{Bmatrix}$$

Eq. 3.5

For a piezostack, with electrodes on only the 1-2 plane of each sheet, it is only possible to introduce an electric field in the 3-axis direction, E_3. Therefore, an applied electric field E_3 under no mechanical stress, will result in direct strains ε_1, ε_2, and ε_3 of the piezoceramic plate. In this case, the strain in the 3-axis direction is multiplied by the number of plates and becomes much larger than the strain in the 1 or 2 axis direction.

Two key parameters to consider when selecting a piezostack are its blocked force, F_b, and its free displacement, δ_f. The blocked force is the amount of force required to completely constrain the piezostack from any displacement under an applied field. The free displacement is the amount of displacement occurring at an applied field with no external mechanical force. Setting $\sigma = 0$, and focusing only on the 3-axis direction, Eq. 3.5 reduces to,

$$\delta_f = d_{33}\mathrm{E}_3 \qquad \text{Eq. 3.6}$$

In this case, d_{33} represents the piezoelectric coefficient of the entire piezostack. The blocked force is equal to the product of the free displacement and the stiffness of the piezostack itself.

$$F_b = \delta_f K_{act} \qquad \text{Eq. 3.7}$$

In order to determine the performance of a piezostack, the actuator load line must be examined. The actuator load line consists of the force plotted against output displacement for a constant voltage input. For any loading condition, the force and displacement of the piezostack will lie on the load line. A typical piezostack load line is shown in Figure 3.4. The y and x axis intercepts represent the actuator blocked

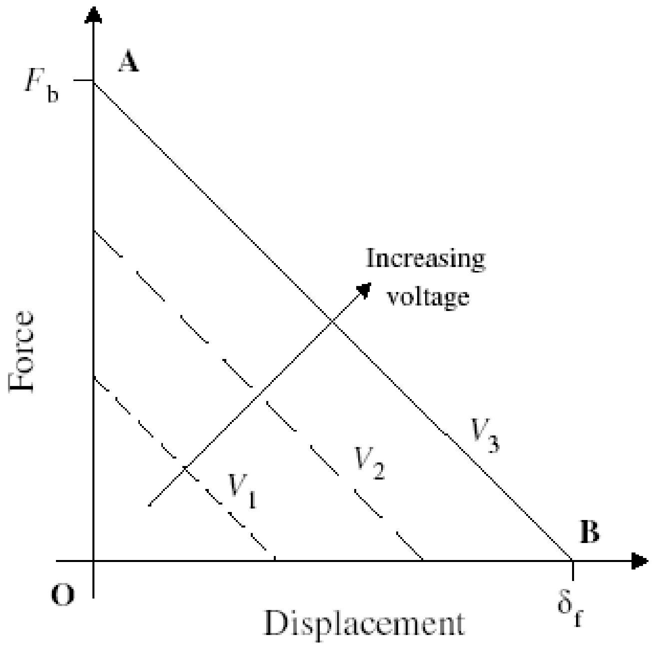

Figure 3.4 - Typical Piezostack Load Line

force and free displacement, respectively. The load line, for a given voltage, connects the two points, as in the case of V_3 (line segment AB). Load lines for V_1 and V_2 are plotted as well. As the input voltage increases, both the free displacement and blocked force of the piezostack increase, shifting the load line, as shown in Figure 8. At a constant voltage, the force produced by the piezostack, F_o can be expressed as a function of its displacement, δ_o,

$$F_o = F_b\left[1-\frac{\delta_o}{\delta_f}\right] \qquad \text{Eq. 3.8}$$

$$F_o = F_b - \delta_o K_{act}$$

where K_{act} is the actuator stiffness and is equal to the blocked force over the free displacement. Similarly, the displacement of the piezostack can be expressed as a function of its exerted force,

$$\delta_o = \delta_f \left[1 - \frac{F_o}{F_b} \right]$$ Eq. 3.9

$$\delta_o = \delta_f - \frac{F_o}{K_{act}}$$

Hydraulic Hybrid Actuator Load Line Analysis

An external load can now be introduced in the load line to analyze its effect on the performance of a piezostack. It should be noted that the following analysis is generic and can be applied to any driving element. For the case of the hydraulic hybrid actuator, the external load on the driving element consists of several components. The stiffness of some of these components, such as the accumulator, fluid and tubing, and pump body, is very large and can be ignored in the analysis. Simplifying the system, a series of spring elements can be modeled as the important components of the actuator. Figure 3.5 shows the simplified system model, consisting of the

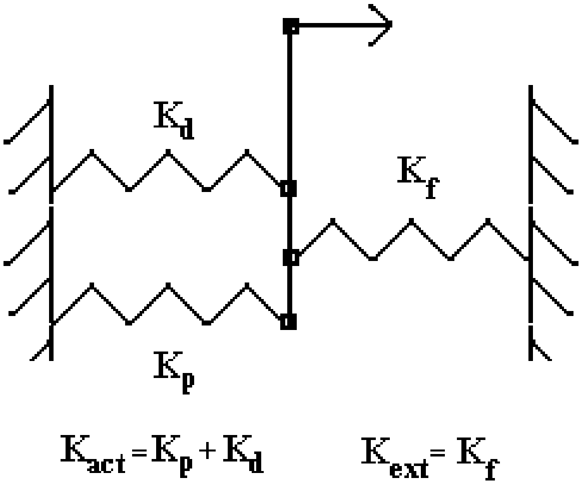

Figure 3.5 – Simplified Model of Actuator and Pumping Chamber

piezostack stiffness, K_p, the piston diaphragm stiffness, K_d, and the pumping chamber fluid stiffness, K_f. To illustrate the operation of the actuator under this condition, the force-displacement characteristic of the pumping chamber fluid is plotted on top of the actuator load line in Figure 3.6. The spring load line is designated by line segment OC. The intersection of the two lines at point C marks the equilibrium point of the spring system. As the input voltage increases or decreases and the actuator load line shifts, the equilibrium point moves along the line OC. Coordinates of the equilibrium point, C, can be found by substituting the external load stiffness into Eq. 3.8,

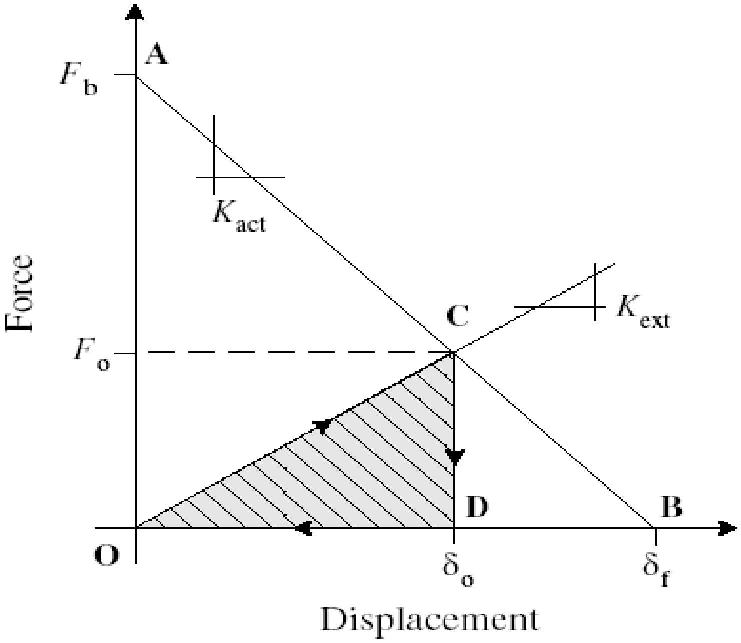

Figure 3.6 - Piezostack Load Line Plotted With External Fluid Stiffness

$$F_o = F_b - \delta_o K_{act} \qquad \text{Eq. 3.10}$$

$$F_o = \delta_o K_{ext} \qquad \text{Eq. 3.11}$$

Combining Eq. 3.10 and Eq. 3.11, the equilibrium displacement is found as,

$$\delta_o = \frac{F_b}{K_{ext} + K_{act}} \qquad \text{Eq. 3.12}$$

Considering a complete cycle, the equilibrium point moves back and forth along the OC line and no work is done by the actuator. Some energy is transferred to the external spring while the piezostack expands, but is transferred back as the piezostack contracts. To produce work from the piezostack, a method of retaining the energy transferred to the load must be utilized. In the case of the hydraulic-hybrid actuator, the external spring represents the stiffness of the fluid in the pumping chamber and through frequency rectification valves, the energy transferred to the fluid can be retained during the contraction cycle. The resulting load line is shown on Figure 3.6 as line OCDO, and the work done by the piezostack every half cycle is the area inside the load line. This value can be obtained geometrically as,

$$W_{act} = \frac{1}{2} F_o \delta_o \qquad \text{Eq. 3.13}$$

Substituting from Eq. 3.10 and Eq. 3.11, the work done by the actuator is,

$$W_{act} = \frac{1}{2} F_b^2 \frac{K_{ext}}{K_{ext} + K_{act}} \qquad \text{Eq. 3.14}$$

To find the maximum work output per cycle, Eq. 3.14 can be differentiated with respect to the external load stiffness and set to zero to find,

$$\frac{\partial (W_{act})}{\partial (K_{ext})} = 0 \Rightarrow K_{ext} = K_{act} \qquad \text{Eq. 3.15}$$

This means that the maximum energy that can be extracted from the actuator occurs when the stiffness of the external load matches the stiffness of the driving element itself. This is called impedance matching. Given an impedance matched condition, the maximum work that can be extracted from any driving element is proportional to the product of its blocked force and free displacement. The area under the load line can be used as a measure of the available energy of the driving element. The performance of several materials can then be compared on this basis with some normalization. For example, the performance of several piezostacks could be compared using the product of their blocked forces and free displacements normalized by their cross-sectional area [61]. A more detailed analysis of the quasi-static actuator performance can be found in Ref. 47.

Chapter 4: Magnetostrictive Material

Magnetostrictives are active materials that exhibit a change in dimensions in response to an applied external magnetic field. This is known as magnetostriction. All magnetic materials possess this property, but in most cases, the effect is small (10 ppm). This phenomenon has been known for some time. However, due to the minimal strain of most magnetic materials, their practical uses have been limited in the past. In the early 1970's, researchers from the Naval Ordnance Lab (NOL) began developing giant magnetostrictive materials such as Terfenol-D, capable of producing strains on the order of 2000 ppm. The development of giant magnetostrictives led to a wide range of practical applications for these materials such as sensors and solid-state actuators. Recently, these materials have been investigated as possible driving elements in hydraulic-hybrid actuators. Before determining their suitability in this type of application, however, it is important to understand the working principles of such a material.

Magnetostrictive materials possess the ability to convert magnetic energy into mechanical energy and vice versa. As an actuator, magnetostrictives transform magnetic energy, usually from a solenoid coil into mechanical energy in the form of an axial extension. This effect is called the Joule effect. Its counterpart, the Villari effect, is the transformation of mechanical energy, from an external force, to a magnetic energy generated in the material. Both of these effects are generated from the alignment of the magnetic domains in the material itself. Without any external influences, mechanical or magnetic, the magnetic domains in a magnetostrictive material will be aligned randomly as shown in Figure 4.1 for magnetic field, H=0.

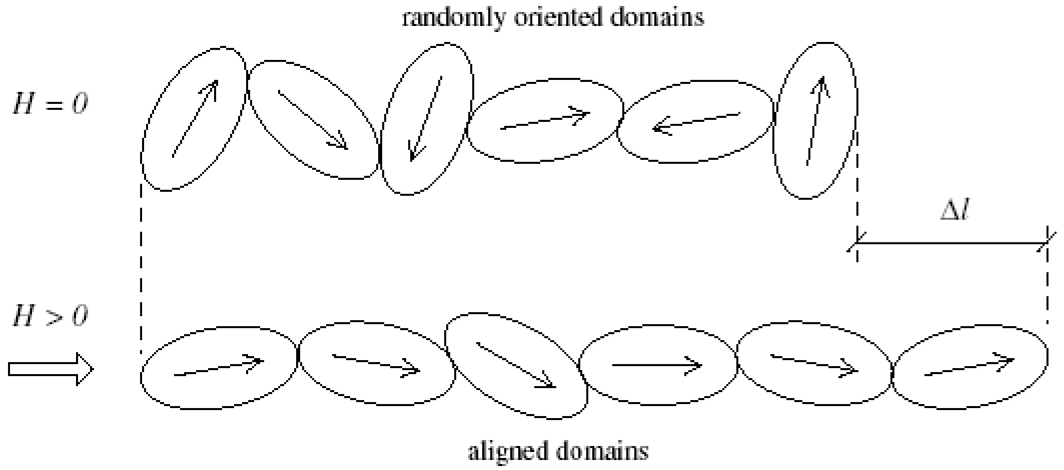

Figure 4.1 - Effect of Field, H, on Magnetostrictive Domains

When an external magnetic field is applied (H>0), the domains realign in the preferred orientation along the external magnetic induction, B, of the coil. This realignment causes a change in the length, Δl, of the material, as well as a net internal magnetic induction in the direction of the applied field. Similarly, an external force applied to a magnetostrictive material will realign the domains in the material causing an internal change in magnetic induction. In this way, the material can be used as a sensor, measuring the change in magnetic induction. Because the reorienting of the material domains occurs on the molecular level, the response time of the material is fast, and its bandwidth is large (~kHz).

The amount of preload on a magnetostrictive sample is of significant importance. The strain of a magnetostrictive rod for a given applied magnetic field increases substantially with an increase in preload up to some optimum point. A plot of typical values for a Terfenol-D rod, in Figure 4.2, shows the maximum induced strain increasing with higher prestress, with a loss in strain at lower magnetic fields. This

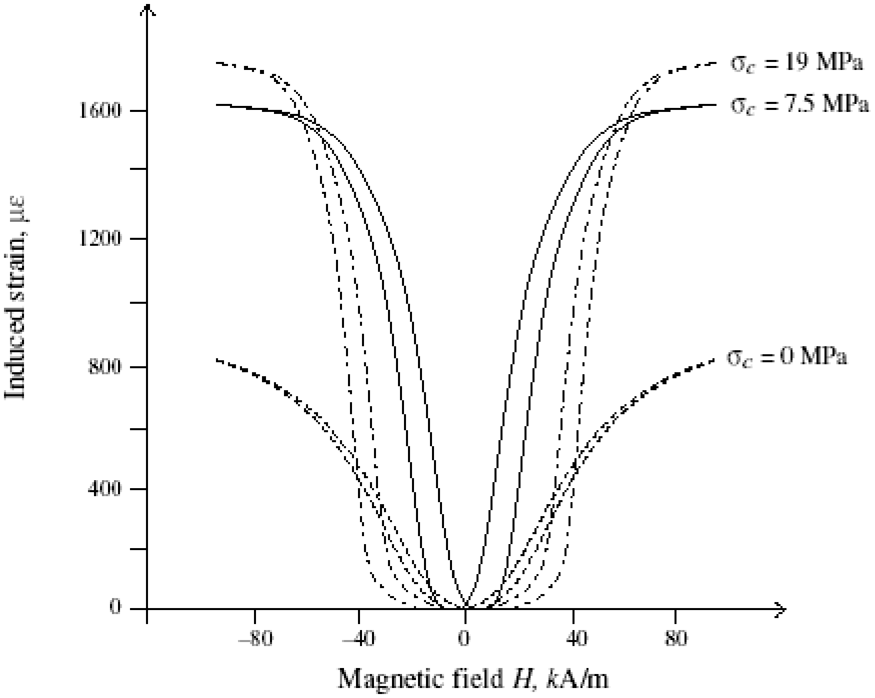

Figure 4.2 - Effect of Pre-Stress on Terfenol-D Magnetostriction [61]

effect is mainly due to the initial alignment of the rod's magnetic moments under some preload. The pre-stress causes the magnetic moments of the rod to line up perpendicular to the applied load. When a magnetic field is then applied in the axial direction, the moments rotate to align with the magnetic field, creating a larger net moment rotation and, therefore, larger strain [50]. This effect is shown in the diagram in Figure 4.3.

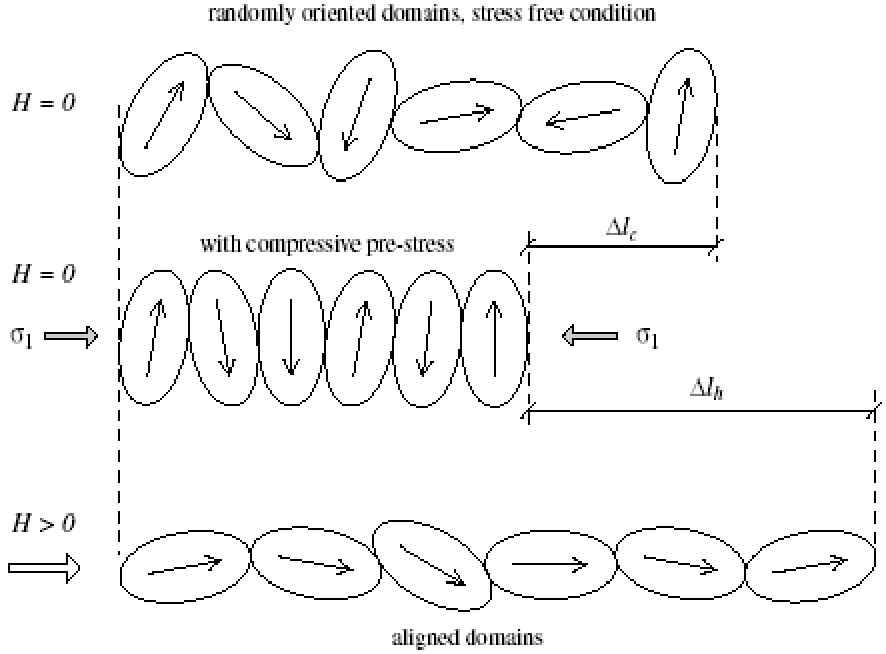

Figure 4.3 - Effect of Pre-Stress on Magnetic Domains

In addition to the longitudinal extension in length, the material also undergoes a lateral contraction. The net result is a zero change in net volume of the material. The change in length of the material, with respect to its normal dimensions, is always positive, regardless of the polarity of the applied magnetic field. Figure 4.4 shows the same effect of applying a positive or negative magnetic field to the material. In this way, the strain on the material has a quadratic dependence on the applied field, as shown in the plot in Figure 4.5. The nature of this relation means that it is not possible to get bipolar actuation from the material by applying a bipolar magnetic field. This type of actuation can be achieved, however, by applying a DC bias to the input field as shown in Figure 4.6. In this method, the materials 'natural' position has

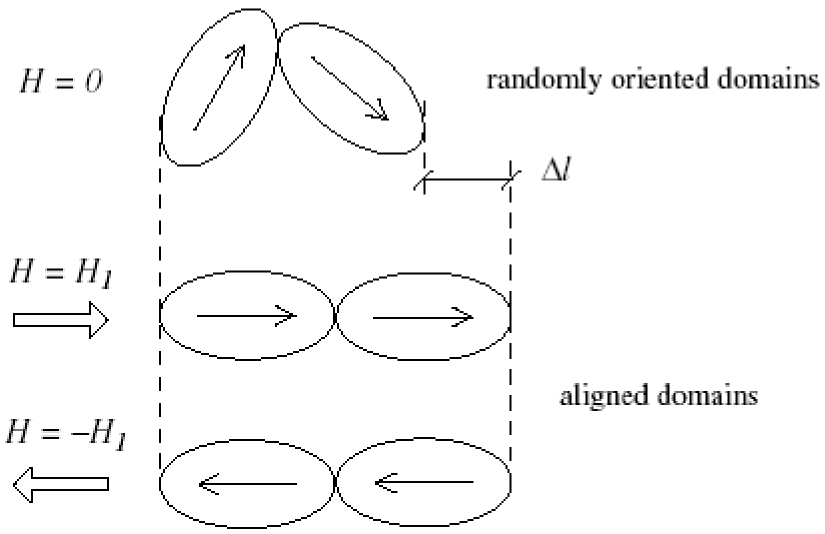

Figure 4.4 - Effect of Field Polarity on Induced Strain

the domains partially oriented along the axis of applied field. The material can then be expanded by applying a larger field or contracted by decreasing the field. A bias can be applied via a DC signal or through the use of permanent magnets in the flux path of the field. An alternate actuation method is to use a purely bipolar field. This type of actuation introduces a ‘frequency doubling’ effect to the actuation. For every cycle of applied magnetic field, the material will strain twice. The effect is that the actuation frequency of the material will be twice the frequency of the applied magnetic field. Because the amplifier used to actuate the magnetostrictive driving elements is unable to supply a bias, a purely bipolar field is used [61].

A comparison of Terfenol-D and Galfenol material properties is given in Table 4.1.

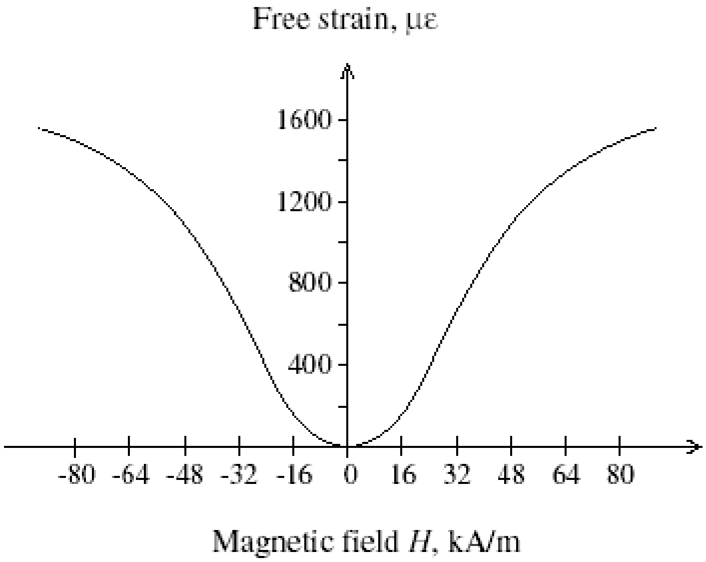

Figure 4.5 - 'Quadratic' Dependence of Strain on Field

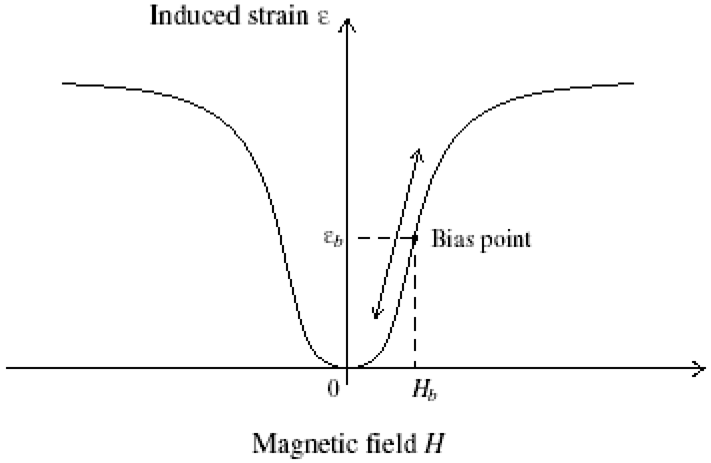

Figure 4.6 - Effect of Biased Field on Induced Strain

Magnetostrictive Material Properties		
	Terfenol-D	**Galfenol**
Length	2"	2"
Diameter	0.25"	0.25"
Magnetic Permeability	3-10	300
Free Strain	1000 ppm	300 ppm
Required Field for Max. Strain	80 kA/m	25 kA/m
Young's Modulus	10-100 Gpa*	30-57 Gpa*
Temperature Sensitivity	20% loss at 80 C	10% loss at 80 C
Robustness	Very Brittle	Machinable

Table 4.1 - Comparison of Terfenol-D and Galfenol Material Properties *Varies with stress and applied field

Chapter 5: Magnetostrictive Actuator Design and Testing

5.1 Actuator Design

In order to convert the existing piezoelectric pump into a magnetostrictive pump, several new parts were designed and fabricated. A simple sketch of the complete magnetostrictive actuator assembly is shown in Figure 5.1. For this actuator, a 0.25” diameter magnetostrictive rod of length 2” was used as the active element. Due to the high operating frequency at which the rod was to be actuated, a laminated rod was used to minimize eddy currents. A coil was designed and constructed to generate the magnetic field needed to actuate the Terfenol-D rod to an induced strain of 1000 ppm. Galfenol requires much less magnetic field than Terfenol-D due to its high magnetic permeability [51]. The coil design would therefore be efficient to drive a Galfenol sample. The coil has a length of 2 in., an outer diameter of 1 in., and an inner diameter of 0.27 in., allowing room for the 0.25 in. rod as well as strain gauges and a

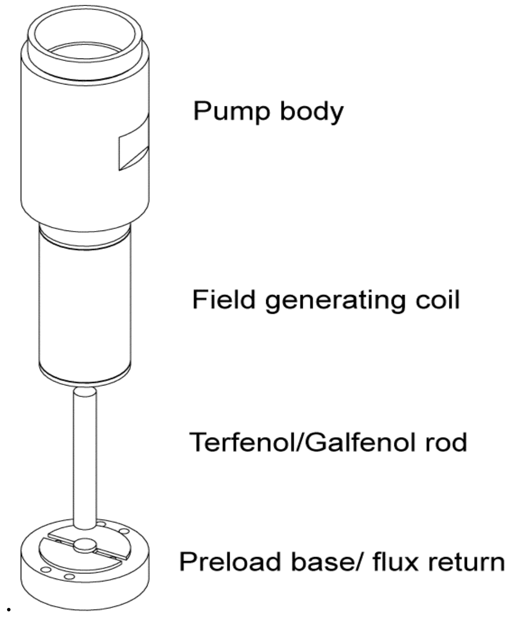

Figure 5.1 - Terfenol-D Actuator

surface-mounted thermocouple. About 362 turns of 32 gauge copper wire were wound at the base of a Delrin core to act as a flux sensor. About 2000 turns of 26 gauge copper wire were then wound over the sense coil as the magnetic field generator. The field-generating coil had a total resistance of about 12 ohms and a mass of 115 g.

Because the pump body needs to be ferromagnetic to complete the flux return path of the coil, a pump body was designed and built out of steel. The pump body has an inner diameter of 1 in. and a length of 2.5 in., allowing the field-generating coil to fit snugly inside it. At one end of the pump body, a steel piston is attached and remains in contact with one end of the Terfenol-D rod. At the other end of the pump body, a steel end cap completes the flux return path and is used as a preloading device on the magnetostrictive rod. The complete magnetic flux path is formed by the pump body, piston, magnetostrictive rod, and end cap. Slots were cut in the end cap to allow room for the coil wires and sensor wires. The slots were coated with insulation to prevent any shorting of the wires with the pump body. An exploded view of the magnetostrictive pump components is shown in Figure 5.2.

For this actuator, the magnetostrictive rod was pre-stressed to 4 ksi. In order to apply the preload, 4 screws connecting the end cap to the pump body were used. Strain gauges mounted on the rod in a Wheatstone bridge configuration allowed the exact amount of stress in the rod to be determined. Because Terfenol-D is a very brittle material, care was taken to evenly tighten the preload screws and apply only axial stress to the rod.

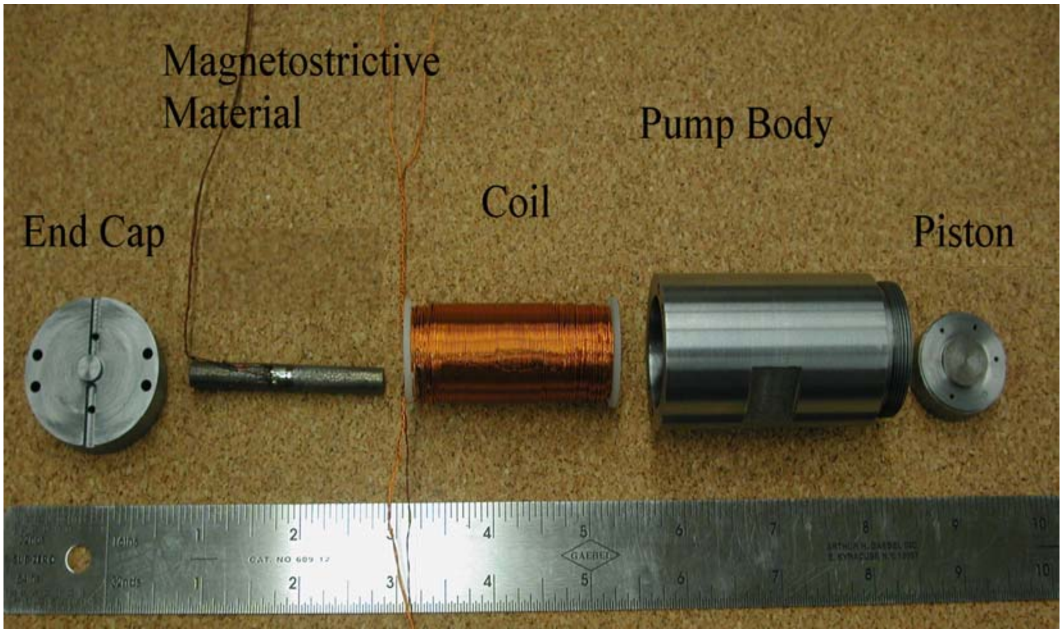

Figure 5.2 - Exploded View of Magnetostrictive Pump Components

5.2 Actuator Testing

Static Testing

Before testing the Terfenol-D actuator in the hydraulic pump, preliminary tests were carried out on the actuator to determine its performance. The first test was a quasi-static measurement of the magnetostrictive strain with varying amounts of current applied to the coil. The magnetostrictive rods were prestressed to 4 ksi, and a low frequency AC input was used to supply 4 amps peak to the field-generating coil with the Terfenol-D core, and 0.5 amps peak for the Galfenol core. The strain of both rods was measured using a surface mounted, full bridge strain gauge setup. The results of the test for Galfenol and Terfenol-D are plotted as strain against coil current in Figure 5.3 and Figure 5.4, respectively.

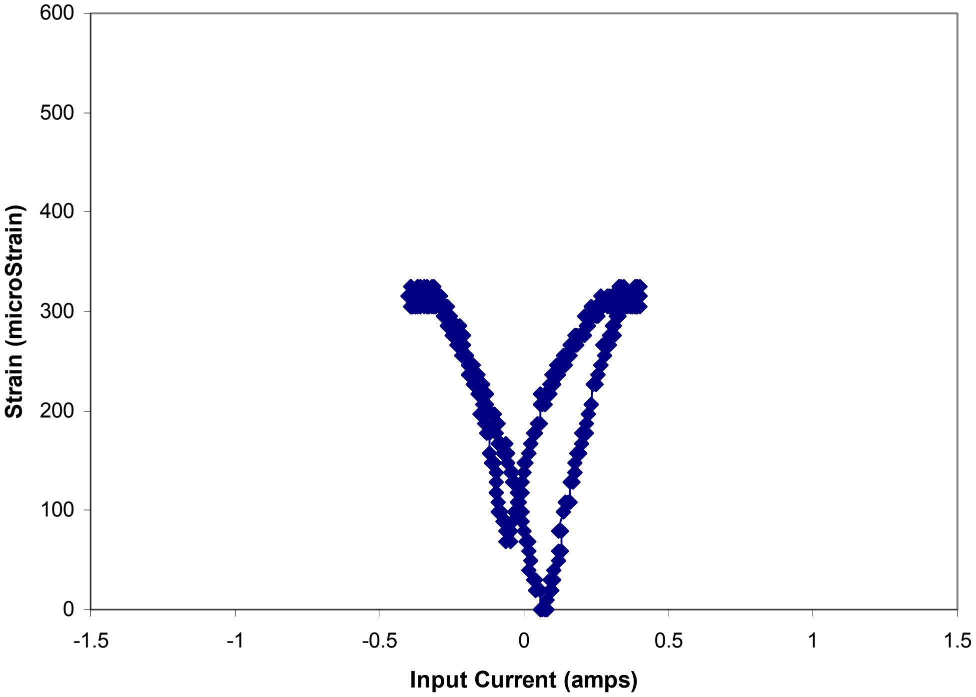

Figure 5.3 – Quasi-static Galfenol Strain Curve (No Output Load)

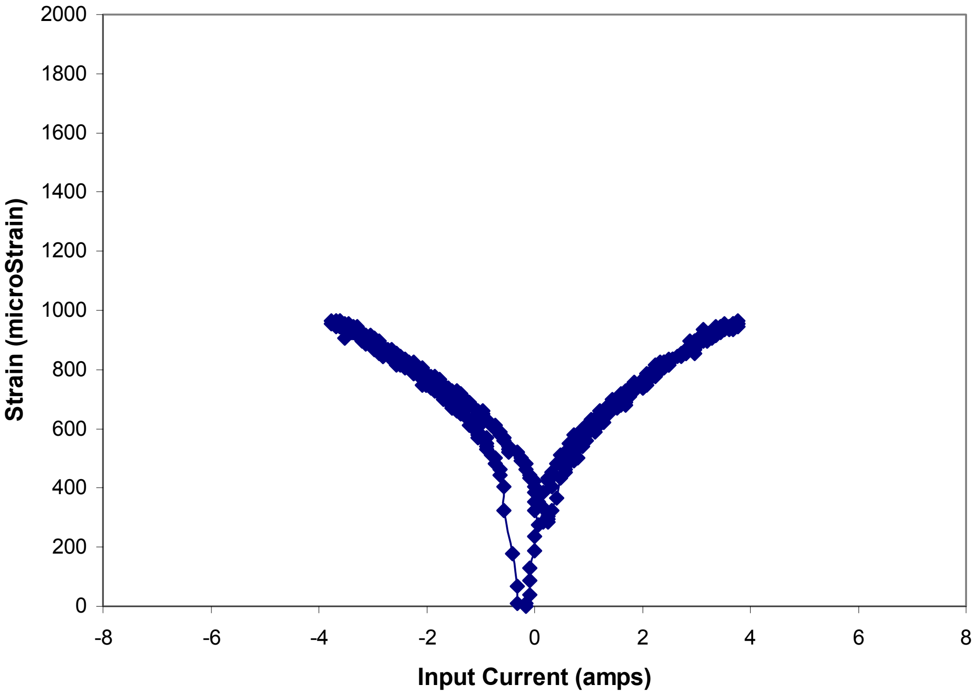

Figure 5.4 – Quasi-static Terfenol-D Strain Curve (No Output Load)

No-load Velocity Testing

To measure the flow rate of the magnetostrictive pump, uni-directional testing of the actuator was conducted with no output load. The pump was connected to the output cylinder and actuated with a sinusoidal voltage from a function generator that was amplified using a commercially available audio amplifier. The audio amplifier was unable to provide a DC bias to the coil of the actuator, and therefore a pure AC voltage was applied. Because the magnetostriction varies quadratically with the applied field, the amplifier acted as a frequency doubler, actuating the driving element for two cycles with every one cycle of input voltage. Note that frequencies shown in the following plots are the frequencies of the material actuation and not the current input. For these tests, the magnetostrictive sample was pre-stressed to 4 ksi, and the fluid (Hydraulic fluid – MIL-H-5606F) was pressurized to 200 psi. For the Terfenol-D actuator, tests were performed for three values of coil current, 2.5, 3, and 4 amps. The current through the coil was controlled by adjusting the gain of the audio amplifier at each frequency. The velocity of the output cylinder was measured using a linear potentiometer. The output shaft was returned to the start position manually after each test. The output velocities are plotted vs. actuation frequency for the Terfenol-D actuator in Figure 5.5.

The data were taken up to the point where the output of the amplifier saturated. The case where 4 amps were applied to the Terfenol-D actuator shows a large increase in performance over the other cases. The trend shows that the output cylinder would continue to reach higher speeds if the actuator was driven at higher frequencies.

However, the large power requirement of the coil at high frequencies limited the maximum frequency of actuation at high drive currents. The plot shows a variation of the resonant frequency of the actuator with driving current. The resonant peak of each curve varies from about 400 Hz to about 700 Hz. Repeated tests yielded the same results with variations of less than 5%.

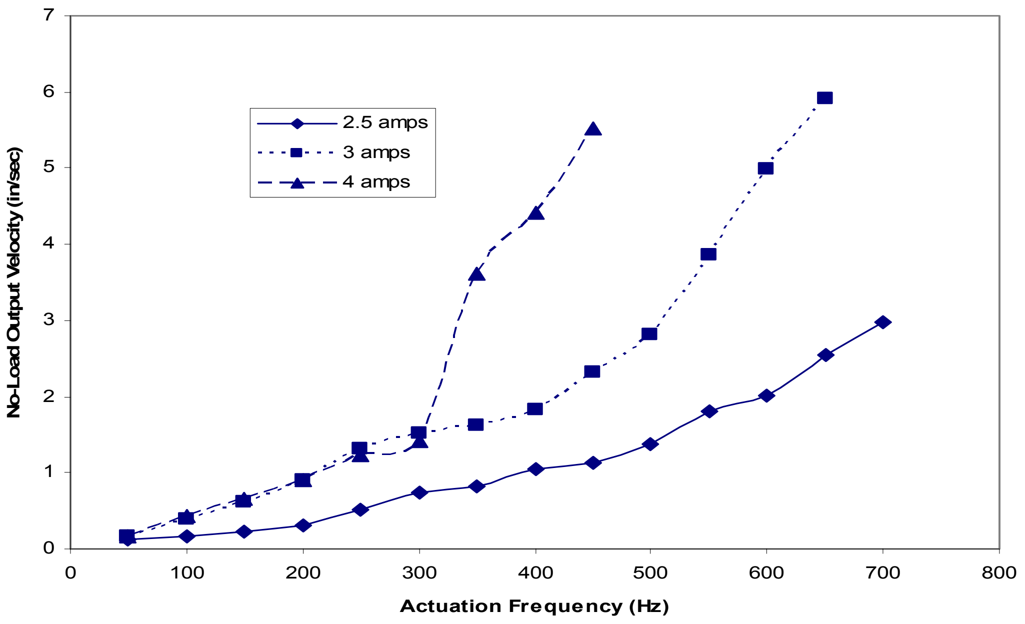

Figure 5.5 – No-load Velocity of Terfenol-D Actuator

Testing of the Galfenol driven pump failed to produce any movement in the output cylinder. It was hypothesized that the Galfenol failed to produce any fluid flow due to its low strain. To prove this theory, no-load tests were again performed for the Terfenol-D actuator. This time, a current of 1 amp peak was applied to the coil in order to induce the same amount of strain from the Terfenol-D rod as the maximum amount of strain from the Galfenol rod (250-300 $\mu\varepsilon$). Actuation at this current level from 0-1000 Hz failed to produce any output. The Terfenol-D actuator was then driven with increasing amounts of induced strain, while measuring the output velocity. The results are plotted in Figure 5.6. The plot shows that a minimum of

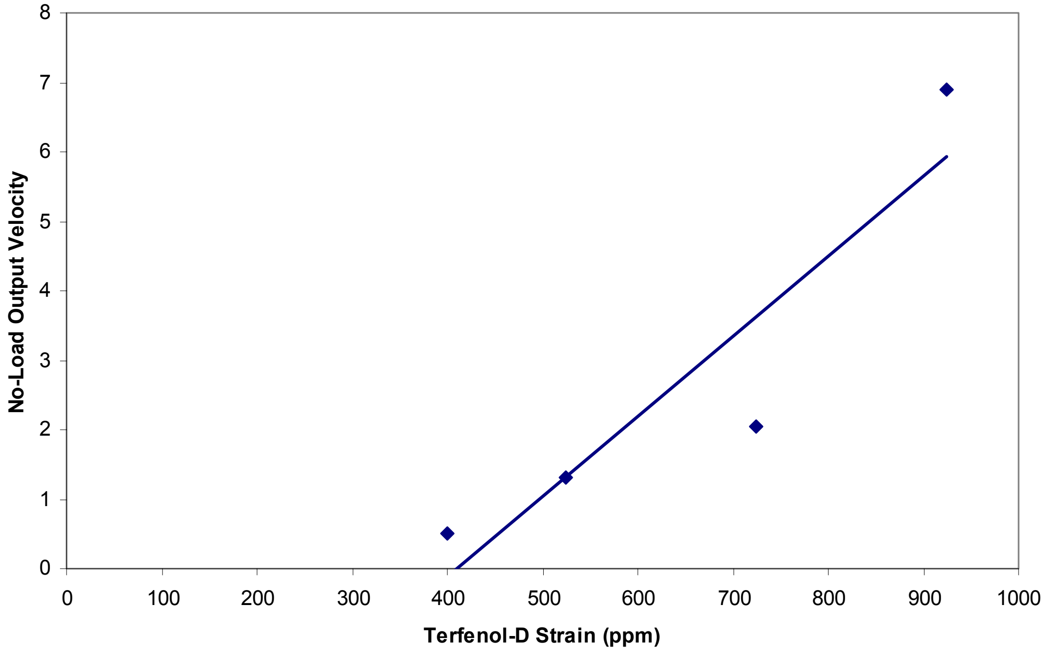

Figure 5.6 - No-load Velocity for Terfenol-D Actuator

about 400 $\mu\varepsilon$ is required to produce any output. It could then be concluded that the maximum strain of the Galfenol actuator was not sufficient to overcome viscous and stiffness losses of the fluid in the actuator. Figure 5.6 suggests that a strain of 400 $\mu\varepsilon$ is required to overcome these losses. Using Galfenol in a pump with alternate pumping chamber dimensions could generate enough flow rate to overcome the internal losses of the actuator. Increasing the piston diameter of the actuator would generate more fluid flow per cycle for a given material strain while increasing the stiffness of the fluid. Because Galfenol has a higher blocked force and lower free strain than Terfenol-D, a larger piston diameter would create a condition where the impedance of the Galfenol rod and pumping chamber fluid are more closely matched. This would extract more work from the Galfenol and create a more efficient actuator. In the present pump setup, however, a 2 inch Galfenol rod with 300 $\mu\varepsilon$ does not displace enough fluid to overcome fluid losses in the actuator and generate any output. For the remaining experiments, only Terfenol-D will be tested in the actuator.

Blocked Force Testing

To determine the blocked force characteristics of the Terfenol-D actuator, further uni-directional tests were conducted. Pumping frequency was held constant this time, and the output load was plotted against output velocity. Weights were hung from the output shaft to create a load on the actuator. A linear potentiometer was used to measure the loaded velocity of the output shaft. The current through the coil was held at 4 amps throughout the tests. Tests were conducted for actuation frequencies of 150 Hz, 200 Hz, and 250 Hz. Results from these tests are shown in Figure 5.6. The blocked force was extrapolated from the experimental data by means of a linear fit. The plots show that the blocked force of the actuator is about 10 lbs., and is independent of the pumping frequency. For low frequencies, below resonance, the unloaded velocity is expected to be linear with pumping frequency [44]. At these frequencies, the flow rate of the pump is simply a product of the piston displacement and pumping frequency. The data plotted here are in good agreement with expected trends.

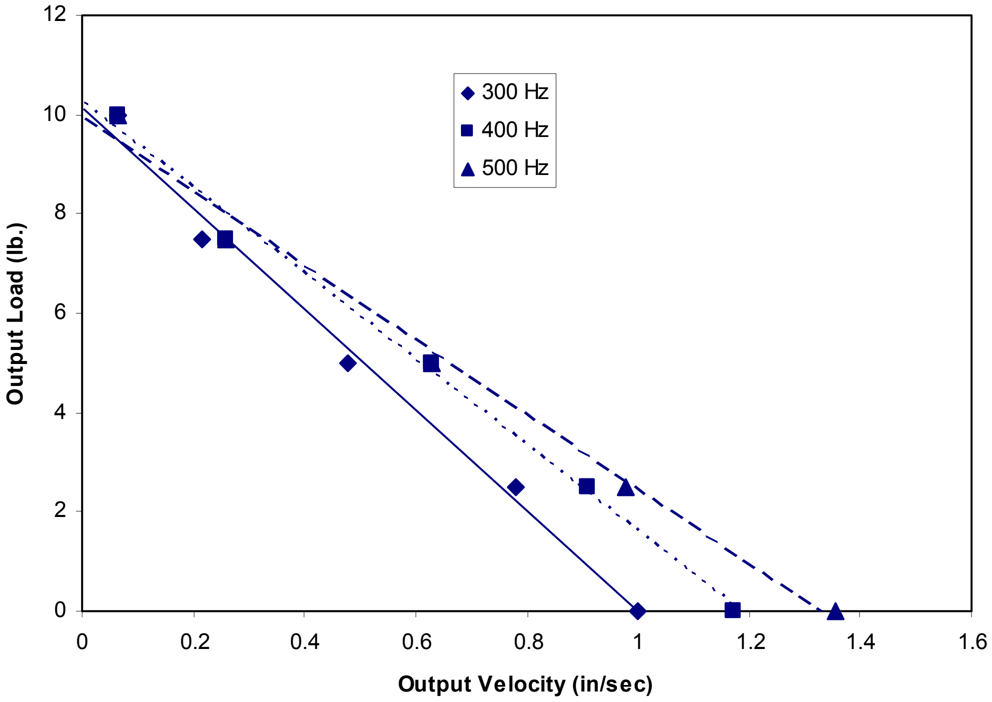

Figure 5.6 - Terfenol-D Actuator Blocked Force

Self Heating

An important characteristic of a high frequency actuator is its self heating. As the operating temperature increases above room temperature, the magnetostriction of Terfenol-D decreases somewhat due to a lowered magnetostriction saturation. These performance issues become more significant at higher temperatures until at the Curie temperature the material becomes paramagnetic [49]. In addition, the heating of the field-generating coil could be significant and further increase temperature levels. For these reasons, it was important to test the heating characteristics of the actuator while driven at high frequencies. A thermocouple was mounted to the surface of the Terfenol-D sample to measure temperature. Although the temperature on the surface of the rod would not exactly represent the temperature at the core, the approximation was considered acceptable for this experiment. The actuator was excited in the same manner as for the unidirectional tests at various frequencies while steady state temperatures were recorded from the thermocouple. The test was carried out for current levels of 1 amp, 1.5 amps, and 2 amps supplied to the coil. The steady state temperatures of the Terfenol-D rod are shown as a function of driving frequency for the three values of coil current in Figure 5.7.

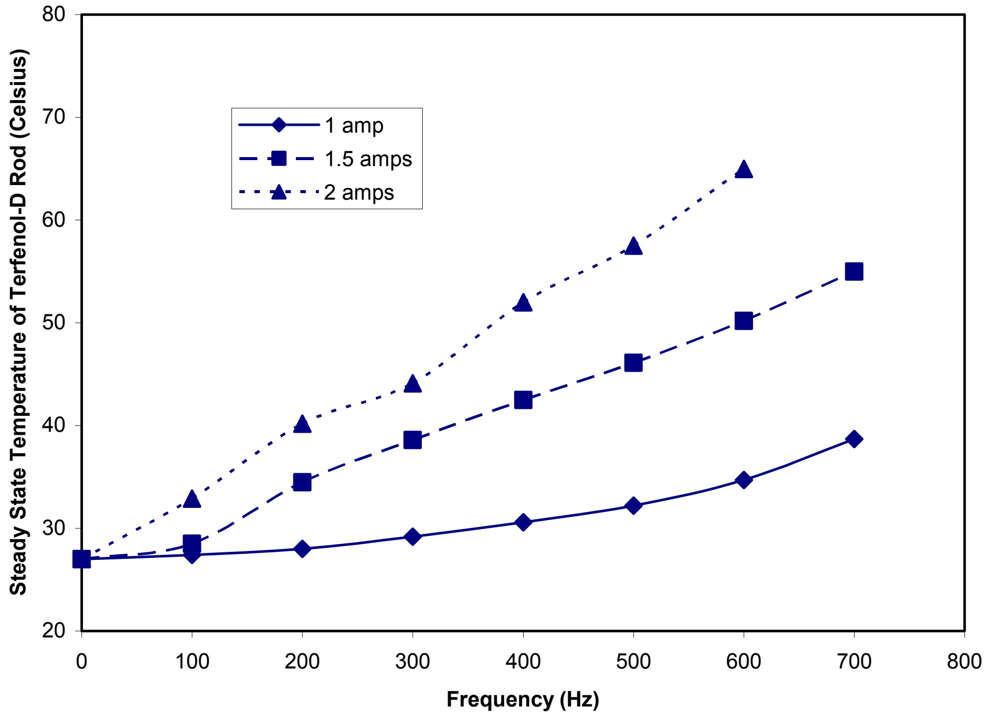

Figure 5.7 - Self Heating of Terfenol-D Actuator

At 2 amps of coil current, high levels of heating were noted not only on the sample, but also in the field generating coil of the actuator. This could be due to significant power losses from eddy currents forming in the pump body. Due to the alternating magnetic induction in the actuator, eddy current loops are set up in the flux return path which produce a magnetic induction opposite to that of the induction produced by the coil [61]. This results in power losses through ohmic heating in the pump body, as well as an increased required current for a given level of induced strain. Testing at higher levels of induction was not conducted due to concerns of damaging the active material. Clearly, self heating could be a significant problem when the coil is driven with high currents.

5.3 Conclusions

The overall performance of the magnetostrictive actuator was comparable to the existing piezo pump, with several short comings.

i. The high power required from the actuator at high frequencies is a major problem. Due to amplifier limitations, the highest drive current that could be supplied was 4 amps at 450 Hz. This falls well short of the resonant peak of the fluid system.

ii. The high velocities achieved show promising results for the magnetostrictive actuator. Because the coil had a high inductance, actuation at high frequencies (500-1000 Hz) required high levels of power. The amplifier used was unable to supply the required power, and the achievable actuation frequency was limited to 700 Hz. A coil with lower inductance could reach higher output powers at higher frequencies.

iii. The Terfenol-D actuator also showed less blocked force than the piezostack actuator. This is a result of the lower active material stiffness and smaller cross-sectional area of the Terfenol-D actuator.

iv. The Terfenol-D actuator produced significant amounts of heat when actuated at a steady state for low values of coil current. As previously stated, this is probably due to eddy currents and the power losses they incur.

With several lessons learned from the initial attempt at developing a magnetostrictive actuator, it was prudent to design and develop a new actuator. The first step in the new design was to perform an analysis to determine the properties and characteristics of various coil configurations so that an optimum coil could be built for this actuator.

Chapter 6: Magnetostrictive Actuator Coil Design

In order to build a more efficient actuator using magnetostrictive materials, a coil design analysis was performed to better understand the properties of this type of actuator. The starting point for this analysis is the simple sketch of such an actuator as shown in Figure 6.1. The analysis will use a Terfenol-D rod as the core of the coil, as well as the pump body and coil dimensions shown in the diagram. Since Galfenol has been ruled out as a possible driving material, the actuator is designed to meet the requirements of Terfenol-D actuation only. Since the dimensions of the actuator body and magnetostrictive material are fixed, many suitable coils can be wound with varying wire thickness and number of turns. The following is a simple algorithm that can be used to generate coil dimensions based on a required amount of strain.

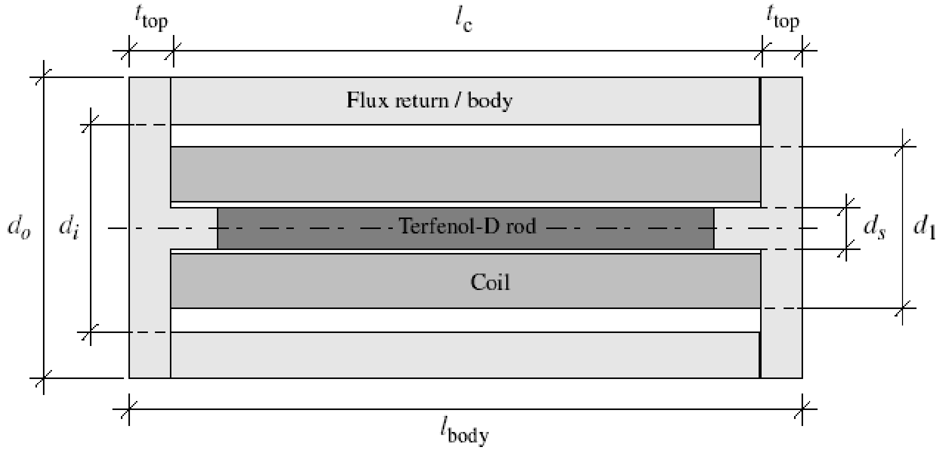

Figure 6.1 - Diagram of Magnetostrictive Actuator

6.1 Coil Design Algorithm

The first step in designing a coil is to determine the amount of magnetic field, H_s, required by the magnetostrictive material for the specified amount of strain. This can be determined from experimental H-Λ curves, where Λ is the strain of the material.

The next step is to calculate the magnetomotive force, mmf, generated by the magnetic circuit for the given applied magnetic field. This can be estimated using an equivalent of Ohm's law for magnetism, where the mmf is equal to the flux in the circuit multiplied by the sum of the reluctances in the circuit. The mmf is given by

$$mmf = H_s l_s \frac{R_c + R_s}{R_s} = N_{tot} i_w \qquad \text{Eq. 6.1}$$

where l_s is the length of the magnetostrictive material, N_{tot} is the total number of coil turns, and i_w is the current passing through the coil. R_c and R_s are the reluctances of the magnetic circuit and the magnetostrictive material, respectively. The reluctance of the two components is based on the magnetic permeability of the material, μ. The magnetic permeability represents the relation of magnetic induction to applied field for a material and is given by

$$\mu = \frac{\Delta B}{\Delta H} \qquad \text{Eq. 6.2}$$

The higher a material's magnetic permeability, the lower its reluctance will be. For example, Galfenol's permeability is on the order of 300, while Terfenol-D's permeability is only about 3-10 [49-51]. This means that the reluctance of a Terfenol-D rod in the magnetic circuit will be much higher than the reluctance of a Galfenol rod. Magnetic permeability of a material is not constant and varies with applied field as shown in Figure 6.2. If a large enough magnetic field is applied to the material, all of the magnetic domains in the material will become aligned. The

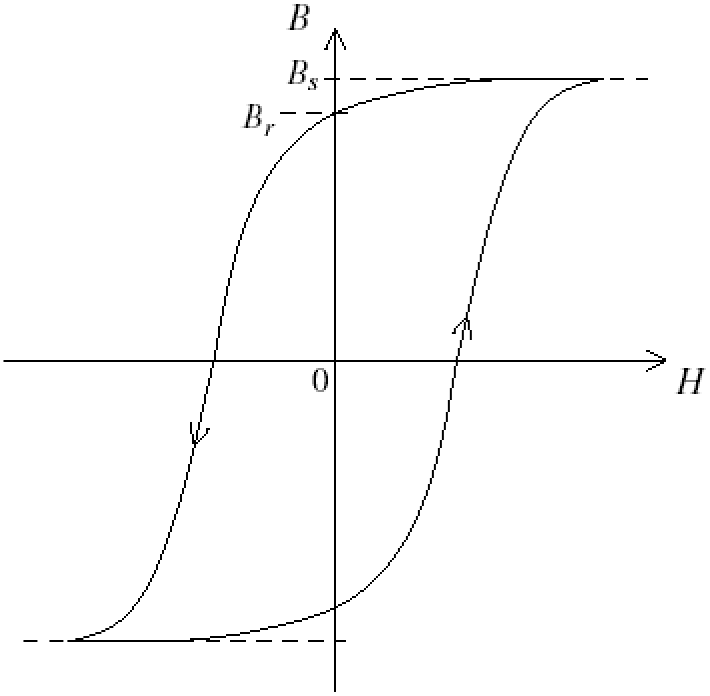

Figure 6.2 - Typical B-H Curve of Magnetostrictive Material

material is said to be in a state of saturation, where its magnetic induction is at a maximum, B_s, and applying a larger magnetic field will have no effect. At this point, the permeability of the material will become small, drastically increasing the material's reluctance. Upon removal of the applied field, some of the domains will remain aligned, leaving a remnant induction, B_r, and leading to magnetic hysteresis.

Usually, 1018 steel, which is used for the actuator body and magnetic circuit, would have a much lower reluctance than either Terfenol-D or Galfenol, making its effect negligible for this calculation. However, it is important to ensure that the field required by the magnetostrictive material will not cause the material in the magnetic circuit flux return path to approach saturation. This will ensure that the reluctance of the flux path is as low as possible. Saturation can generally be avoided by having an adequately sized actuator body. This requirement is typically satisfied just by sizing the pump body to meet stiffness requirements. Therefore, if the pump body is stiff enough not to absorb energy from the actuating magnetostrictive material (~10x material stiffness), it will not approach saturation. This was verified using simple reluctance calculations.

Even in an unsaturated state, the actuator body has air gaps and flux leakage points, where connections to other parts of the actuator are made, which make its reluctance significantly larger. We can relate R_c and R_s as follows. For a Terfenol-D rod, $R_c < R_s$, and for a Galfenol rod, $R_c \cong R_s$. For the purposes of this design, an empirical formula is used to calculate the mmf as

$$mmf = 1.05 H_s l_s = N_{tot} i_w \text{ for Terfenol-D} \qquad \text{Eq. 6.3}$$

$$mmf = 2 H_s l_s = N_{tot} i_w \text{ for Galfenol} \qquad \text{Eq. 6.4}$$

Next, a formula for the coil geometry can be determined. The actuator volume available for the coil is fixed from the existing actuator body dimensions. The actuator body has an inner diameter, d_i, of 1 inch, and a length, l_c of 2 inches. For a given wire diameter, d_w, the number of turns per layer, N_t, of winding can be determined by

$$N_t = \frac{l_c}{d_w} \qquad \text{Eq. 6.5}$$

The number of layers in the coil, N_l, is bound by the inner diameter of the actuator body and the diameter of the magnetostrictive material, and is obtained by

$$N_l = \frac{d_1 - d_s}{2d_w}; \text{ for } d_i \geq d_1 \geq d_s \qquad \text{Eq. 6.6}$$

where d_1 is the outer diameter chosen for the coil. The total number of turns in the coil, N_{tot}, is the product of the turns per layer and number of layers.

With the physical dimensions of the coil determined, the inductance and resistance of the coil, and the current required to produce the specified mmf can be calculated. The inductance is found using the formula,

$$L = \frac{\mu N_{tot}^2 A}{l_c} \qquad \text{Eq. 6.7}$$

where A is the cross-sectional area inside the coil. To calculate the resistance of the coil, the total length of wire in the coil, l_w, must first be determined. This can be found from the coil dimensions as

$$l_w = 2\pi \left(\frac{d_1 + d_s}{2} \right) N_{tot} \qquad \text{Eq. 6.8}$$

All calculations using the coil geometry are estimations and imperfections in the coil winding are not taken into account. This approximation becomes less accurate as the wire thickness increases. For an initial design study, the approximation is acceptable. The resistance of the coil can now be calculated as

$$R_w = \frac{\rho_w l_w}{A_w} \quad \text{Eq. 6.9}$$

where A_w is the cross-sectional area of the wire, and ρ_w is the resistivity of the wire. The current required by the coil to produce the specified mmf can be found from the previous equation of

$$i_w = \frac{mmf}{N_{tot}} \quad \text{Eq. 6.10}$$

With the required current and the coil properties, the voltage and power required for the coil can now be determined as a function of the operating frequency, ω. The voltage required, V_w, is given by

$$V_w = i_w Z \quad \text{Eq. 6.11}$$

$$V_w = i_w \sqrt{R_w^2 + w^2 L_w^2} \quad \text{Eq. 6.12}$$

where Z is the total impedance of the coil. The power required for the coil, P_w, is given by

$$P_w = i_w^2 Z \quad \text{Eq. 6.13}$$

$$P_w = i_w^2 \sqrt{R_w^2 + w^2 L_w^2} \quad \text{Eq. 6.14}$$

Since the inductive part of a coil does not dissipate power, but stores the energy in the magnetic field, only the resistive part of the coil contributes to the heat produced in the coil, P_d, which is given by

$$P_d = i_w^2 R_w = \frac{mmf^2}{N_{tot}^2}\frac{\rho_w l_w}{A_w} \qquad \text{Eq. 6.15}$$

$$P_d = 4\rho_w (mmf)^2 \frac{(d_1 + d_s)}{(d_1 - d_s) l_c} \qquad \text{Eq. 6.16}$$

The equation shows that for minimum dissipated power, d_1 should be as large as possible. Therefore, the coil should fill the entire actuator body ($d_1 = d_i$). It can also be seen from this analysis that the power dissipated by the coil is independent of the wire diameter. Similarly, by substituting for L_w and R_w, it can be seen that the total power required is independent of the wire diameter:

$$P_w = \sqrt{i_w^4 R_w^2 + i_w^4 w^2 L_w^2} \qquad \text{Eq. 6.17}$$

$$P_w = \sqrt{\left[4\rho_w (mmf)^2 \frac{(d_1 + d_s)}{(d_1 - d_s) l_c}\right]^2 + \left[w (mmf)^2 \frac{\mu_s^2 \pi d_s}{4 l_c}\right]^2} \qquad \text{Eq. 6.18}$$

The required voltage, however, will increase with decreasing wire diameter for a given operating frequency:

$$V_w = \sqrt{i_w^2 R_w^2 + i_w^2 w^2 L_w^2} \qquad \text{Eq. 6.19}$$

$$V_w = \sqrt{\left[2(mmf)\rho_w \frac{(d_1 + d_s)}{d_w}\right]^2 + \left[\frac{w(mmf)}{8}\frac{\mu_s \pi d_s^2 (d_1 - d_s)}{d_w^2}\right]^2} \qquad \text{Eq. 6.20}$$

Finally, the total mass of the actuator body and coil, M_b and M_w, can be calculated as,

$$M_b = \rho_b \left[2\frac{\pi d_o^2}{4} t_{top} + \frac{\pi (d_o^2 - d_i^2)}{4} l_c\right] \qquad \text{Eq. 6.21}$$

$$M_w = \rho_w l_w A_w = \frac{\rho_w}{16} \pi^2 (d_1^2 - d_s^2) l_c \qquad \text{Eq. 6.22}$$

where ρ_b is the density of the body material, and ρ_w is the density of the wire material. The mass of the magnetostrictive sample is neglected compared to the mass of the actuator body and coil. The total mass of the actuator is then the sum of the body mass and coil mass. Again, the total mass is independent of the wire diameter.

For various wire diameters, values of coil impedance, power required, voltage and current required, etc., can be calculated. From power limitations such as maximum voltage or current, a suitable wire gauge and coil configuration can be chosen. This algorithm was run for several values of wire diameter, using the dimensions of the current actuator setup. Data required for the calculations are:

- General Data
    - Required strain: 1000 $\mu\varepsilon$
    - Design operating frequency: 500 Hz
- Terfenol-D rod
    - Length l_s : 50.8 mm (2”)
    - Diameter d_s : 6.35 mm (0.25”)
- Body
    - Material: 1018 Steel
    - Density: 7850 kg/m^3
    - Relative permeability μ_b : 1000
    - Saturation magnetic induction $B_{sat,1018}$: 1.5 T

  - Outer diameter d_o : 35.56 mm (1.4")
  - Body wall thickness: 5.08 mm (0.2")
  - End cap thickness: 7.62 mm (0.3")
- Coil wire
  - Density: 8906 kg/m^3
  - Resistivity: 1.72 x 10^{-8} ohm-m

Based on the H-Λ curves for Terfenol-D, a magnetic field of H_s= 60 kA/m was required to induce a strain of 1000 ppm [48]. This led to a required mmf of:

$$mmf = i_w N_{tot} = 1.05 H_s l_s = 3200.4\, amp - turns \qquad \text{Eq. 6.23}$$

Next, the length of the coil was determined to be 2.2" due to available space inside the pump body. Assuming a coil wound to fill the entire pump body (condition for minimum power dissipated), the number of turns in the coil can now be calculated for various wire gauges. The inductance and resistance of the coil can then be found based on the coil properties. The current required by the coil for the specified mmf can be found by dividing the mmf by the number of turns in the coil. The current can then be used to determine the voltage and power required by the coil. The mass of the actuator can also be determined from the physical characteristics of the coil and actuator body. The power dissipated by the coil and the coil mass are calculated as:

$$P_d = 4\rho_w (mmf)^2 \frac{(d_1 + d_s)}{(d_1 - d_s) l_c} = 64.37 \text{ W} \qquad \text{Eq. 6.24}$$

$$M_w = \frac{\rho_w}{16} \pi^2 (d_1^2 - d_s^2) l_c = 169 \text{ g} \qquad \text{Eq. 6.25}$$

The actuator body mass is calculated to be 462 g. The required current and voltage at an actuation frequency of 500 Hz are plotted against various wire gauges in Figure 6.3 and Figure 6.4, respectively. The drastic decrease in current is due to the increased number turns with higher wire gauges. The increased number of turns means that less current will be required for a given mmf and induced strain.

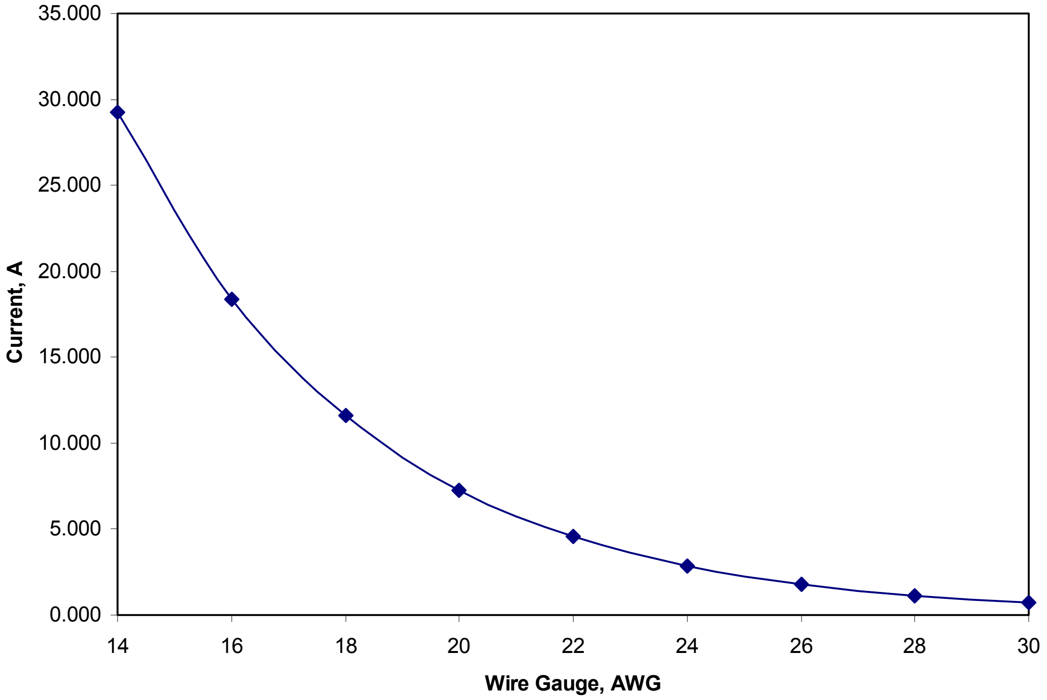

Figure 6.3 – Coil Current Required at 500 Hz and MMF = 3200 Amp-Turns

The voltage required increases with increasing wire gauge because an increase in number of turns results in a more inductive coil, and a higher coil impedance at high actuation frequencies. This effect is much less apparent at a lower operating frequency, as shown in Figure 6.4, where the voltage is also plotted at an operating frequency of 100 Hz. Note that the required current is kept the same.

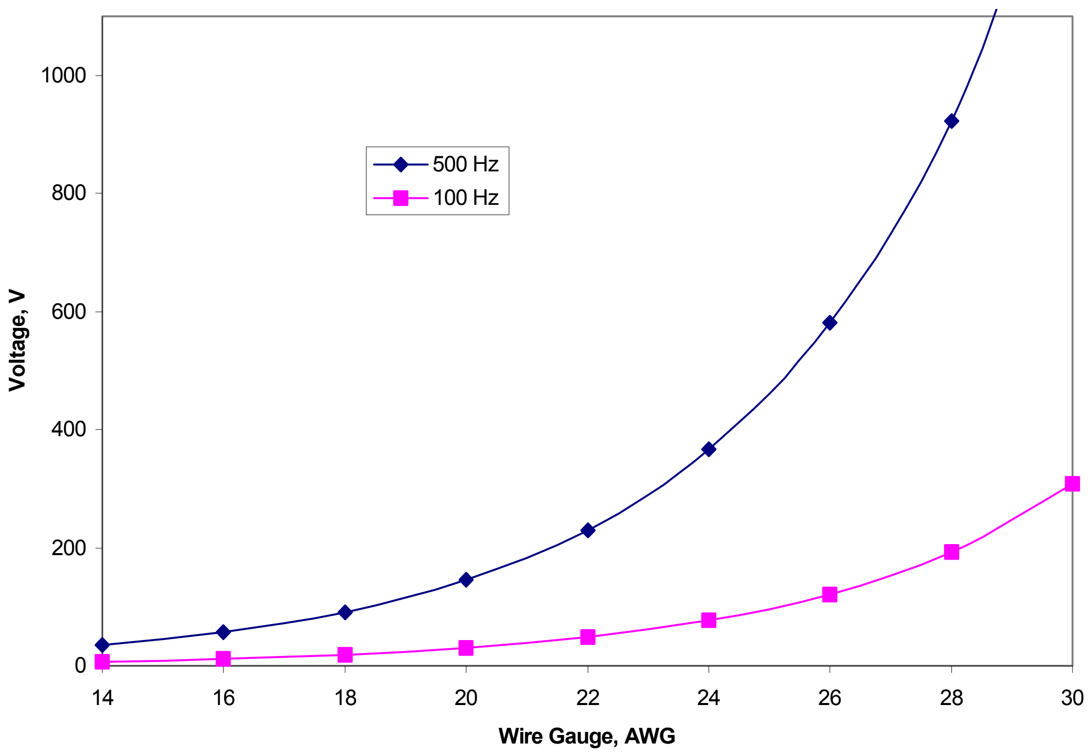

Figure 6.4 – Coil Voltage Required at 500 Hz and MMF=3200 Amp-Turns

In addition, we can define a winding ratio, $W_r = \frac{(d_1 - d_s)}{(d_i - d_s)}$, that represents the fraction of the actuator body that is filled with the windings. For $W_r = 1$, the body is filled, and the coil has its maximum diameter. The previous calculations can be repeated for $0 \le W_r \le 1$. The general trends are shown in the figures below. Figure 6.5 shows the power dissipated in the coil as the winding ratio is increased. The optimum point is where the actuator body is completely filled ($W_r = 1$), as stated previously. At this point, the power dissipated is at a minimum. Figure 6.6 shows the mass of the coil with varying winding ratio. By not completely filling the actuator body with the coil, the actuator can be made lighter. However, a smaller diameter coil will have fewer turns, resulting in more required current for a given mmf. This increased current

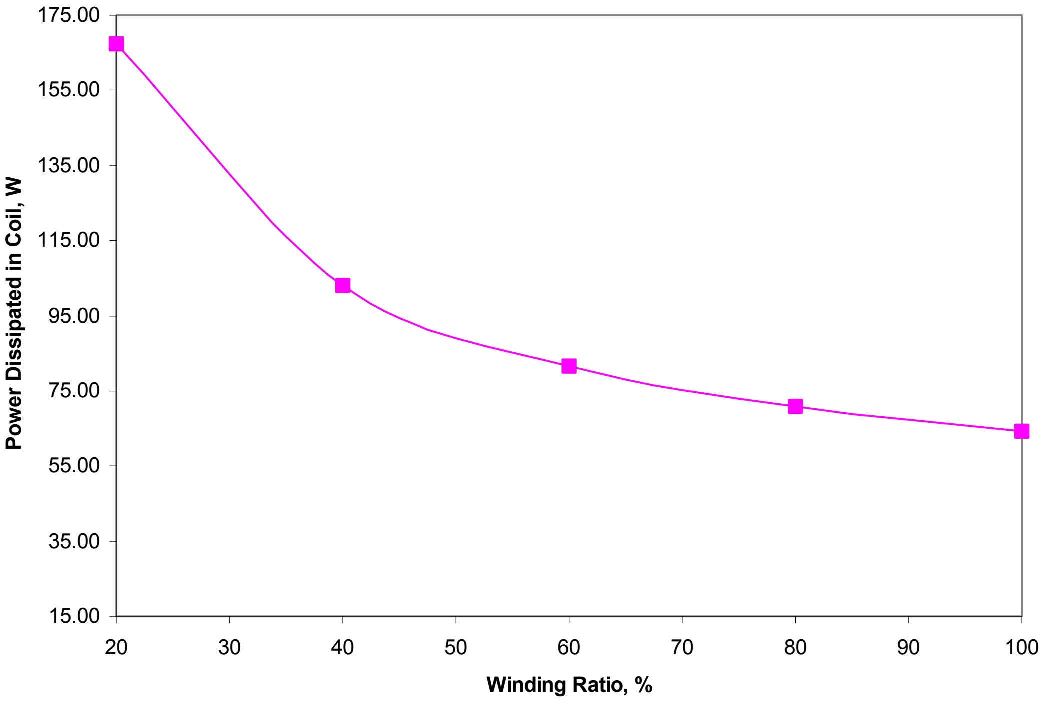

Figure 6.5 - Power Dissipated Vs. Winding Ratio

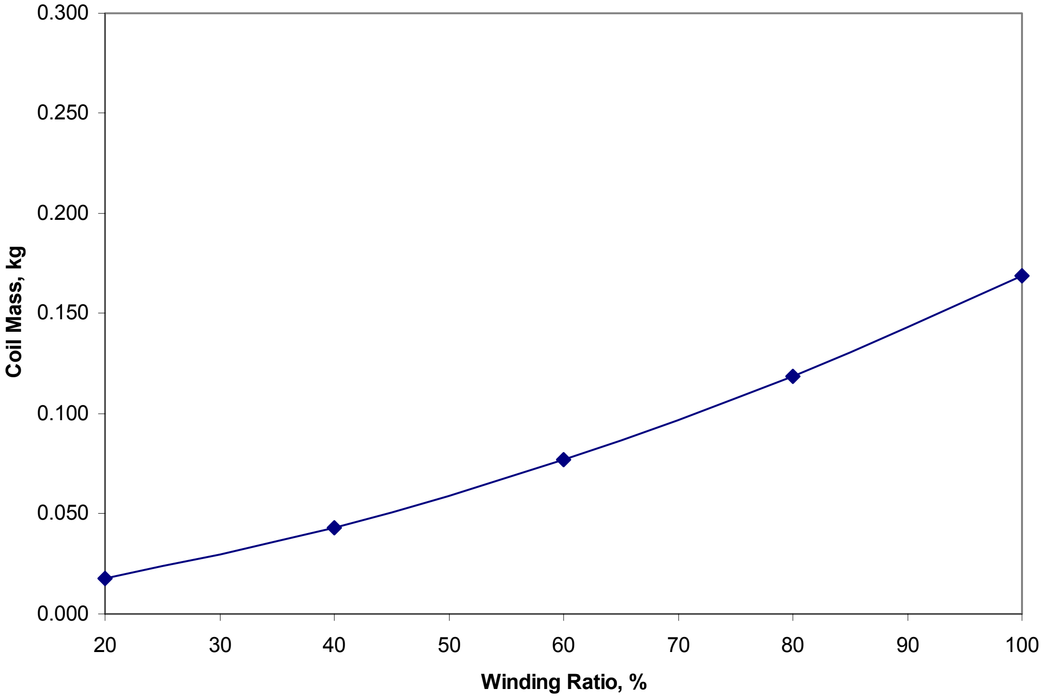

Figure 6.6 - Coil Mass Vs. Winding Ratio

requirement is what drives the dissipated power up at lower winding ratios. The coil mass is only about 35% of the entire actuator mass, and at this stage of development, the actuator’s mass is less important than its power requirements, therefore, a winding ratio of 1 can be assumed to achieve the optimum point [61].

Chapter 7: Magnetostrictive Actuator Characterization

The initial coil design showed good overall performance but was limited in its operating frequency range and produced a large amount of heat. It was necessary to design a more ideal coil specifically for actuating Terfenol-D. The coil analysis showed that winding a coil with high gauge wire (small wire diameter), increases the inductance of the coil. From the formula for coil inductance, it can be seen that the inductance is proportional to the total number of turns in the coil and, therefore, inversely proportional to the 4th power of the wire diameter,

$$L = \frac{\mu N_{tot}^2 A}{l_c} = \frac{\mu A}{l_c}\left(\frac{l_c\left(d_1 - d_s\right)}{2d_w^2}\right)^2 \qquad \text{Eq. 7.1}$$

The plot in Figure 7.1 shows the relation of coil inductance to wire gauge (AWG) for a Terfenol-D core actuator. In addition to increasing the inductance, decreasing the wire diameter of the coil will also increase the DC resistance of the coil due to the added length of the wire and smaller cross-sectional area. The resistance of a coil is inversely proportional to the 4th power of the wire diameter as shown in the equation,

$$R_w = \frac{\rho_w l_w}{A_w} = \frac{\rho_w 2\pi\left(\frac{d_1 + d_s}{2}\right)\left(\frac{l_c\left(d_1 - d_s\right)}{2d_w^2}\right)}{\pi\frac{d_w^2}{4}} \qquad \text{Eq. 7.2}$$

The total coil impedance can then be calculated as a function of wire diameter,

$$Z = \sqrt{R_w^2 + w^2 L^2} = \sqrt{\left[\frac{\rho_w 2\pi\left(\frac{d_1 + d_s}{2}\right)\left(\frac{l_c\left(d_1 - d_s\right)}{2d_w^2}\right)}{\pi\frac{d_w^2}{4}}\right]^2 + w^2\left[\frac{\mu A}{l_c}\left(\frac{l_c\left(d_1 - d_s\right)}{2d_w^2}\right)^2\right]^2} \qquad \text{Eq. 7.3}$$

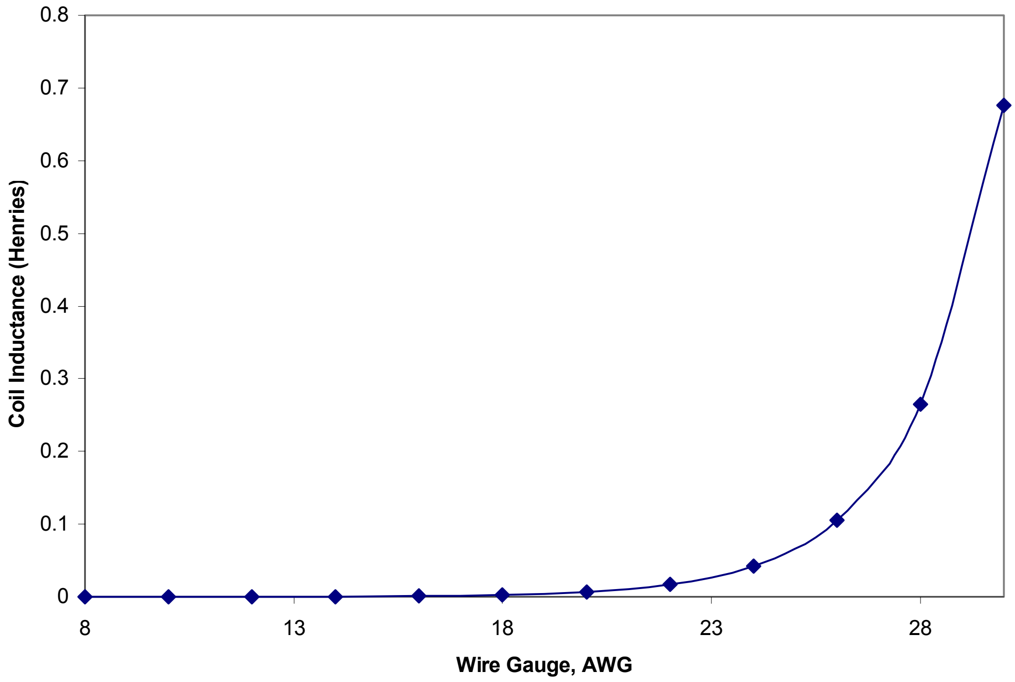

Figure 7.1 – Theoretical Coil Impedance for Various Wire Sizes, d_1=26 gauge, d_2=20 gauge

This function is plotted in Figure 7.2 for an operating frequency of 1000 Hz. Eq. 7.3 shows that the impedance of the coil is inversely related to the 4th power of the wire diameter. This relation is the explanation for the increase in required voltage with wire diameter. The current required by a coil to generate a given mmf is inversely proportional to the number of turns in the coil and is therefore proportional to the square of the wire diameter,

$$mmf = const = N_{tot} i_w \Rightarrow i_w \propto \frac{1}{N_{tot}} \propto d_w^2 \qquad \text{Eq. 7.4}$$

Since voltage required is the product of the current and impedance, from Eq. 7.3 and 7.4, the voltage required would be inversely proportional to the square of the wire diameter.

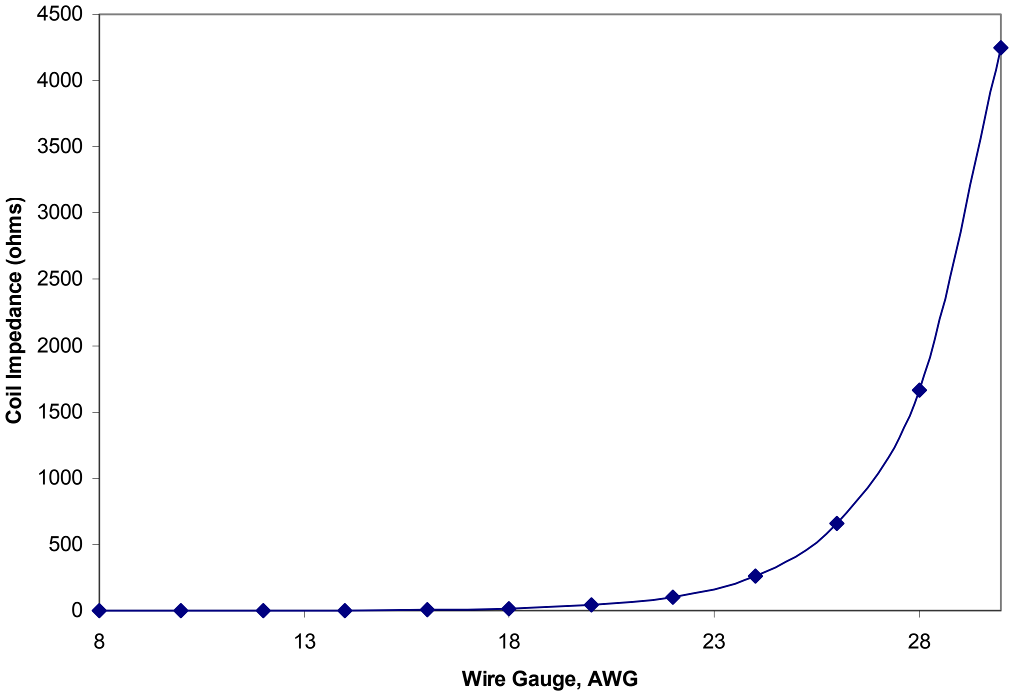

Figure 7.2 - Coil Impedance Vs. Wire Gauge

The power dissipated in the coil, however, is the product of the current squared and the resistance of the coil. Since the resistance of the coil is inversely proportional to the 4th power of the wire diameter, and the current is proportional to the wire diameter squared, it shows that the power dissipated for a given mmf and frequency would not vary with wire diameter.

$$P = i_w^2 R_w; \quad i_w \propto d_w^2,\ R_w \propto \frac{1}{d_w^4} \qquad \text{Eq. 7.5}$$

It can be seen from this analysis that the voltage requirement for the initial 26 gauge coil prohibited actuation at higher frequencies.

A new coil was designed with the primary design driver being low impedance. The wire for the new coil is then chosen as 20 AWG wire, to ensure voltage requirements are well within the amplifier's limitations of 200 V. According to the coil design algorithm, this should result in a coil with about 730 turns, a resistance of about 1.217 ohms, and a mass of about 169 g. Actual properties of the 20 gauge coil are 600 turns, a resistance of about 1.2 ohms, and a mass of about 113 g. It is not surprising that the actual number of turns is lower than the calculated number, as the design algorithm assumes a perfectly wound coil. With a larger diameter wire, it becomes more difficult to tightly wind the coil due to the increased wire stiffness. This would also explain the over-predicted mass. A picture of the 20 AWG coil is shown in Figure 7.3.

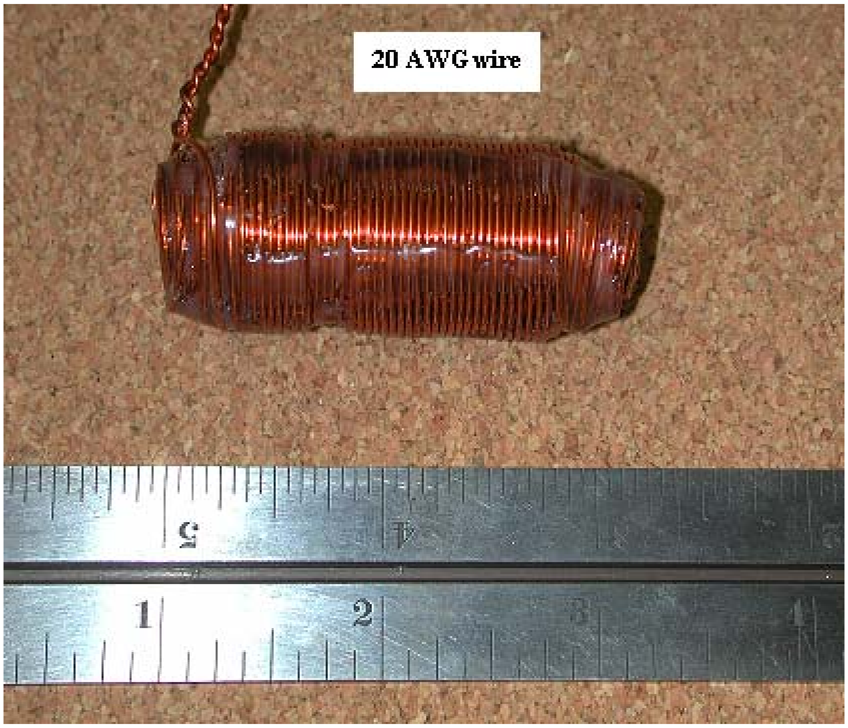

Figure 7.3 – 20 AWG Coil

7.1 Determination of Coil Inductance

Before proceeding with testing of the actuator, the inductive properties of the coil were calculated and validated experimentally. Based on Eq. 7.1, the coil inductance is calculated to be 2.1 mH. This value is obtained using a value of 3 for the magnetic permeability of Terfenol-D. A test was performed to experimentally determine the coil's inductance. With the Terfenol-D rod and flux return path, the coil was driven at a constant current of about 6 amps peak through a range of actuation frequencies (frequency of material actuation) from 0-900 Hz. The voltage drops across the coil and sense resistor were then measured. The data for this test is plotted in Figure 7.4 along with theoretical predictions. The data shows a linear relation between the voltage required and the input frequency at high frequencies. This is the expected

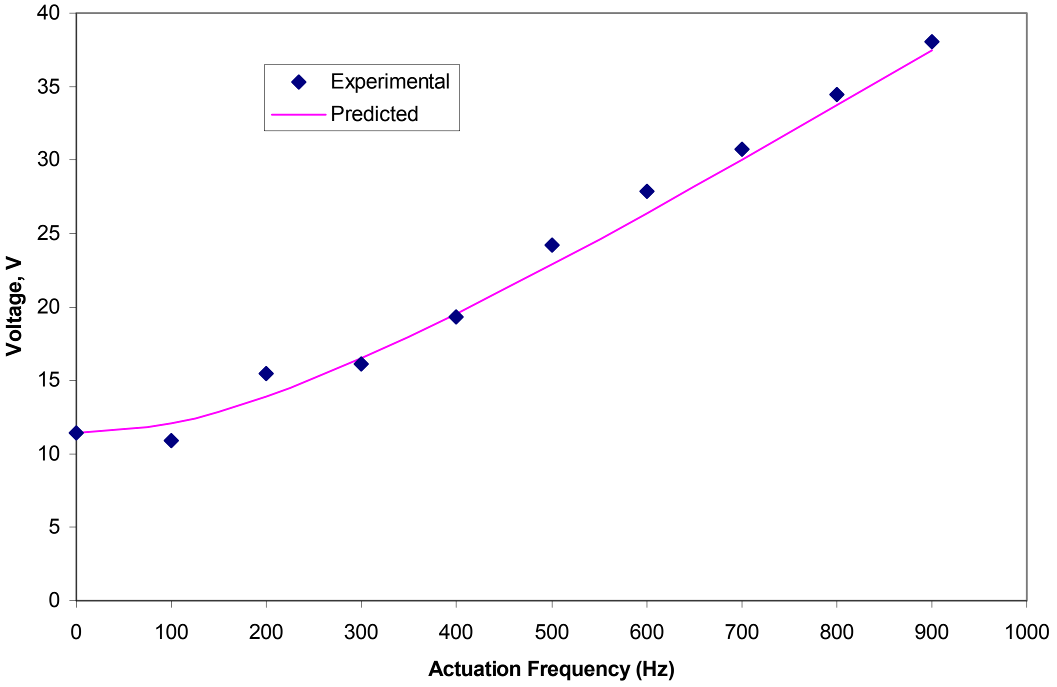

Figure 7.4 – Measured Voltage Required of 20 Gauge Coil for 6 Amps

result if the reactance, or inductive resistance, of the coil is much greater than the DC resistance. In this case, the DC resistance of the coil can be neglected when calculating the coil impedance at high frequencies, and the formula for required voltage becomes,

$$V = i_w Z = i_w \sqrt{\cancel{R_w^2} + w^2 L^2} \cong i_w w L \qquad \text{Eq. 7.6}$$

With the values of voltage and DC resistance of the coil known, the inductance of the coil can easily be determined for each frequency. These values are plotted in Figure 7.5. The experimental values show good correlation with the calculated values, especially at higher frequencies, where the inductive effects would be dominant. This

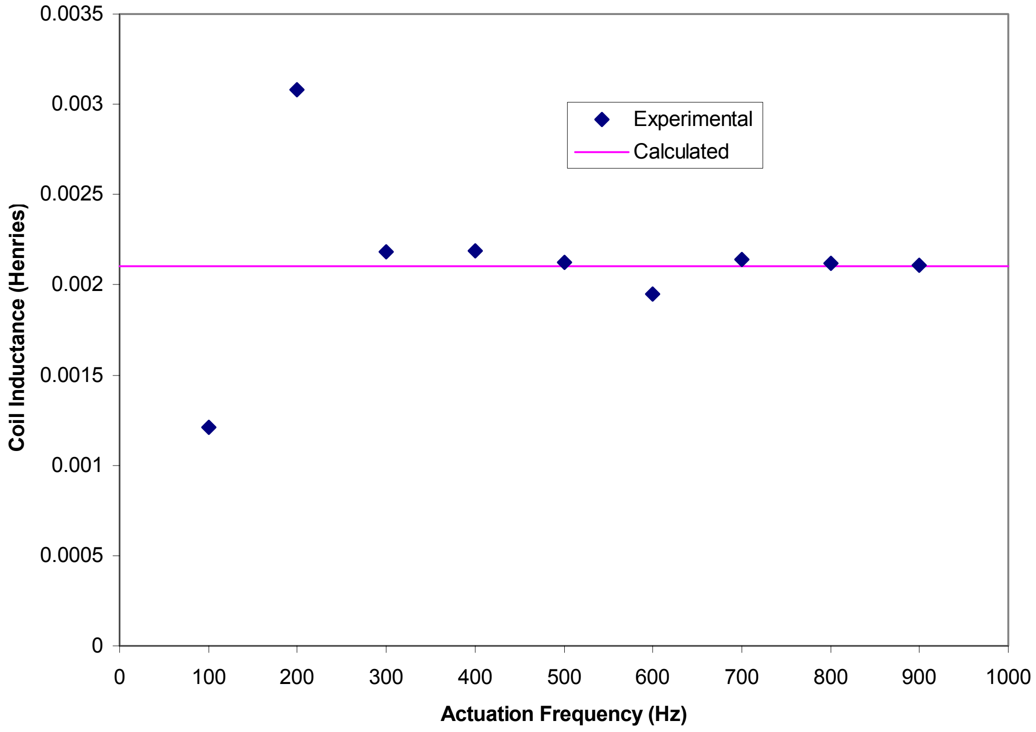

Figure 7.5 - Measured Coil Inductance of 20 Gauge Coil with Terfenol-D at 6 Amps

means that Eq. 7.6 can be used as a basis for design. In order to match the mmf generated by the initial coil, the new coil would have to be driven with about 3 times as much current, as it has 3 times fewer coil turns. For the maximum mmf generated by the initial coil, 8000 amp-turns, this coil will require about 12 amps of driving current. Before actuating at this current, the voltage required at this condition should be calculated to ensure the amplifier does not exceed its voltage limitation of 200 Volts. The predicted required voltage is plotted in Figure 7.6 for the 20 gauge coil and the 26 gauge coil. The predicted voltage of the 20 gauge coil shows maximum levels well within the amplifier limitations.

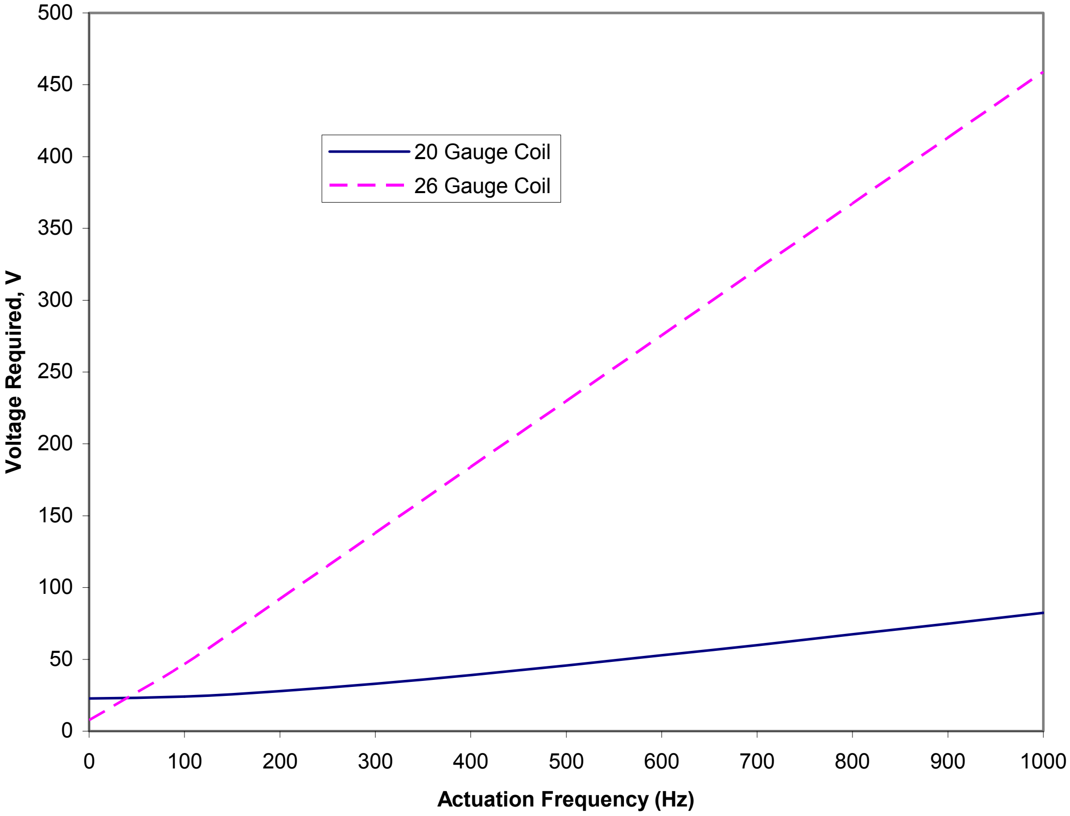

Figure 7.6 - Predicted Voltage Required for MMF = 8000 A-turns

It can also be seen from the coil analysis that the permeability of the core material has a large affect on the inductance of the coil. For example, using a coil with a Galfenol core in place of the Terfenol-D core would increase the inductance of the coil by 100 times.

$$L = \frac{\mu N_{tot}^2 A}{l_c} \qquad \text{Eq. 7.7}$$

This is because the permeability of Galfenol is about 100 times the permeability of Terfenol-D ($\mu_{Gal} \cong 100\mu_{Terf}$). However, because of the high permeability of Galfenol, only about 24 kA/m^2 of field is required to induce maximum strain in the material. This is approximately 30% of the required field for Terfenol-D ($H_{Gal} = 24kA/m^2 \cong 0.3H_{Terf}$). Based on Eq. 7.8 for mmf, this means that the required current for maximum strain of Galfenol is about 60% of the required current for Terfenol-D.

$$N_{tot} i_{Gal} = 2H_{Gal} l_s \cong 2(0.3H_{Terf}) l_s \Rightarrow i_{Gal} \cong 0.6\frac{H_{Terf} l_s}{N_{tot}} \qquad \text{Eq. 7.8}$$

And since,

$$i_{Terf} = \frac{1.05 H_{Terf} l_s}{N_{tot}} \qquad \text{Eq. 7.9}$$

Then,

$$i_{Gal} \cong 0.6 i_{Terf} \qquad \text{Eq. 7.10}$$

Note that the subscripts for current and magnetic field refer to values required for maximum strain of that material. Because the coil will be 100 times more inductive with a Galfenol core, it will also have about 100 times greater impedance. The combination of the lower current required and higher reactance will result in the required voltage being about 60 times the required amount for Terfenol-D at a frequency ω.

$$V_{Gal} = i_{Gal}\omega L_{Gal} \cong (0.6 i_{Terf})\omega(100 L_{Terf}) = 60 i_{Terf}\omega L_{Terf} = 60 V_{Terf} \qquad \text{Eq. 7.9}$$

The power required will be about 36 times higher.

$$P_{Gal} = V_{Gal} i_{Gal} \cong (60 V_{Terf})(0.6 i_{Terf}) = 36 V_{Terf} i_{Terf} = 36 P_{Terf} \qquad \text{Eq. 7.10}$$

The analysis shows that large amounts of power and voltage are required to induce the maximum strain in Galfenol, compared to Terfenol-D. In addition, the maximum strain of Galfenol is less than one third the maximum strain of Terfenol-D. In terms of performance, a Galfenol actuator does not compare to an equally sized Terfenol-D actuator. Its only advantage in this type of application is its robust qualities and machinability, as well as low cost. Therefore, in order to design an efficient hybrid actuator using Galfenol as the driving material, a novel approach must be taken in order to utilize these qualities. Compared strictly on output strain and input power, there is no reason to use Galfenol in place of Terfenol-D.

7.2 Improvements in the Design of the Pump Body

A possible source for the high amounts of heat generated by the first coil is the presence of eddy currents in the pump body. Due to the alternating magnetic induction in the actuator, eddy currents are set up in the pump body in such a way that they produce a magnetic field opposing the one produced by the coil. This leads to power losses through ohmic heating of the pump body, and therefore, increases the required power for a given mmf. The use of laminated active material helps to minimize this effect, but does not eliminate it. In order to further reduce the presence of eddy currents, 2 slots were cut lengthwise into the pump body. A picture of the slots can be seen in Figure 7.7. The slots are 1/32" wide, cut lengthwise to maintain the stiffness of the pump body. The slots divide the area of the pump body into two, limiting any circulating current. Because the slots are cut lengthwise, the change in reluctance along the path of the magnetic field is minimal, and does not affect the magnetic induction of the Terfenol-D rod. The result should be a lower required current for the same mmf, and therefore a lower generated heat.

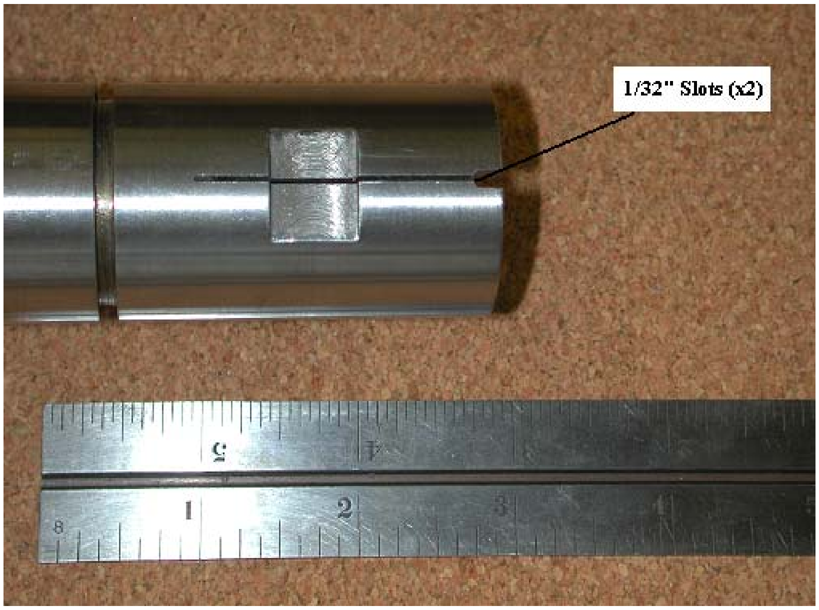

Figure 7.7 - Slots Cut in Pump Body

7.3 Strain Characterization

The new Terfenol-D actuator is limited by a maximum drive current of 12.5 amps. This limitation is due to the current limit of the amplifier. The strain of the Terfenol-

D rod is plotted against the input current of the coil in Figure 7.8 at an actuation frequency of 100 Hz. In this condition, the strain amplitude of the Terfenol-D rod is about 900 $\mu\varepsilon$ and is beginning to reach a state of saturation. The actuator strain shows a significant amount of hysteresis. This hysteresis is a result of a remnant magnetic field in the pump body. The remnant field results in a negative field being required to bring the strain of the material back to zero. This results in a decrease in maximum applied field and maximum induced strain. The value of maximum strain

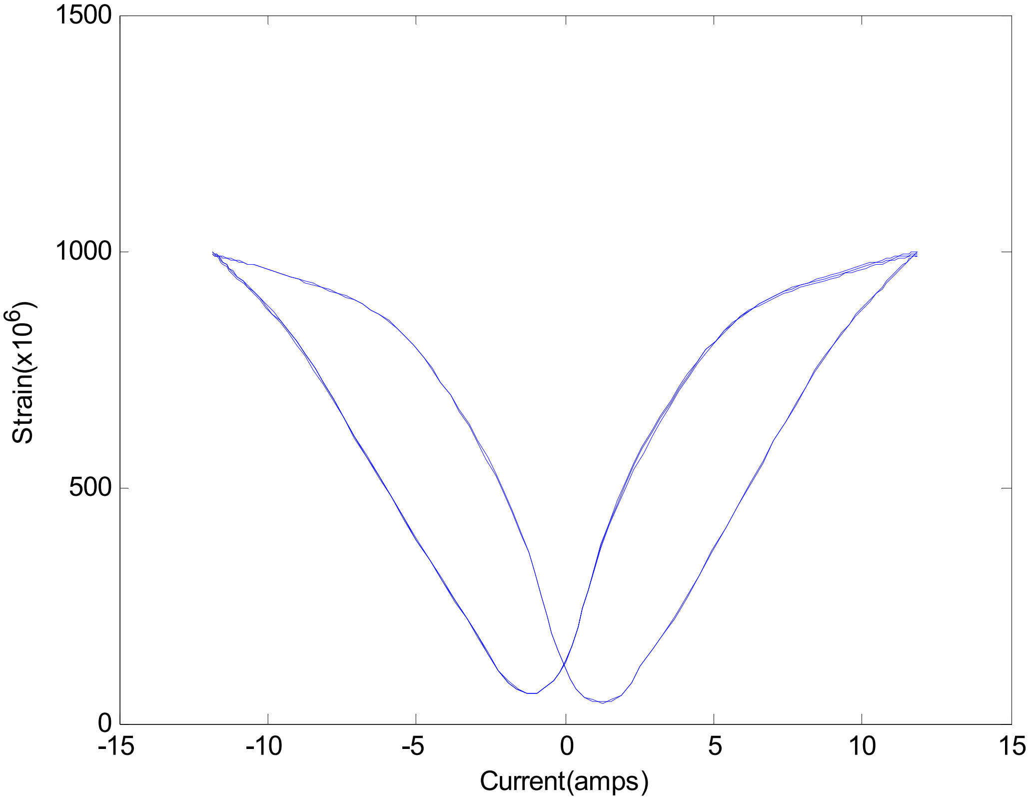

Figure 7.8 - Measured Strain of Terfenol-D Actuator in 20 Gauge Coil at 100 Hz, No-load

for a given current input, or applied field, decreases slightly at increasing actuation frequencies. A plot in Figure 7.9 shows the strain as a function of actuation frequency for a constant input current amplitude of about 12 amps. With the 20 gauge coil, the Terfenol-D rod can be actuated up to a frequency of about 800 Hz at the same level of mmf as the 26 gauge coil. This is almost twice the actuation frequency that was obtained with the 26 gauge coil. The variation of strain at low frequencies is minimal and becomes noticeable after about 500 Hz. At 800 Hz, the strain is only about 86% of its value at 100 Hz. This is probably due to the effect of operating near the resonant frequency of the hydraulic circuit. The amplifier used to supply power to the coil is within its power limitations at this condition and is not the cause of the decreased strain.

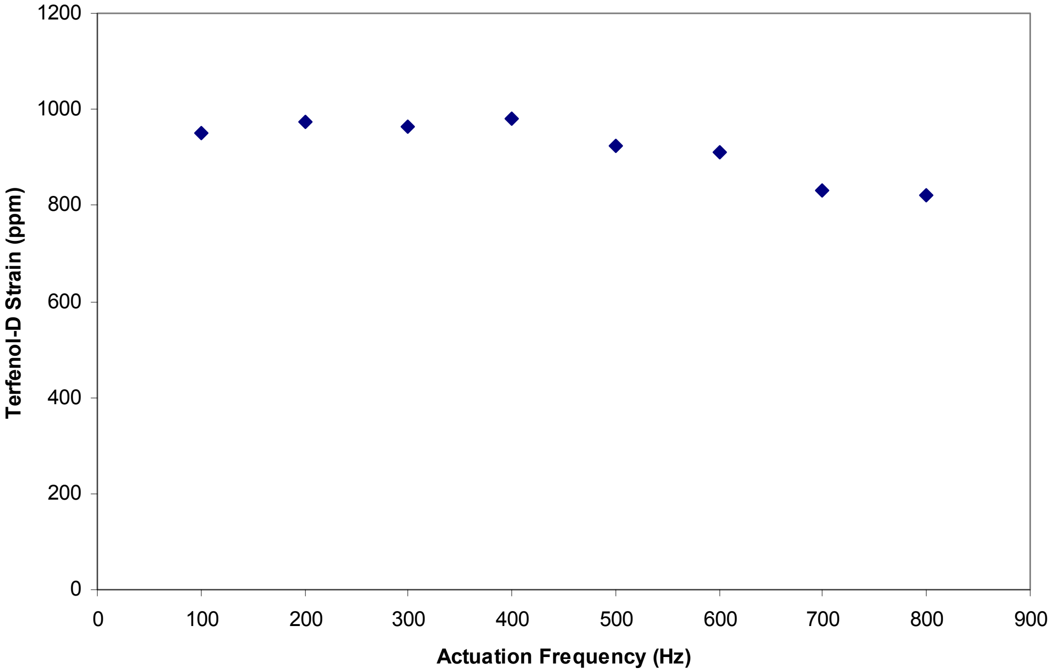

Figure 7.9 – Measured Strain Variation of Terfenol-D in 20 Gauge Coil, Unloaded

The improvements made to the pump body and field generating coil should result in an increase in performance over the previous actuator. Because the new coil was wound with larger diameter wire and fewer turns, it carried a lower inductance than the initial coil, therefore requiring less voltage at high frequencies. This coil characteristic allows actuation of the Terfenol-D rod at higher frequencies when operated at its maximum induced strain. In addition, slots cut in the pump body help to reduce eddy current losses, and in doing so, lower the required current for a given induced strain. This should lower power requirements and generate less heat at all operating conditions. Important parameters of the 20 gauge coil are listed in Table 7.1.

20 Gauge Coil Parameters	
Physical Dimensions	
Number of Turns	600
Wire Diameter	0.00081"
Coil Length	2"
Coil Diameter	0.9"
Total Mass	113 g
Electrical Properties	
DC Resistance	1.2 ohms
Inductance	2.1 mH

Table 7.1 - Coil Parameters

Chapter 8: Piezostack Actuator Characterization

In order to compare the Piezo-pump performance to the performance of the magnetostrictive actuator, a piezostack was constructed with an active length equal to the active length of the Terfenol-D rod. The equivalent active lengths provided a basis for comparison. The length of the new stack was 2.05", with a cross-sectional area of 0.155 in and a mass of 60 grams. A picture of the new piezostack instrumented with full-bridge strain gauges is shown in Figure 8.1. The three stacks were connected in parallel, resulting in a total capacitance of 21 μF. The reactance of the piezostacks, X_C, is given by the equation,

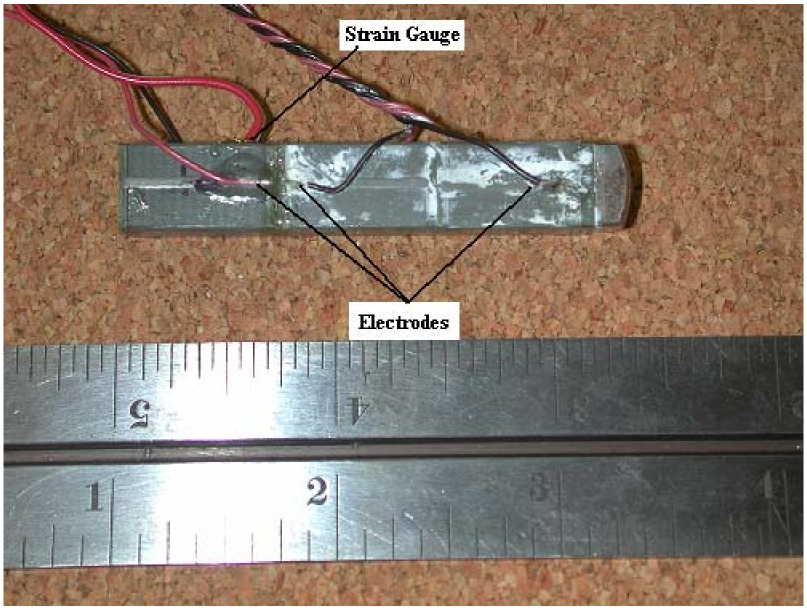

Figure 8.1 - Piezostack Actuator, 3 PI 804.1 Stacks in Series [62]

$$X_C = \frac{1}{2\pi f C} \qquad \text{Eq. 8.1}$$

where f is the frequency of excitation. The maximum operating voltage range of the piezostack recommended by the manufacturer is 0-100 volts. Because the reactance of a capacitor decreases with increased frequency, maintaining a voltage level of 0-100 volts at high actuation frequencies requires increased current. A plot of the current required as a function of actuation frequency is shown in Figure 8.2 along with experimental results. The plot shows that at high frequencies, the required current begins to level off. Since this is a non-ideal capacitor, its resistance is not purely reactive. Internal friction of the piezostack molecules will cause an energy loss during actuation. This effect can be modeled as a DC resistor. The impedance of the piezostack is a combination of the reactance and this resistive component. At higher frequencies, the reactance of the piezostacks becomes small and the impedance

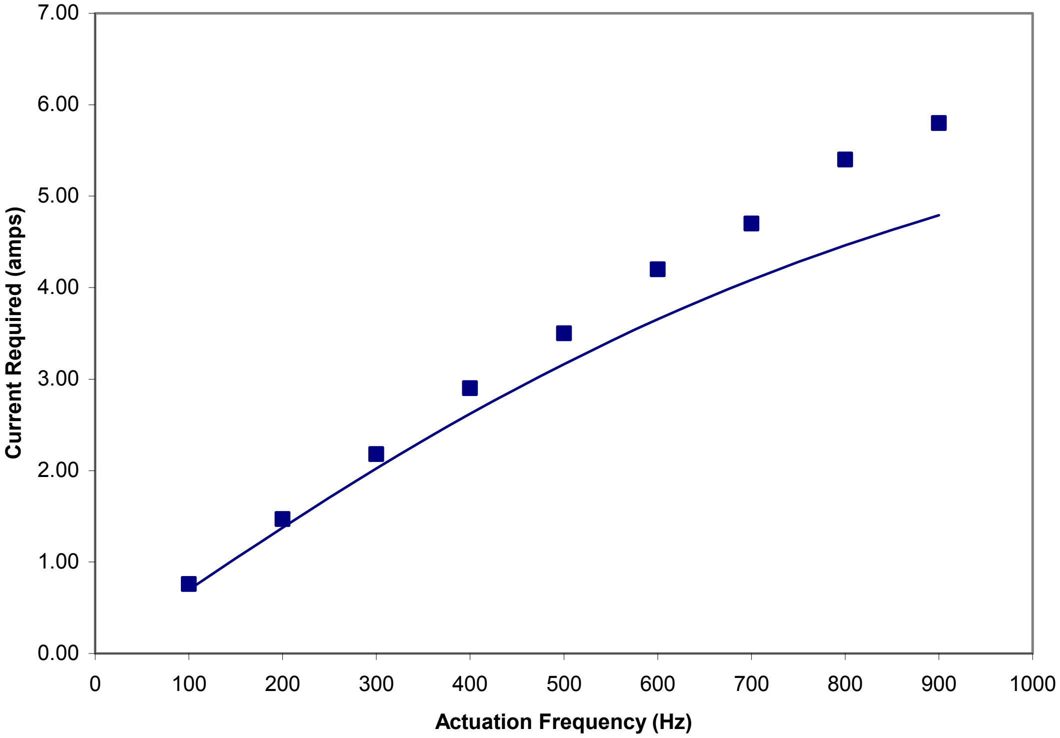

Figure 8.2 – Predicted and Measured Current Required by Piezostacks (0-100V)

becomes predominantly resistive. From measured values of required current, the DC resistance is measured at about 6.5 ohms. The variation of measured impedance with actuation frequency is shown in Figure 8.3. The measured capacitance of the piezostacks during actuation is higher than 21 μF. This is due to the variation of the piezostack capacitance with applied field. Eq. 8.2 shows the relation of capacitance to the physical characteristics of parallel plates.

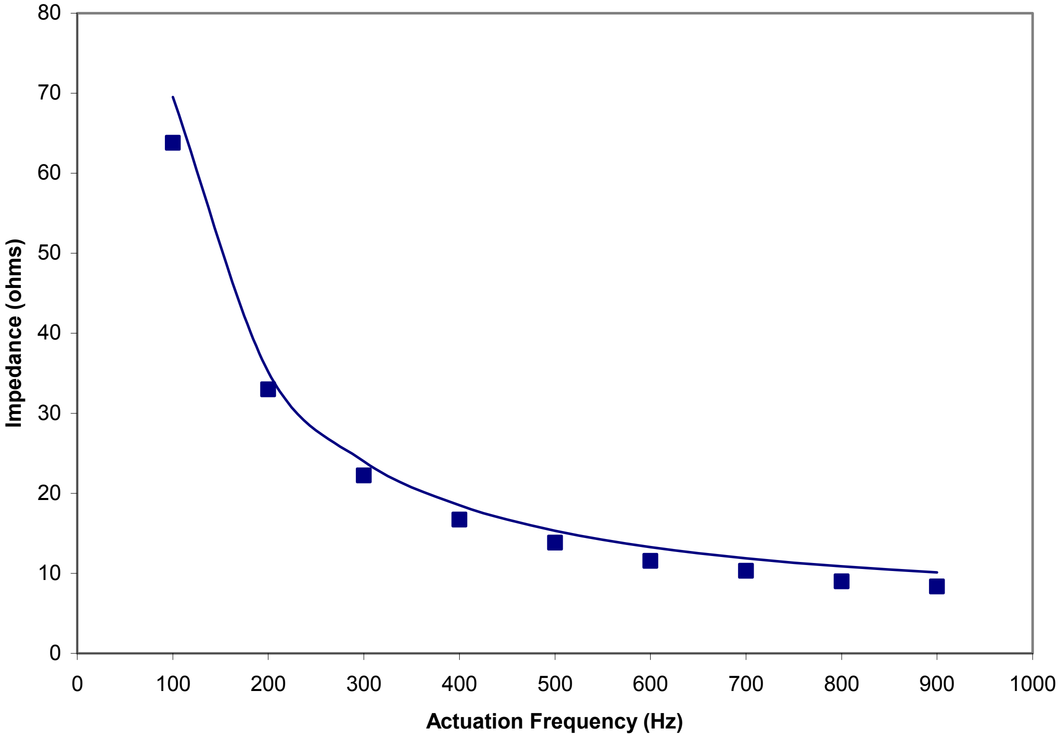

Figure 8.3 – Predicted and Measured Impedance Variation with Actuation Frequency (0-100V)

$$C = K_{\varepsilon} \frac{A}{d} 8.85 \times 10^{-12} \qquad \text{Eq. 8.2}$$

The piezostack can be treated as a number of parallel plate capacitors connected in series, where A is the area of each plate, d is the distance between each plate, and

K_ε is the dielectric constant of the material between the plates. The dielectric constant of the piezoceramic material varies with applied field, changing the capacitance during actuation.

The induced strain of the piezostack is plotted against the input voltage at a frequency of 100 Hz in Figure 8.4. The maximum strain of the piezostacks is about 700 $\mu\varepsilon$.

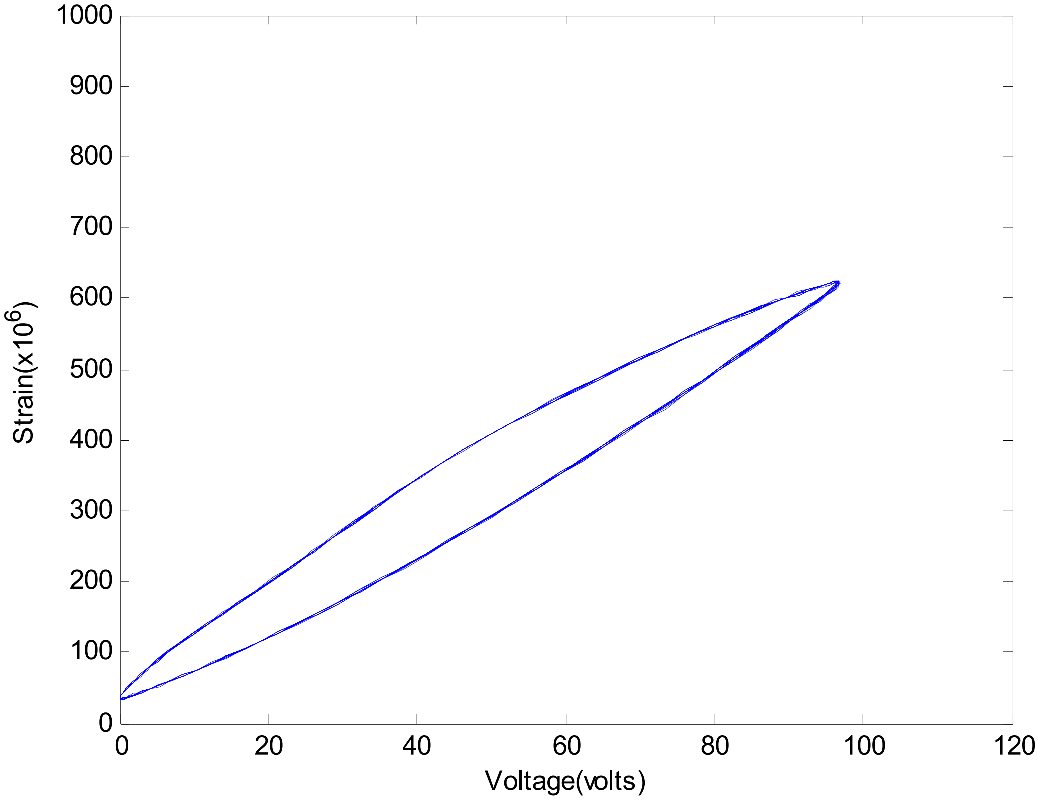

Figure 8.4 – Measured Piezostack Induced Strain at 100 Hz

The hysteresis present in the piezostack is due to the changing orientations of the unit cells of the material in response to a large electrical field or mechanical stress. This results in the movement of the unit cell domain walls and makes the overall response of the material non-linear. The hysteresis dissipates energy in the form of internal heating. Self-heating test results for piezoelectrics can be found in [44].

Similarly to the Terfenol-D rod, the piezostack strain varies somewhat with actuation frequency. This is illustrated in Figure 8.5. The effect is less apparent for the piezostacks, but the induced strain clearly decreases at higher frequencies near the resonant frequency of the hybrid actuator.

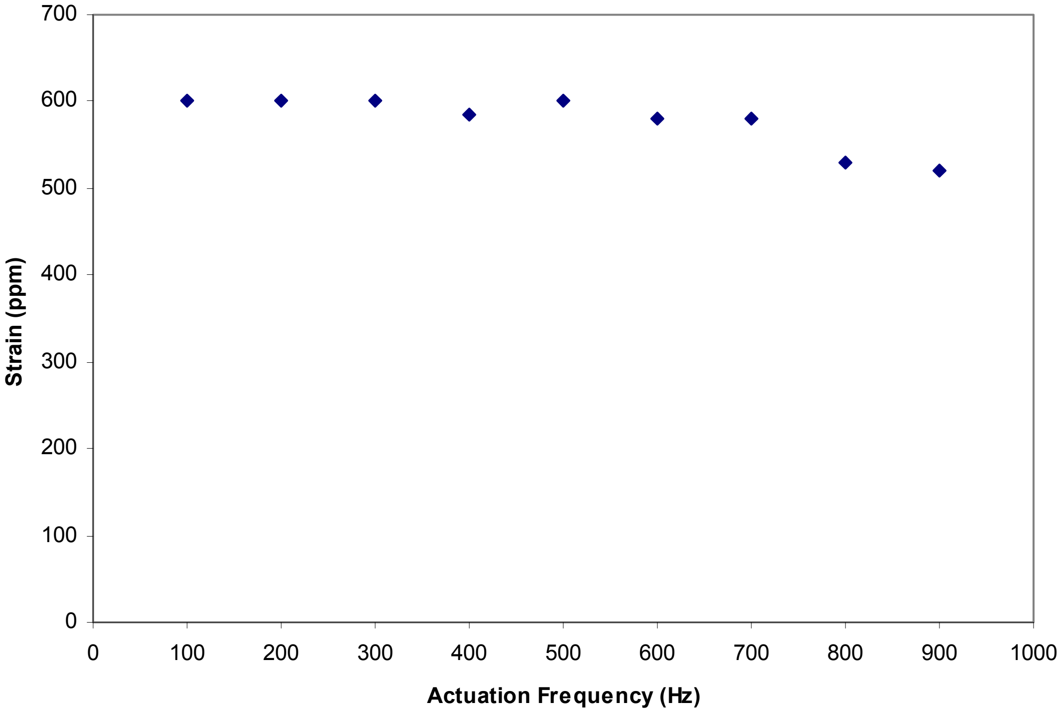

Figure 8.5 – Measured Variation of Piezostack Strain with Actuation Frequency (0-100V)

The important dimensions of the piezostack driving element are listed in Table 8.1. Having characterized the basic properties of the new piezostack, the actuator performance can now be tested and compared with the performance of the magnetostrictive actuator. Because all performance comparisons will be made based on input power, actuating the materials at different values of induced strain will not affect the comparisons. The efficiencies of each actuator can be measured separately and compared.

Piezostack (P-804.10) Dimensions	
Number of stacks	3
Cross-sectional area	0.152 sq. in.
Stack length	0.7"
Blocked force (0-100V)	1133 lbs.
Free strain (0-100V)	700 ppm
Free displacement (0-100V)	1.47 mil
Total Capacitance	21 μF
Total Mass	60 g

Table 8.1 - Piezostack Dimensions [62]

Chapter 9: Comparison of Results

9.1 No-Load Performance

The unloaded velocity of the piezo-pump and magnetostrictive-pump actuator was measured in order to determine the fluid flow rate produced by each actuator across a range of actuation frequencies. The maximum actuation frequency was limited by amplifier capability. Each active material was run at its maximum strain condition to determine its maximum fluid flow rate as well as the response of the hydraulic circuit. Each test consisted of measuring the velocity of the output cylinder as well as the strain of the active material at a constant excitation frequency. In addition, the voltage and current input to the actuator was monitored so that the input power could be obtained at each condition. In this way, the performance of each active material could be compared based on the input power.

The no-load velocities of both pumps are plotted against actuation frequency in Figure 9.1. A prediction based on a simple quasi-static modeling of the pump is also plotted for both cases. The strain of the material at each actuation frequency and the dimensions of the pumping chamber were used to calculate the fluid flow produced by the material. The dimensions of the output cylinder were then used to predict the output velocity. The experimental data agrees well with predicted values at low actuation frequencies. As the actuation frequency approaches resonance, dynamic effects in the hydraulic circuit become apparent. State of the art modeling techniques can not yet accurately capture the actuator behavior at high frequencies. The plot shows that the resonant frequency of the Terfenol-D pump is about 150 Hz less than the resonant frequency of the piezostack pump. A possible explanation of this trend is the difference in stiffness of the two driving materials. The Terfenol-D rod has a lower stiffness than the piezostack leading to a lower resonant frequency.

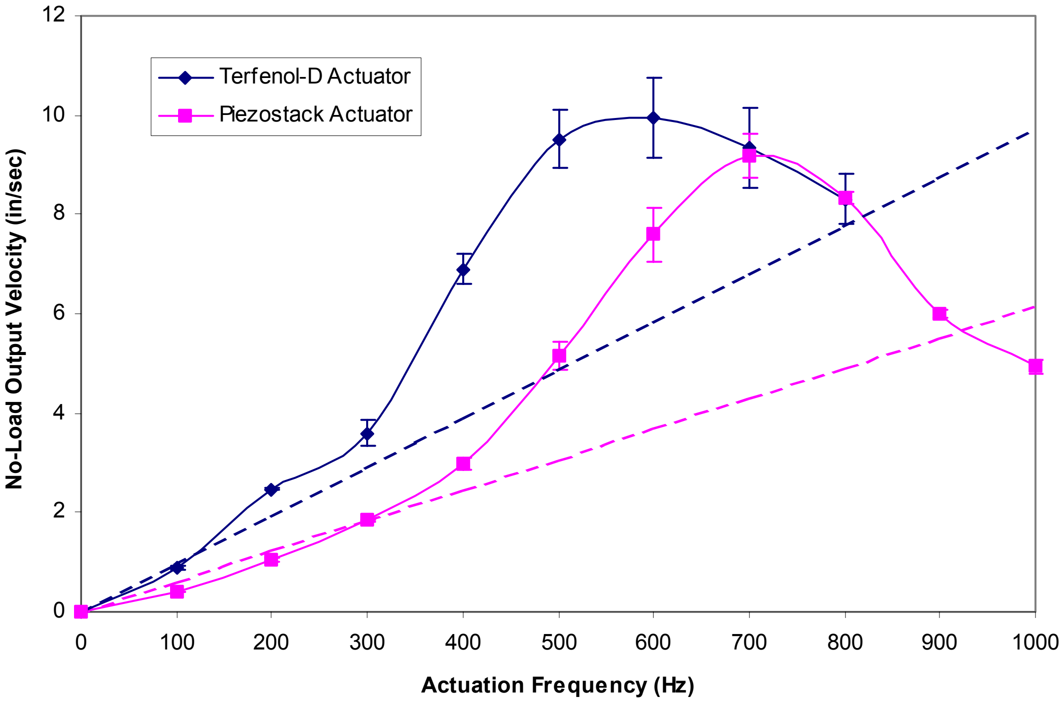

Figure 9.1 - No-Load Cylinder Velocity and Quasi-Static Predictions

The output velocity of the Terfenol-D actuator is higher than the piezostack actuator due to the higher maximum strain. Note that this may not be a fair comparison because the Terfenol-D actuator requires more input power to drive the material to achieve its maximum induced strain. By normalizing these output velocities by the input power required at each frequency, a better comparison can be made between the two actuators. Since no-load velocities are being measured, the output velocity corresponds to the losses in the actuator. The losses can be assumed equal for the cases of the piezostack actuator and the Terfenol-D actuator, since the output velocities of both are on the same order. Figure 9.2 shows the output velocity normalized with the input power for each actuator across a range of actuation frequencies. The input power used to calculate these values is the apparent power or total power required. The total power is the product of voltage and current that are out of phase because of reactance. The actuators are close in performance at low values of actuation frequency, up to 400 Hz. As the actuators approach higher frequencies, the coil inductance drives up the input power of the magnetostrictive coil, resulting in a significant degradation in its performance. The maximum efficiency of the piezostack actuator nearly doubles that of the Terfenol-D actuator.

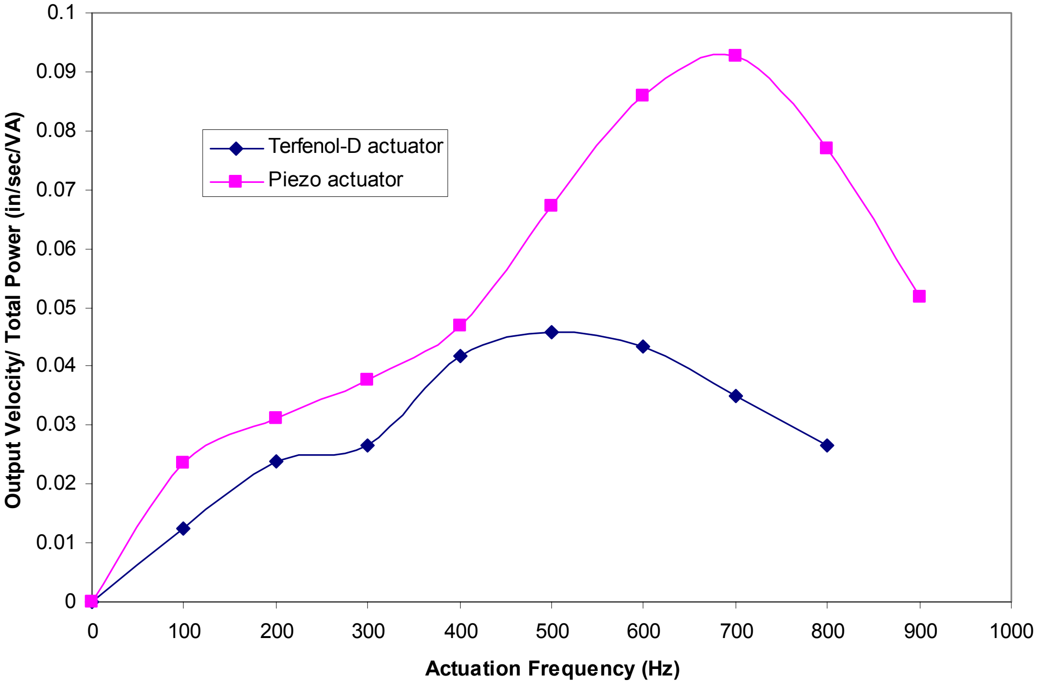

Figure 9.2 – Measured No-Load Output / Input Power

It is important to know whether the actuators would retain the same level of efficiency if driven at a different input excitation level. In order to determine this, both actuators were driven with varying input powers at a constant actuation frequency of 400 Hz. The results are shown in Figure 9.3. The plot shows that each

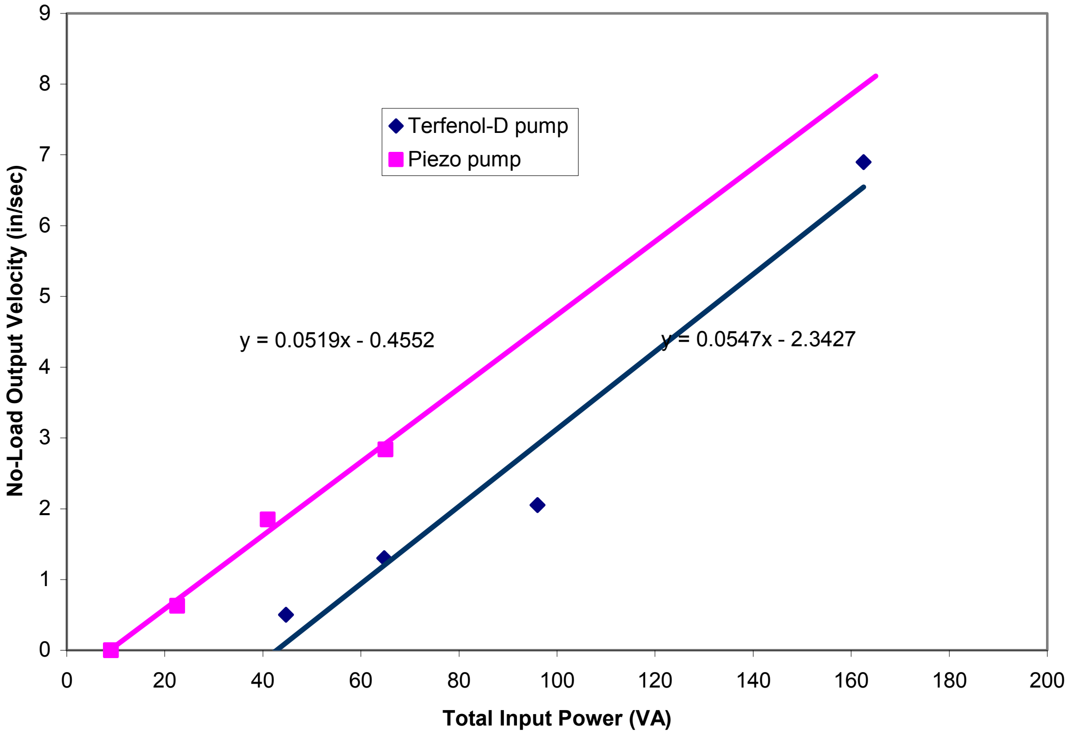

Figure 9.3 - Variation of Output Velocity with Input Power at 400 Hz

actuator output velocity has a linear relation with input power. This means that the actuators will maintain a constant efficiency, regardless of the input power. At this frequency, the slope of both curves is about the same. This means that for a given increase in input power, both actuators will give the same increase in output velocity. As the actuation frequency increases, the efficiency of the Terfenol-D actuator will decrease as the inductive reactance of the coil becomes large and requires more input power. The piezostack actuator efficiency continues to increase with frequency as the output gains from operating near resonance have a greater effect than the losses suffered from the decreased capacitive reactance. This trend can be explained by looking at the required input power as a function of actuation frequency. These values are plotted in Figure 9.4 for both actuators. The relation of input power to actuation frequency is almost linear for both actuators. The slope of the Terfenol-D actuator curve is much higher than the piezostack actuator curve, meaning more power is required for the same increase in actuation frequency. This trend is responsible for the loss of efficiency in the Terfenol-D actuator as the actuation frequency increases to resonance.

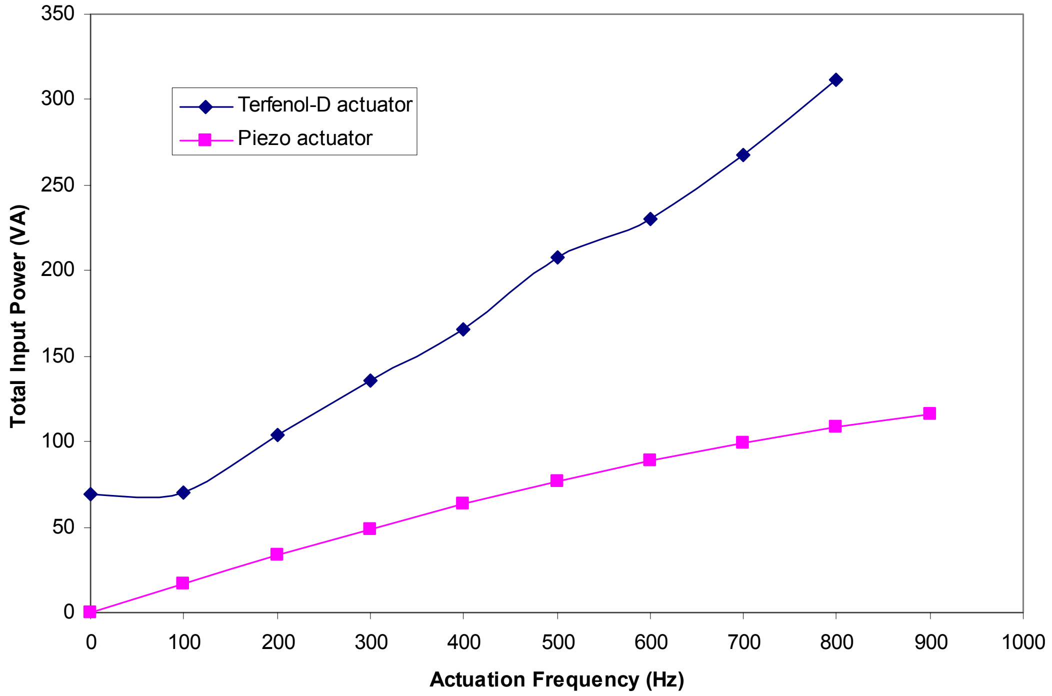

Figure 9.4 – Measured Required Power for Actuation at Maximum Strain Condition

9.2 Loaded Performance

After testing unloaded performance, tests were performed to measure the blocked force and overall loaded performance of the actuators. By measuring the loaded velocity of the actuators with a known output load, a value of output power could be obtained. Based on the input power required at each operating condition, an efficiency can be found. To do this, a value of output power was measured across a range of actuation frequencies. At each frequency, the active material was driven with a constant value of voltage or current, for the piezostack and Terfenol-D, respectively. Output velocities were measured for several loads acting on the actuator, leading to a force-velocity curve at each frequency. These force-velocity curves are plotted in Figure 9.5 and Figure 9.6 for the piezostack actuator and the Terfenol-D actuator, respectively.

These plots show only the curves for actuation frequencies of 100 Hz, 200 Hz, and 300 Hz. A linear fit is plotted for the data points in order to extrapolate the blocked force of the actuator. The unloaded velocities of the actuators are almost linear with actuation frequency. This is to be expected since fluid flow rate is simply a product of the piston deflection and the actuation frequency at low frequencies below resonance (See Figure 9.2). As the output load is increased, the strain of the actuating material decreases and the output velocity at all frequencies converges to zero at the blocked force condition. The blocked force remains constant for all actuation frequencies. The blocked force of the Terfenol-D actuator is about 10 lbs, while the

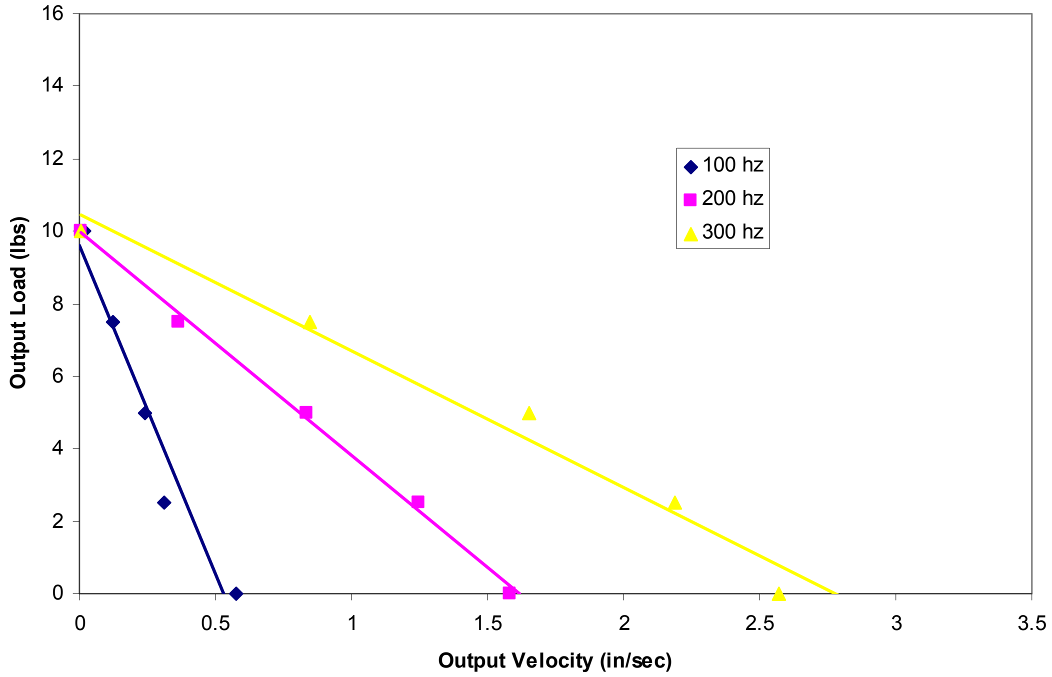

Figure 9.5 – Measured Force-Velocity Curve of Terfenol-D Actuator

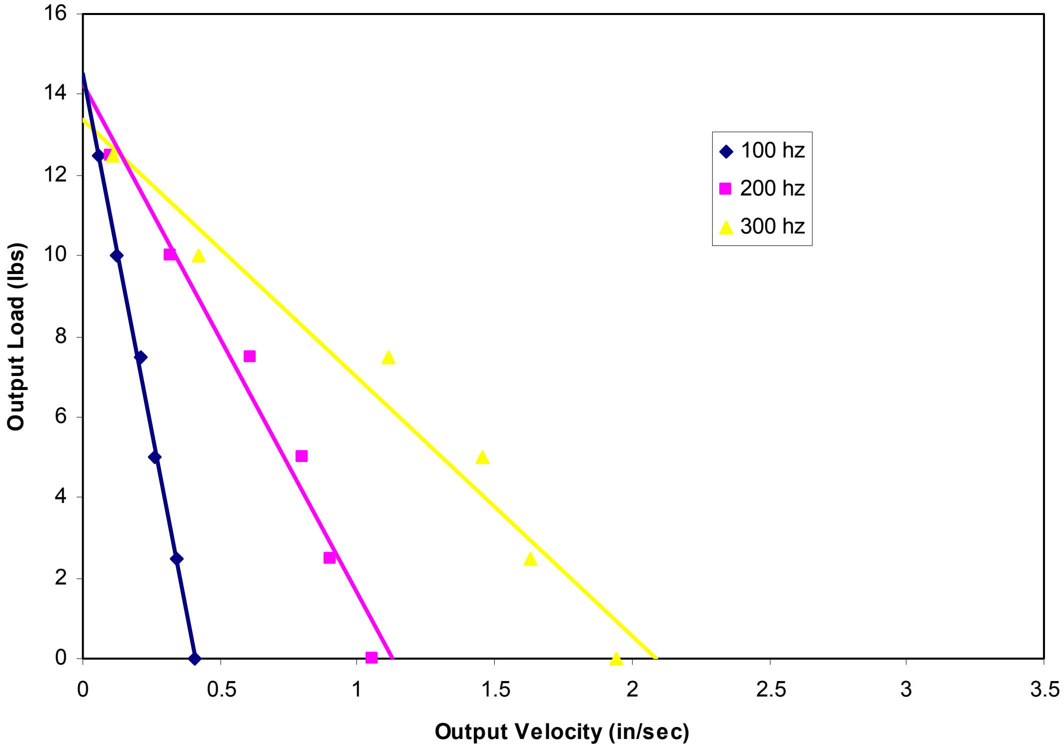

Figure 9.6 – Measured Force-Velocity Curve of Piezostack Actuator

blocked force of the piezostack actuator is about 14 lbs. The difference of about 40% is due to the lower stiffness of the Terfenol- D rod. Because of this, there is a greater decrease in strain for a given output load. This effect can be seen in Figure 9.7, where the induced strain amplitude of each actuator is plotted against output load at an actuation frequency of 100 Hz.

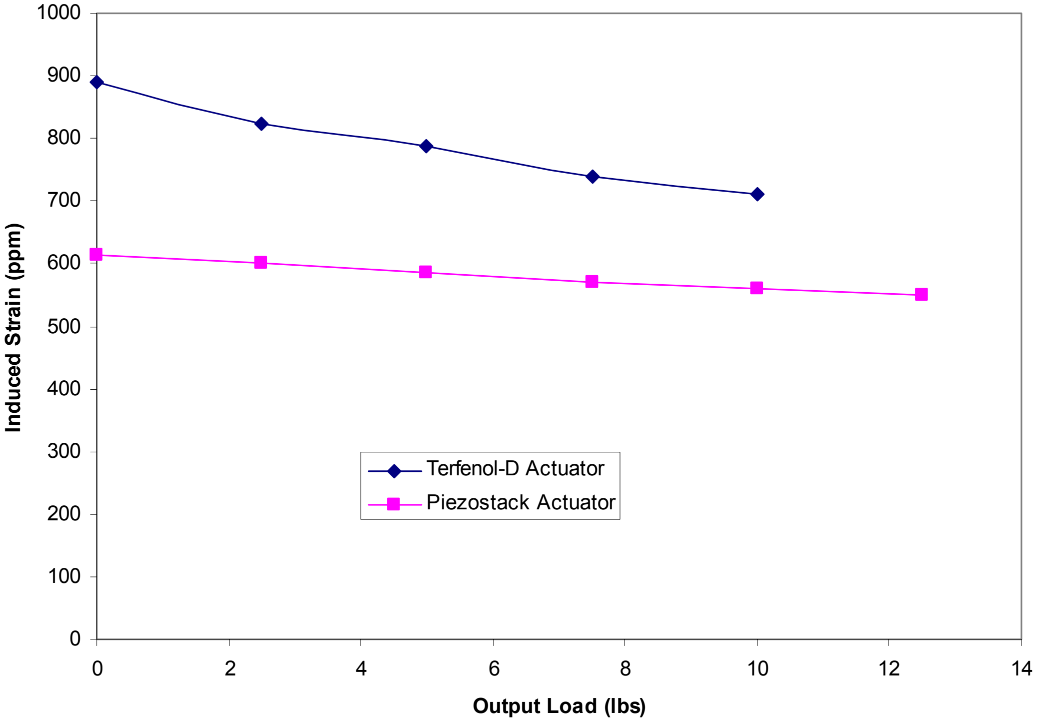

Figure 9.7 – Induced Strain Under External Load

To obtain a value for output power of the actuator, the area under the force-velocity curve was found for each actuation frequency. This area corresponds to the available power of the actuator. Half of the area under the force-velocity curve corresponds to the maximum output power condition and was calculated at each actuation frequency. The values of maximum output power are plotted against actuation frequency for both pumps in Figure 9.8. The plot shows similar values of output power at low actuation frequencies. This is because, although the Terfenol-D pump has a lower blocked force than the piezo pump, it also has a greater no-load velocity. The two factors balance out at low frequencies. At higher frequencies, the blocked forces remain constant, but the un-loaded velocities increase, resulting in a higher output power for the Terfenol-D pump.

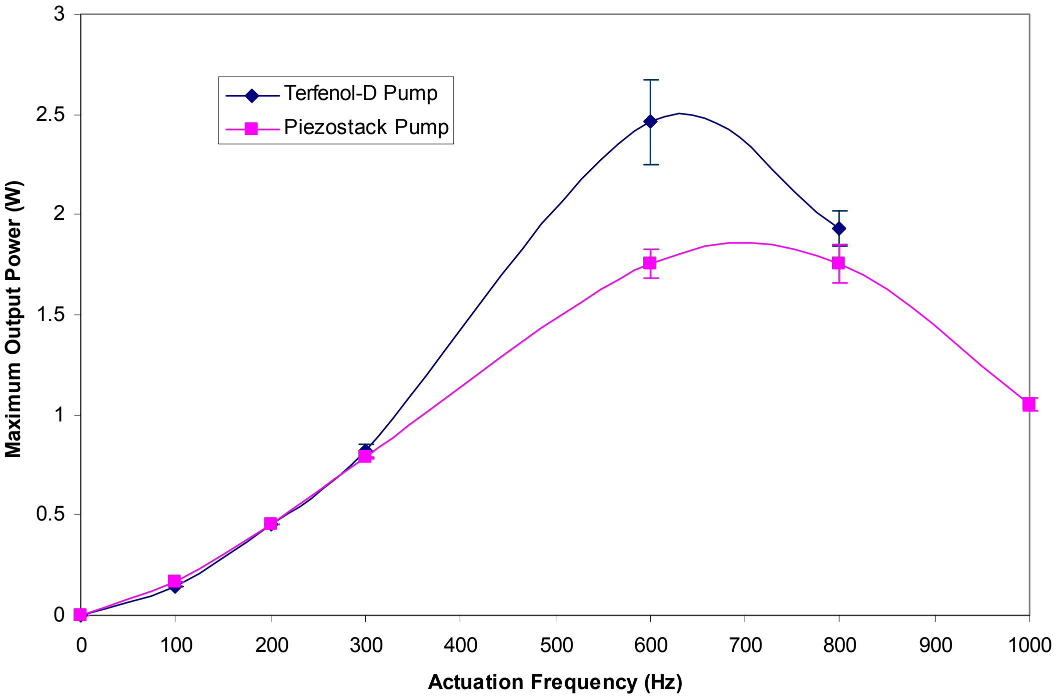

Figure 9.8 – Maximum Output Power

An accurate comparison of the actuator efficiencies cannot be made without considering the input power. By normalizing the output power of the actuators by the input power at each frequency, the overall efficiency can be obtained. The efficiency of each actuator, based on apparent input power is shown for varying actuation frequencies in Figure 9.9. It can be seen that the efficiency of the piezostack actuator is about twice the efficiency of the Terfenol-D actuator across all actuation frequencies. At low frequencies, when the output power of both actuators is about the same, the larger input power drives down the efficiency of the Terfenol-D actuator. As the actuation frequency increases, the Terfenol-D actuator produces more output power than the piezostack actuator. However, the large increase in required input power from the inductive reactance of the coil degrades the overall efficiency. Because of the lower power requirements of the piezostack actuator, its overall efficiency is much higher than the Terfenol-D actuator. To improve the Terfenol-D actuator, a coil with slightly larger wire diameter could be used to help lower the reactance at high frequencies. A coil with a much larger wire diameter, however, will begin to lose efficiency as the winding process becomes more difficult.

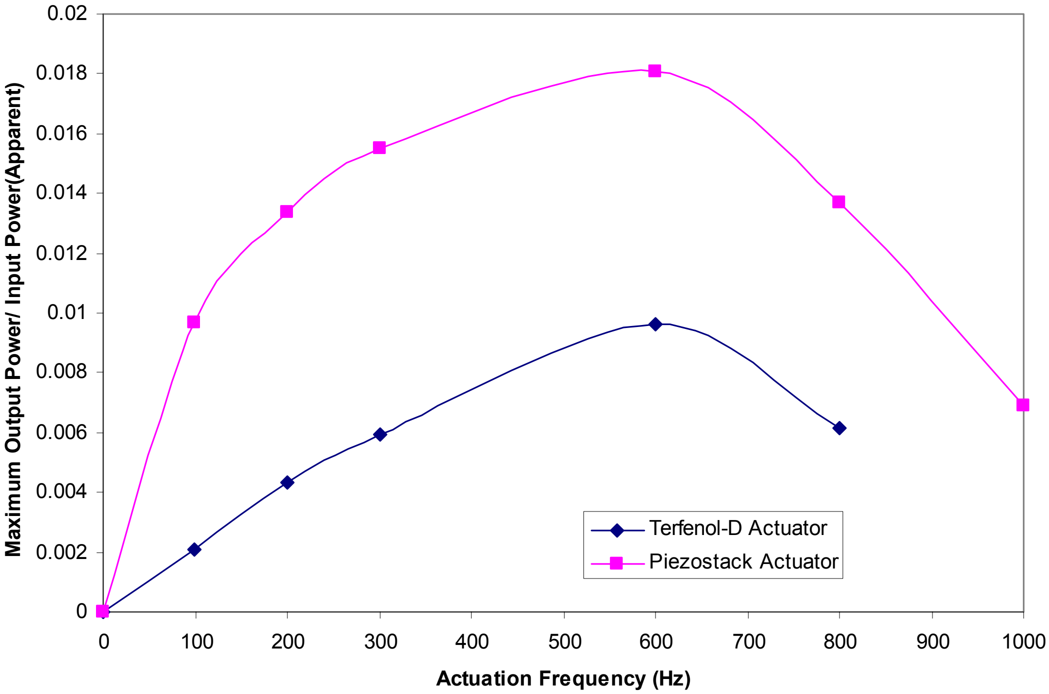

Figure 9.9 - Actuator Efficiency (Apparent)

The maximum efficiency of the Terfenol-D pump and piezostack pump are low when determined using apparent power. The reactance of the active materials dominates the impedance and creates a large reactive power requirement. The dissipated power is a measure of the ohmic losses in the actuators, and can also be used to determine actuator efficiency. The apparent power is much higher than the actual dissipated power in both of these cases. Efficiencies are calculated using dissipated power and are plotted against actuation frequency in Figure 9.10. The efficiencies of the actuators with respect to dissipated power are much higher. The power dissipated in the Terfenol-D actuator comes from the DC resistance of the coil, and remains constant with actuation frequency. The power dissipated in the piezostack actuator comes from molecular friction and increases with actuation frequency. At low frequencies, the piezostack dissipates very little power because of the low current input. The dissipated power varies with the square of the input current. The efficiency of the piezostack actuator with respect to dissipated power is, therefore,

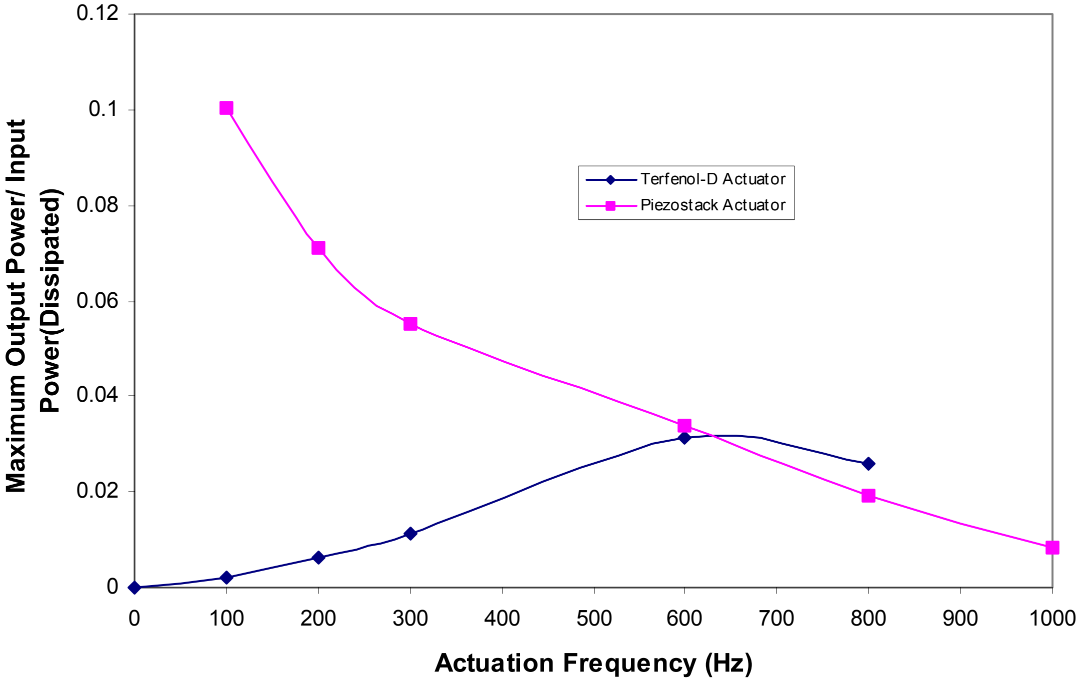

Figure 9.10 – Actuator Efficiency (Dissipated)

very high at low frequencies. A comparison of important actuator performance measures is given in Table 9.1.

Performance Comparison		
	Terfenol-D	**Piezostack**
Mass of Active Material	14.8 g	60 g
Mass of Coil	113 g	N/A
Maximum No-Load Velocity	10 in/sec (@600 Hz)	9.25 in/sec (@700 Hz)
Blocked Force	10 lbs	14 lbs
Maximum Output Power	2.5 W (@600 Hz)	1.75 W (@600 Hz)
Maximum Efficiency	1% (@600 Hz)	1.8% (@600 Hz)
Dissipated Power at Maximum Efficiency	78.14 W	52.02 W

Table 1 – Performance Comparison of Terfenol-D and Piezostack Actuators

9.3 Reactance Canceling

A method to reduce the apparent input power required for either actuator is to cancel the reactance of the actuator with a series or parallel reactance. For the case of the Terfenol-D actuator, where the coil generates an inductive reactance, a capacitor can be added in series to generate a capacitive reactance. Since inductive reactance and capacitive reactance are 180 degrees out of phase with each other, the reactances are subtracted to obtain a net reactance. For a given actuation frequency, the reactance of the added capacitor can be designed to be close to the reactance of the field generator, leaving a minimum net reactance. For the same input current, the actuator will then require much less voltage because the impedance of the circuit will be much smaller. For the piezostack actuator, an inductor can be added in parallel to produce a similar effect. This method of LC circuit tuning can be an effective way to reduce required power at a given actuation frequency. By tuning the circuit to the resonant frequency of the actuator, the condition for maximum output power can be obtained at a condition where minimum input power is required. This method could dramatically improve the efficiency of the actuator.

The problem with this method is tuning the LC circuit to the correct frequency. The reactances of the coil and capacitor both depend on input frequency. However, the inductance of the coil depends on the permeability of its core. In this case the Terfenol-D rod is the core, and its permeability varies depending on the applied magnetic field as well as the external stress. This variation in coil inductance with applied field makes it difficult to locate the resonant frequency of the LC circuit. Similarly, the capacitance of the piezostacks varies with applied field. The change in capacitance of the piezostack also changes its reactance. Another factor that could limit the power reductions from a tuned LC circuit is the DC resistance in the actuator which acts as damping in the circuit. For example, the DC resistance that is present in any inductor will limit the power reductions. Because of these difficulties, no substantial gains were achieved by applying this method to either actuator. Future generation pumps that are designed for a specific operating frequency could utilize this method to minimize the total input power required and maximize actuator efficiency.

Chapter 10: Bi-Directional Operation

10.1 Setup

To achieve bidirectional output capability in this actuator, it was necessary to design and build an active valve system to control the flow path of the fluid from the pumping chamber to the output cylinder. Two commercially available piloting solenoid valves from the Lee Company were chosen as the active valves in the system because of their compact size and negligible leakage [63]. A diagram of a solenoid valve is shown in Figure 10.1. The valves are controlled by applying a voltage across a solenoid coil. This creates a magnetic field that acts on a plunger. In the off position, the plunger is extended to cut off flow from the pressure port and allow flow between the control and return ports. In the on position, the plunger is retracted to allow flow from the pressure port to the control port.

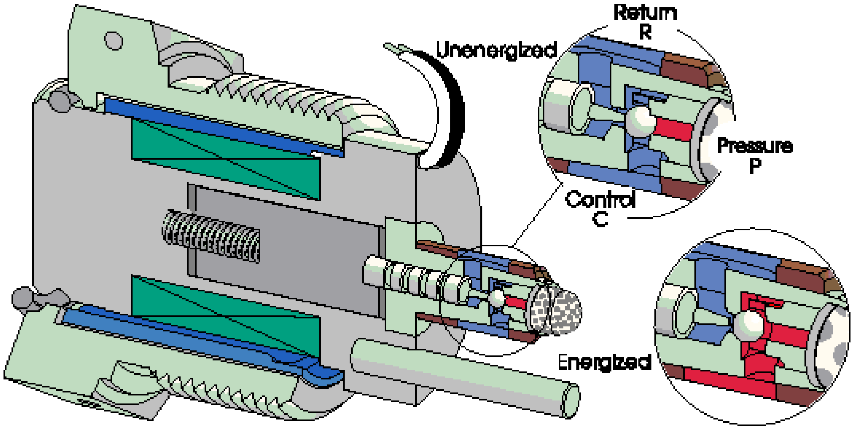

Figure 10.1 - Diagram of Solenoid Valve [63]

The valves use a current of 0.28 amps at 28 Vdc (7.8 Watts). Their maximum response time is 0.015 seconds to pull in at the rated pressure of 3000 psi, and 0.035 seconds to drop out at the rated pressure. For a complete cycle to open and close the valve, a time of 0.05 seconds is needed, making the valves capable of operating at frequencies up to 20 Hz. This was found to be acceptable as an initial investigation into bidirectional actuation. In addition, the low leakage in the valves was important to minimize performance losses in the system. The valves have zero leakage externally, and were found to have a maximum internal leakage of 2 cc/minute at the rated pressure of 3000 psi. The valves were used in a purely on-off fashion, controlled by a square wave.

In addition to the valves, a system of tubing was required to direct the flow in the proper direction from the pump to the output cylinder. For this, a new manifold was designed and constructed to house the solenoid valves. A drawing of the manifold is shown in Figure 10.2. The manifold directs fluid from the pump to the pressure ports of the two solenoid valves and creates a return path for the fluid from the output cylinder to the pump. By controlling the orientation of the solenoid valves, the flow path of the fluid can be changed to create bidirectional actuation. A schematic of the complete valve system coupled to the pump and output cylinder can be seen in Figure 10.3.

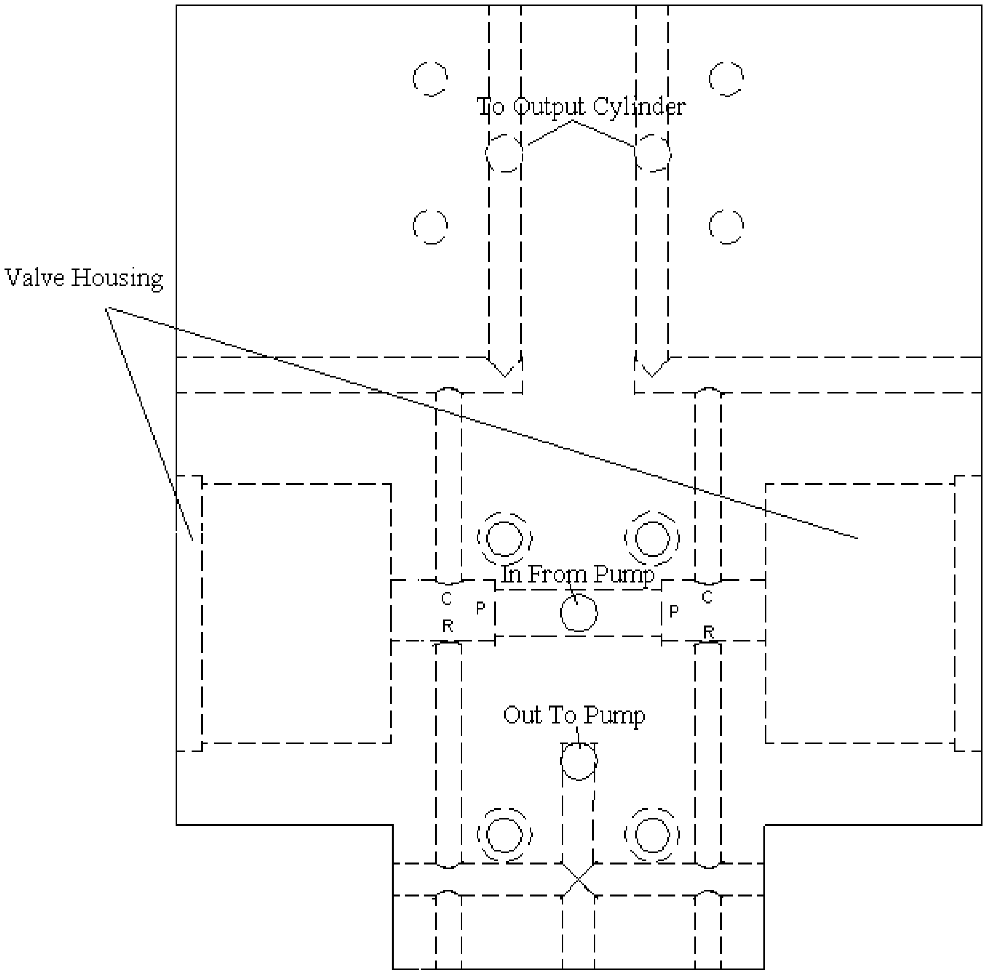

Figure 10.2 - Schematic of New Manifold

A control system for the bidirectional system was designed and constructed to enable the valve timing to be adjusted. A basic circuit was combined with the solenoid drivers to actuate the valves. A schematic of the electronics used in the control system is shown in Figure 10.4. The control and timing unit enables the setting of the duty cycle and timing of the waveforms sent to either directional solenoid valve. The valve driver unit accepts the signals from the control and timing unit and actuates the solenoid valves appropriately, taking power from a 24V DC power supply. A schematic circuit diagram of the valve driver is shown in Figure 10.5. All of the bi-directional testing was conducted with no overlap in the valve operation.

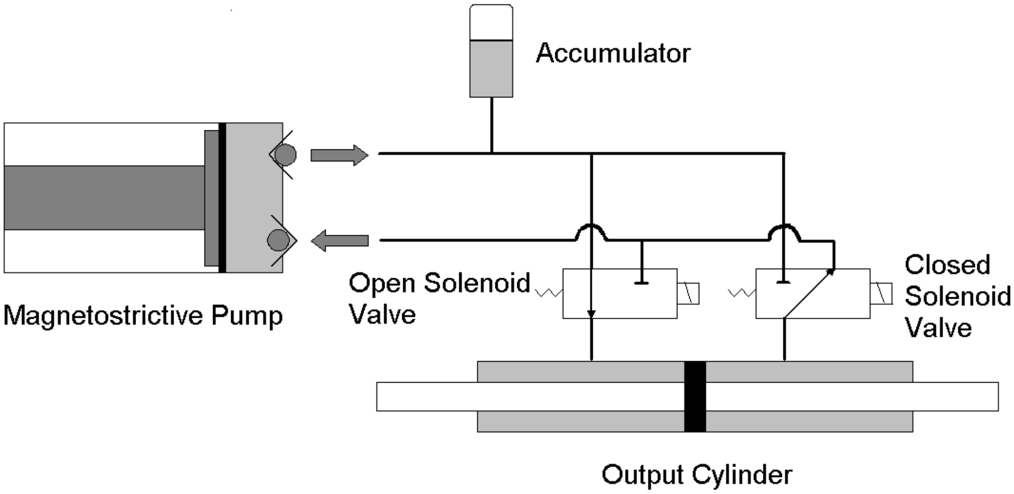

Figure 10.3 - Diagram of Bi-Directional Actuator

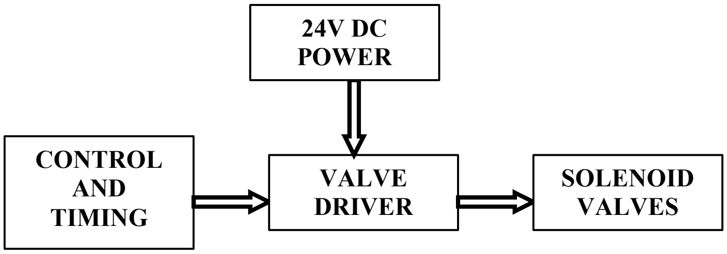

Figure 10.4 - Schematic of Valve Control System

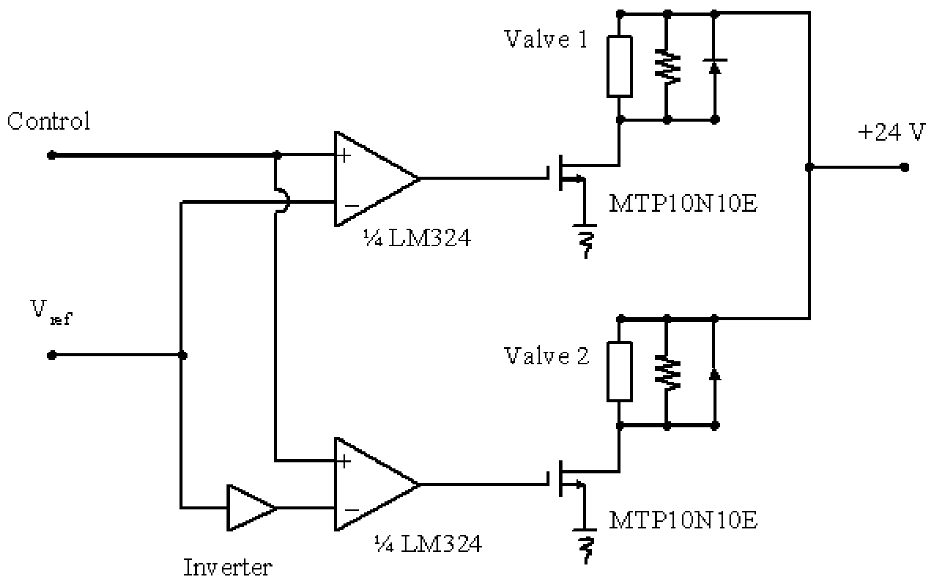

Figure 10.5 - Circuit Diagram for Valve Controller

10.2 Testing and Results

To investigate the bi-directional behavior of the actuator, the solenoid valve system was coupled to the Terfenol-D actuator as shown in Figure 10.6. The actuating material was preloaded to 4 ksi, and the fluid in the actuator was pressurized to 200 psi. A potentiometer was attached to the output shaft to measure the stroke and frequency of actuation. No output load was used during the bi-directional tests.

During the first test, the Terfenol-D actuator was driven at a constant frequency of 500 Hz, and a coil current of 3 amps. The output stroke per cycle was then measured as a function of output frequency from 0.5 Hz to 25 Hz. The results are shown in Figure 10.7. Because the flow rate from the pumping head is constant, there is a tradeoff in the output cylinder between output stroke and frequency. Assuming no leakage in the valves, the volume of fluid moved by the output cylinder for a given

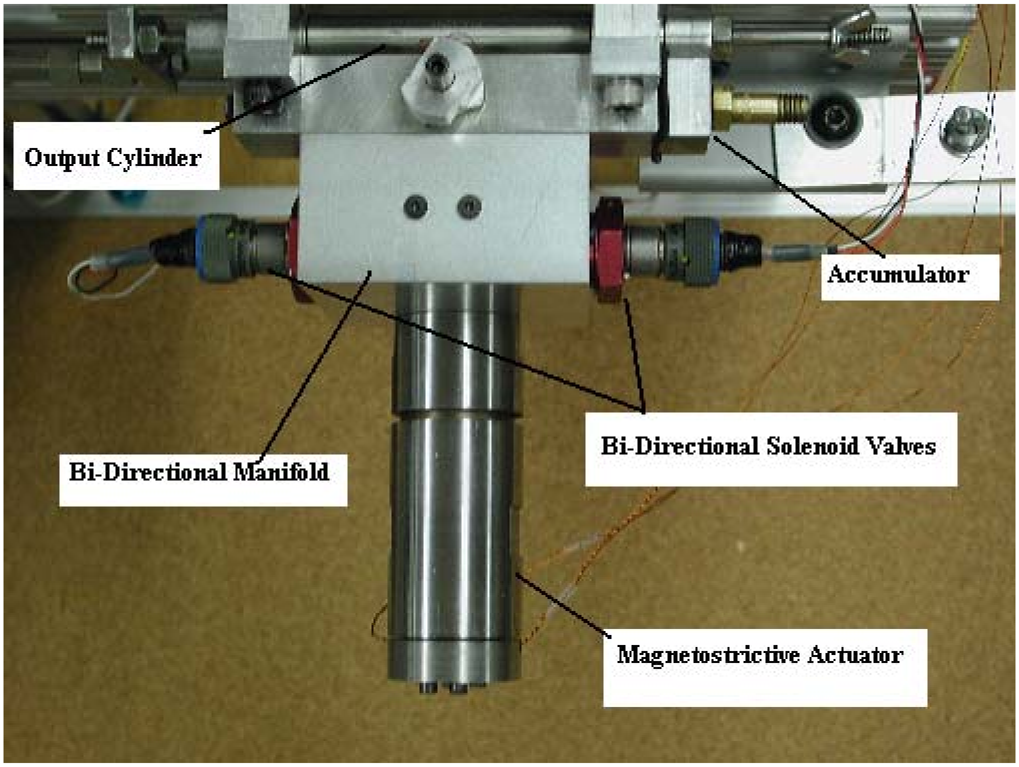

Figure 10.6 - Bi-Directional Actuator

time remains constant, so the product of the output stroke and frequency should also be constant. The plot of stroke vs. frequency should then form a rectangular hyperbola. Data obtained from the testing of the bi-directional Terfenol-D actuator agrees well with a hyperbola fit, as seen in Figure 10.7. It can then be concluded that the leakage in the valve system was negligible even with zero overlap in the valve timing. The equation of the hyperbola fit is,

$$\omega x = v \qquad \text{Eq. 10.1}$$

where ω is the output frequency (cycles/sec), x is the output stroke of one cycle (in/cycle), and v is the average velocity of the output shaft (in/s).

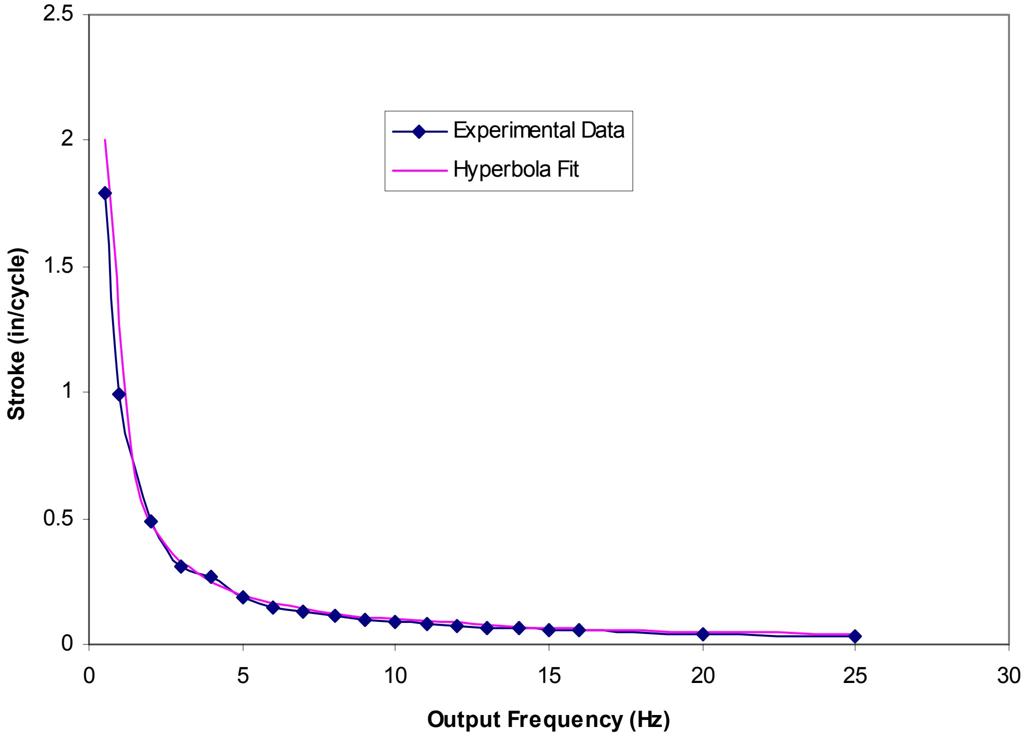

Figure 10.7 - Output Stroke of Bi-Directional Actuator

The no load velocity of the actuator at these conditions was found to be about 3 in/sec during uni-directional tests. The average velocity found during bi-directional testing was 1 in/sec. The degraded performance during bi-directional tests can be attributed to the additional viscous and inertial losses caused by the added tubing and fluid in the active valve system.

In addition to degrading the overall performance of the actuator, the additional fluid and tubing in the actuator from the valve system may also affect the frequency response of the system. A second bi-directional test was performed to investigate this possibility. For this test, the output frequency of the actuator was held constant at 1

Hz, while the output stroke was measured for varying actuation frequencies (0 to 600 Hz) of the Terfenol-D pump. The results of this test are shown in Figure 10.8. The results show that near 400 Hz, the output stroke saturates with increased driving frequencies. This is an unexpected result because during uni-directional testing, output velocities at this frequency were still increasing. The added tubing in the actuator from the new manifold is likely the cause of this trend. With additional fluid in the actuator, the overall stiffness of the hydraulic circuit will decrease, resulting in a lower natural frequency. Studies on the affect of tubing length on this actuator's frequency response can be found in [45]. A more extensive investigation into the

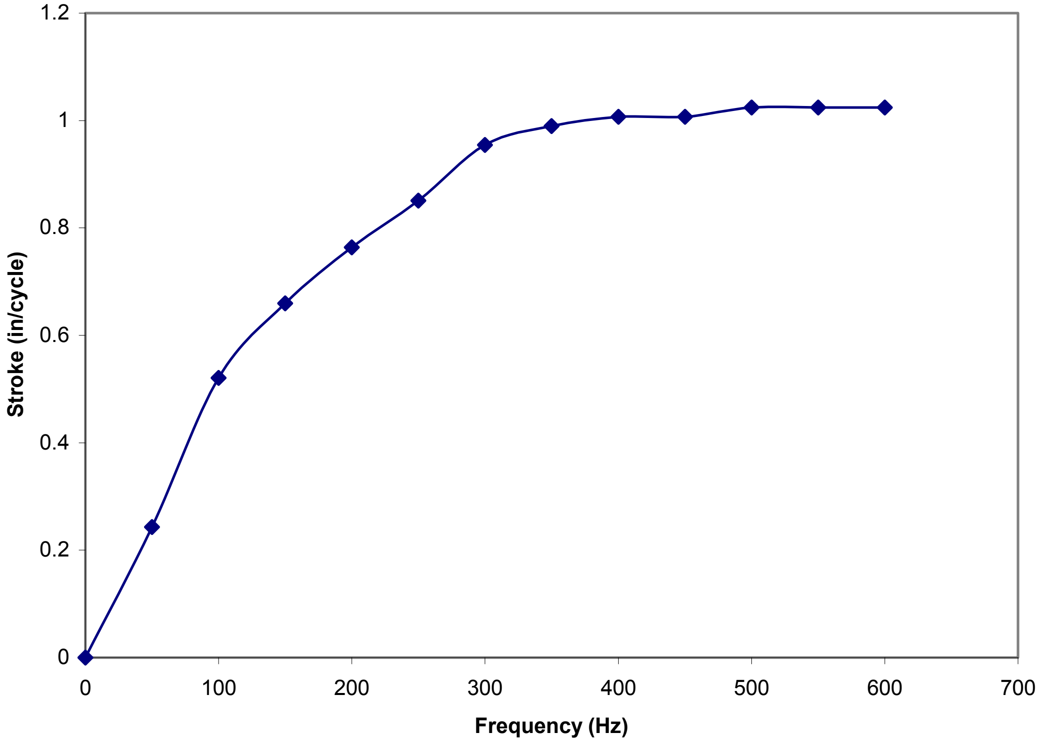

Figure 10.8 - Variation of Output Stroke With Actuation Frequency

frequency response of the hydraulic circuit in the bi-directional actuator will be needed to accurately identify this characteristic.

Chapter 11: Conclusions and Future Work

11.1 Conclusions

In order to compare the performance of a magnetostrictive pump and a piezo pump, a magnetostrictive and piezostack actuator were designed and constructed with equivalent active lengths. Their performance characteristics were then measured experimentally and normalized by the required input power of the actuator. By normalizing the performance characteristics of the actuators, the two pumps could be accurately compared.

The new piezostack actuator was simply a length extension of the previously tested piezostack actuator. After assembling the piezostack, the maximum induced strain was measured to be about $700\mu\varepsilon$. Performance characteristics such as unloaded output velocity and loaded velocity were then determined to obtain the maximum ouput power of the actuator. The maximum unloaded velocity of the piezo pump occurred at an actuation frequency of 700 Hz and was about 9 in/sec. Measurements of the loaded velocity of the piezo pump showed a maximum output power of 3.75 Watts at the same frequency. The force required to block the piezo pump from producing any output was about 14 lbs. The maximum power output occurred at a load of about 5 lbs. Heating was kept to a minimum by not actuating the pump for prolonged periods of time. Previous testing has already shown self-heating to be a problem in piezostack actuators.

A magnetostrictive actuator was designed and built for comparison with the piezostack actuator. A 1st generation coil was wound and tested as a first attempt at a magnetostrictive hydraulic-hybrid actuator. The maximum induced strain of a Terfenol-D rod achieved in this actuator was about 900 $\mu\varepsilon$. The actuator showed good performance with a Terfenol-D core, but was limited to low actuation frequencies due to high power requirements resulting from this high inductance coil. In addition, a large amount of heating in the coil was observed. To better understand these problems, a coil analysis was performed and it was determined that a coil with larger wire diameter should be wound to decrease the coil inductance. Thus the 2nd generation coil had a much lower inductance and required less voltage at the same mmf than the initial coil. This allowed the new coil to drive the Terfenol-D rod to the same levels of induced strain as the first coil and at twice the actuation frequency. In addition, slots cut in the pump body helped to reduce eddy currents and their effect on dissipating power. Without eddy currents creating a magnetic field in opposition to the coil, the actuator was able to generate the same mmf with less applied current. This resulted in a much more efficient coil, and self-heating was not observed in the new coil.

After failed attempts at driving the pump with Galfenol, it was determined that actuation of this pump would not be possible due to the low strain of the material. The maximum strain achieved in the Galfenol rod was only about 300 $\mu\varepsilon$, while it was shown that a minimum of about 350 $\mu\varepsilon$ was required to drive the pump output cylinder. To prove this, Terfenol-D was used as the active material and driven to the level of induced strain achieved in the Galfenol rod. The test produced no output velocity, and it was concluded that in order to build an efficient Galfenol driven pump, a larger pumping chamber would be required to generate more fluid flow using more piston displacement. It was also determined, through the coil analysis, that a coil with a Galfenol core would be much more inductive than a coil with a Terfenol-D core, resulting in a larger required voltage and input power. Galfenol is an attractive option for this type of actuator because of its robustness, machinability, and low cost. Terfenol-D is very brittle, and was shown to have problems with cracking due to the applied preload. It is also expensive and not machinable.

With improvements made to the 1st generation coil, the new Terfenol-D actuator was tested for the same performance characteristics as the piezo pump. The Terfenol-D pump was found to have a maximum unloaded velocity of about 10 in/sec at 550 Hz. The maximum output power of the actuator was 5 Watts occurring at an output load of 5 lbs., and an actuation frequency of 550 Hz. The blocked force of the Terfenol-D actuator was only about 10 lbs., due to its lower stiffness. Because the Terfenol-D pump achieved this level of performance with a higher level of induced strain than the piezo pump, an accurate comparison between the two could not be made without considering the input power. When compared based on input power, the piezo pump was found more efficient in unloaded and loaded condition. The maximum efficiency of the piezo pump was about 1.8%, while the Terfenol-D pump efficiency was only 0.9%. These efficiencies do not represent true power efficiencies, as the performance values are normalized using apparent power, and not dissipated power. The dissipated power efficiencies at the resonant frequency of the actuator are about twice as high as the apparent power efficiencies.

Overall, the piezo pump appears to be the more efficient actuator. It performed better in unloaded and loaded actuation when compared based on input power. In addition, the piezo actuator is much lighter than the Terfenol-D actuator, which requires a heavy coil to provide the required magnetic field. The piezo actuator is only about 35% of the mass of the Terfenol-D actuator. A major drawback of the piezo actuator is its self-heating problem. Presently, a form of active or passive cooling is required for prolonged actuation.

In addition to the comparison of driving materials in the hydraulic-hybrid actuator, a study was carried out to determine characteristics of bi-directional actuation. For this task, a valve system was designed and built using commercially available piloting solenoid valves (Lee Company). Two valves were utilized, along with a new manifold, to direct the fluid flow direction in order to control the direction of movement of the output piston. The system was tested for a range of input and output frequencies and showed overall good performance. It was noted that the velocity of the output cylinder was degraded substantially due to the increased viscous and inertial effects of the added fluid in the new manifold. As an initial attempt in bi-directional actuation, the valve system was successfully implemented and showed promising results.

11.2 Future Work

In order to investigate the possible benefits of a Galfenol driven hybrid actuator, a new actuator design must be generated to overcome the small stroke of Galfenol. In the current actuator, the maximum strain of Galfenol (~300 ppm) was shown to be insufficient for producing any fluid flow. An actuator using a pumping chamber with larger area would produce more fluid flow for a given piston displacement, and could improve the performance of a Galfenol driven hybrid actuator. The performance of a Galfenol driven hybrid actuator could then be compared to Terfenol-D and piezostack driven actuators to determine the most suitable for the envisaged application.

In addition, improvements to actuator modeling, particularly at high operating frequencies (~1000 Hz), must be made to provide an accurate design tool for future actuators. This will allow the actuator to be designed specifically for operation at the predicted resonant frequency, maximizing output power and efficiency.

Finally, testing of this actuator under centrifugal loading must be carried out to determine its feasibility for an active rotor application. The introduction of high centrifugal loads, such as the ones present on a helicopter rotor, may have degrading effects on the overall performance of the actuator. These effects must be determined through systematic experiments.

References

[1] Inderjit Chopra. "Status of application of smart structures technology to rotorcraft systems." *Journal of the American Helicopter Society*, 45(4): 228-252, October 2000.

[2] R.W. Prouty. *Helicopter performance, stability, and control.* Rober E. Kriege Publishing Company, Inc., Malabar, FL, 1990.

[3] P. R. Payne. "Higher harmonic rotor control". *Aircraft Engineering*, 30(354): 222-226, August 1958.

[4] K. Nguyen and I. Chopra. "Application of higher harmonic control to rotors operating at high speed and thrust." *Journal of the American Helicopter Society*, 35(3): 78-89, July 1990.

[5] K. Nguyen and I. Chopra. "Application of higher harmonic contro (HHC) to hingeless rotors." *Vertica*, 14(4): 545-556, October 1990.

[6] K. Nguyen and I. Chopra. "Effects of higher harmonic control on rotor performance and control loads." *Journal of Aircraft*, 29(3), May/June 1992.

[7] C.E. Hammond. "Wind tunnel results showing vibratory loads reduction using higher harmonic blade pitch." *Journal of the American Helicopter Society*, 28(1): 10-15, January 1983.

[8] E. R. Wood, R. W. Powers, C. H. Cline, and C.E. Hammond. "On developing and flight testing a higher harmonic flight control system." *Journal of the American Helicopter Society*, 30(1): 3-20, January 1985.

[9] W. Miao, S. B. R. Kottapali, and H. M. Frye. "Flight demonstration of higher harmonic control (HHC) on the S-76." *42nd American Helicopter Society Forum, Washington DC*, June 1986

[10] M. Polychroniadis and M. Achache. "Higher harmonic control: flight tests of an experimental system on an sa 349 research gazelle." 42nd American Helicopter Society Forum, Washington DC, June 1986.

[11] J. Shaw, N. Albion, E. J. Hanker, and R. S. Teal. "Higher harmonic control: wind tunnel demonstration of fully effective vibratory hub forces suppression." *Journal of the American Helicopter Society*, 34(1): 14-25, January 1989.

[12] J. Bao and I. Chopra, *Development of Mach Scale Rotors with Composite Tailored Couplings for Vibration Reduction*. PhD defense, University of Maryland, College Park, MD, 2004.

[13] Inderjit Chopra and J. L. McCloud, III. "A numerical simulation study of open-loop, closed-loop and adaptive multicyclic control systems." *Journal of the Amercan Helicopter Society*, 28(1): 311-325, January 1983.

[14] Peter C. Chen and Inderjit Chopra. "Wind tunnel test of a smart rotor model with individual blade twist control." *Journal of Intelligent Material Systems and Structures*, 8(5): 414-425, May 1997.

[15] Judah Milgram and Inderjit Chopra. "A parametric design study for actively controlled flaps." *Journal of the American Helicopter Society*, 43(2): 110-119, April 1998.

[16] Andreas Paul Friedrich Bernhard. *Smart Helicopter Rotor with Active Blade Tips*. PhD thesis, University of Maryland, College Park, MD 20742 USA, February 2000.

[17] A.P.F. Bernhard, J. O'Neill, F. Kohlhepp, W. Welsh, and P. Lorber. "Active Rotor Control (ARC) of a mach-scale trailing edge flap rotor." *Presented at the American Helicopter Society 57th Annual Forum, Washington DC*, May 9-11 2001.

[18] J. Falls and I. Chopra, "

[19] B. Roget and I. Chopra, "

[20] Jeanette J. Epps. *In-Flight Tracking of Helicopter Rotor Blades with Tabs Using Shape Memory Alloys*. PhD thesis, University of Maryland, College Park, MD 20742 USA, 2000

[21] Harsha Prahlad and Inderjit Chopra. "Design of a variable twist tilt-rotor blade using shape memory alloy (SMA) actuators." *Proceedings of SPIEs Annual Symposium on Smart Structures and Materials, Newport Beach, CA*, 4327: 46-59, 2001.

[22] Jayanth N. Kudva, Brian P. Sanders, Jennifer L. Pinkerton-Florance, and Ephrahim Garcia. "Overview of the DARPA/AFRL/NASA Smart Wing Phase II program." *Proceedings of the 8th SPIE Conference on Smart Structures and Materials: Industrial and Commercial Applications of Smart Structures Technologies, Newport Beach, CA*, 4332: 383-389, March 2001.

[23] J. S. Paine and Z. Chaudhry. "The impact of amplification on efficiency and energy density of induced strain actuators." *Proceedings of the SAME Aerospace Division*, AD52: 511-516, 1996.

[24] Timothy P. Galante, Jeremy E. Frank, Julien Bernard, Weicheng Chen, George A. Lesieutre, and Gary H. Koopmann. "Design, modeling and performance of a high force piezoelectric inchworm motor." *Proceedings of the 5th SPIE Smart Structures and Materials Symposium: Smart Structures and Integrated Systems, San Diego, CA*, 3329: 756-767, March 1998.

[25] Khanh Duong and Ephrahim Garcia. "Design and performance of a rotary motor driven by piezoelectric stack actuators." *Japanese Journal of Applied Physics*, Part1, 35(12A): 6334-6341, December 1996.

[26] T. Sashida and T. Kenjo. *An Introduction to Ultrasonic Motors*. Clarendon Press, Oxford, 1993.

[27] L. D. Mauck and C. S. Lynch, "Piezoelectric hydraulic pump." *Proceedings of the 6th SPIE Conference on Smart Structures and Integrated Systems, Newport Beach, CA*, 3668: 844-852, March 1999.

[28] L. D. Mauck and C. S. Lynch, "Piezoelectric hydraulic pump optimization." *Proceedings of the 11th International Conference on Adaptive Structures Technology*, pg. 100-107, 1999.

[29] L. D. Mauck, J. Menchaca, and C. Lynch, "Piezoelectric hydraulic pump development." *Proceedings of the 7th SPIE Conference on Smart Structures and Integrated Systems, Newport Beach, CA*, March 2000.

[30] L. D. Mauck, and C. Lynch, "Piezoelectric hydraulic pump development." *Journal of Intelligent Material Systems and Structures,* 11, pg. 758-764, October 2000.

[31] L. D. Mauck, W. S. Oates, and C. Lynch, "Piezoelectric hydraulic pump performance." *Proceedings of the 8th SPIE Conference on Industrial and Commercial Applications of Smart Structures Technologies, Newport Beach, CA*, March 2001.

[32] K. Nasser, D. Leo, and H. H. Cudney, "Compact piezohydraulic actuation system." *Proceedings of the 7th SPIE Conference on Industrial and Commercial Applications of Smart Structures, Newport Beach, CA*, March 2000.

[33] K. Nasser, *Development and Analysis of the Lumped Parameter Model of a Piezohydraulic Actuator.* Master's thesis, Virginia Polytechnic Institute and State University, Blacksburg, VA 24061, USA, November 2000.

[34] K. Nasser and D. J. Leo, "Efficiency of frequency-rectified piezohydraulic and piezopneumatic actuation." *Journal of Intelligent Material Systems and Structures*, 11: 798-810, October 2000.

[35] K. Nasser, N. Vujic, D. J. Leo, and H. H. Cudney, "Modeling and testing of a piezohydraulic actuation system." *Proceedings of the 8th SPIE Conference on Smart Structures and Integrated Systems, Newport Beach, CA*, March 2001.

[36] K. Konishi, I. Yoshimura, K. Hashimoto, and N. Yamamoto, "Hydraulic actuators driven by piezoelectric elements (1st report, trial piezoelectric pump and its maximum power)." *Journal of Japanese Society of Mechanical Engineering* ©59(564), pg. 213-220, 1993.

[37] K. Konishi, T. Yoshiura, K. Hashimoto, T. Hamada, and T. Tamura, "Hydraulic actuators driven by piezoelectric elements (2nd report, enlargement of piezoelectric pumps output power using hydraulic resonance)." *Journal of Japanese Society of Mechanical Engineering* ©60(571), pg. 228-235, 1994.

[38] K. Konishi, K. Hashimoto, T. Miyamoto, and T. Tamura, "Hydraulic actuators driven by piezoelectric elements (3rd report, position control using piezoelectric pump and hydraulic cylinder)." *Journal of Japanese Society of Mechanical Engineering* ©61(591), pg. 134-141, 1995.

[39] K. Konishi, H. Ukida, and T. Kotani. "Hydraulic actuators driven by piezoelectric elements (4th report, construction of mathematical models for simulation)." *Journal of Japanese Society of Mechanical Engineering* ©63(605), pg. 158-165, 1997.

[40] M. J. Gerver, J. H. Goldie, J. R. Swenbeck, et. al. "Magnetostrictive water pump." *Proceedings of the 6th SPIE Conference on Smart Structures and Integrated Systems, Newport Beach, CA*, 3329: 694-705, March 1998.

[41] F. Claeyssen, N. Lhermet, "Actuators based on giant magnetostrictive materials." *8th International Conference on New Actuators, Bremen, Germany*, June 2002.

[42] E. H. Anderson and J. E. Lindler, "Smart material actuator with long stroke and high power output." *43rd AIAA/ASME/ASCE/AHS/ASC Structures, Structural Dynamics, and Materials Conference, Denver, Colorado*, April 2002.

[43] J. Sirohi and I. Chopra, "Design and testing of a high pumping frequency piezoelectric-hydraulic hybrid actuator." *Proceedings of the 9th SPIE Conference on Smart Structures and Integrated Systems, San Diego, CA*, March 2002.

[44] J. Sirohi, *Piezoelectric Hydraulic Hybrid Actuator for a Potential Smart Rotor Application*. PhD thesis, University of Maryland, College Park, MD, 20742, 2002.

[45] J. Sirohi and I. Chopra, "Design and development of a high pumping frequency piezoelectric-hydraulic hybrid actuator." *Journal of Intelligent Material Systems and Structures*, Vol. 14, No. 3, pg. 135-147, March 2003.

[46] J. Sirohi, C. Cadou, and I. Chopra, "Frequency domain modeling of a piezohydraulic actuator." *Proceedings of the 44th AIAA/ASME/ASCE/AHS/ASC Structures, Structural Dynamics & Materials Conference, Norfolk, VA*, April 2003.

[47] C. Cadou and B. Zhang, "Performance modeling of a piezo-hydraulic actuator." Journal of Intelligent Material Systems and Structures, Vol. 14, No. 3, pg. 149-160, March 2003.

[48] Etrema Products, Inc., http://www.etrema-usa.com, Ames, IA, 2003.

[49] F. Calkins, A. Flatau, *Design, Analysis, and Modeling of Giant Magnetostrictive Transducers.* PhD Dissertation, Iowa State University, 1997.

[50] R. Kellogg, A. Flatau, "Blocked force investigation of a Terfenol-D transducer," *SPIE's 6th Annual International Symposium on Smart Structures and Materials*, 3668-19, March 1999.

[51] R. Kellogg, A. Flatau, A. Clark, M. Wun-Fogle, T. Lograsso, "Temperature and stress dependences of the magnetic and magnetostrictive properties of $Fe_{0.81}Ga_{0.19}$." *Journal of Applied Physics,* 91, 7821 (2002).

[52] V. Giurgiutiu, R. Pomirleanu, C. Rogers, "Energy-based comparison of solid-state actuators." *University of South Carolina, Laboratory for Adaptive Materials and Smart Structures*, March 2000.

[53] J. Yoo, J. Sirohi, S. John, A. Chaudhuri, C. Cadou, N. Wereley, "Bidirectional control of a magnetorheological piezohydraulic actuator." *SPIE Smart Structures and Materials 2004: Smart Structures and Integrated Systems*, 5390 pg. 116-126, 2004.

[54] Bimba Manufacturing Company, http://www.bimba.com, Monee, IL, 1999.

[55] AE Techron, http://www.aetechron.com, Elkhart, IN, 2004.

[56] QSC Audio, http://www.qscaudio.com, Costa Mesa, CA, 2004

[57] Stanford Research Systems, http://www.thinksrs.com, Sunnyvale, CA, 2003.

[58] National Instruments, http://www.ni.com, Austin, TX, 2004.

[59] The MathWorks, http://www.mathworks.com, Natick, MA, 2004.

[60] Vishay Measurements Group, http://www.vishay.com, Malvern, PA, 2004.

[61] I. Chopra and J. Sirohi, "Smart structures class notes: Piezoelectric actuators and sensors, Electrostrictives and magnetostrictives." University of Maryland, College Park, MD, 2004.

[62] Physik Instrumente (PI). Products for Micropositioning, US-edition, 1997.

[63] The Lee Company, Technical Hydraulic Handbook. Westbrook, CT, 2003.